Pulse-Shaping-Based Nonlinear Microscopy: Development and Applications

By

Daniel Christopher Flynn

A dissertation submitted in partial fulfillment
of the requirements for the degree of
Doctor of Philosophy
(Macromolecular Science and Engineering)
in the University of Michigan
2014

Doctoral Committee:

Associate Professor Jennifer P. Ogilvie, Co-Chair
Professor Richard M. Laine, Co-Chair
Professor Raoul Kopelman
Professor Richard Robertson
Professor Eitan Geva

"Calvin: …that's the whole problem with science. You've got a bunch of empiricists trying to describe things of unimaginable wonder"
-Bill Watterson

DEDICATION

For my parents

ACKNOWLEDGEMENTS

I have been very fortunate to have the strong support of family, friends, coworkers and even strangers throughout my graduate career. The University of Michigan has provided a strong foundation for this support structure and has enabled many fulfilling and enjoyable pursuits. The number of people who have made an impact on my life here is simply astounding. For those not mentioned, please know your support has not been forgotten.

I want to start by thanking the Department of Defense (DoD) for supporting me through the National Defense Science & Engineering Graduate Fellowship (NDSEG) Program. This funding has given me tremendous academic freedom and allowed me to pursue research that would have otherwise been inaccessible.

The Macromolecular Science and Engineering program has served as a home away from home. I want to specifically thank Nonna Hamilton and Richard Laine for their support. My first experience with a Michigan winter may not have been as pleasant if it hadn't been for Nonna. She bought all the first year students gloves and scarves out of fear we would freeze. Her kindness, generosity and support have been a constant throughout my graduate career. Professor Laine has and continues to push me forward. His high expectations and unwillingness for compromise has stretched me as a researcher, for which I am very grateful. I also want to thank Professor Robertson whose critiques and guidance have provided depth to my academic progression.

I want thank my graduate supervisor and mentor, Jennifer Ogilvie. Her drive, focus, scientific intuition and integrity are inspiring. She is one of a few individuals who

can take a theoretical concept and apply it in ways that make a meaningful contribution to a field. The opportunity to learn from her has not only been intellectually fulfilling but enjoyable as well. She has really stretched me as a researcher and I am proud to have had the opportunity to work for her.

I am very fortunate to have a supportive dissertation committee. Having Raoul Kopelman, Eitan Geva, Richard Laine, Richard Robertson, and Jennifer Ogilvie in one room has been both intimidating and exciting. They are quick to spot my weaknesses and while their critiques carry weight, their questions have guided me as a researcher.

I have been very fortunate to be a member of the Ogilvie lab. In no particular order, I want to thank Dawen Cai, Seckin Senlik, Amar Bhagwat, Meredith Brenner, Anton Loukianov, Jie Pan, Veronica Policht, Andrew Niedringhaus and Marcos Nunez. Special thanks goes to Daniel Wilcox and Franklin Fuller for all their help since I joined the lab. I have made many friendships and am excited to see where these talented individuals go next. I want to specifically thank Amar Bhagwat, who I have had the pleasure of working closely with over the past two and a half years. He has been a tremendous resource and I continue to learn from him. The work presented in this dissertation is a result of our teamwork.

I want to thank the undergraduates with whom I have had the privilege of mentoring. I specifically want to thank Meghan Orr and Briana Mork for their enthusiasm and dedication. Like my mentors, I held high expectations for these two students and pushed them to realize their capabilities. To see their growth has been one of the most fulfilling aspects of my time at Michigan.

I want to thank my undergraduate adviser, Arlette Baljon. She supported my growth as a scientist starting as a second year undergraduate and continues, unequivocally, today. I can't count the number of letters of recommendation she has written, let alone attempt to recognize the time and effort she has invested in me. Besides serving as a mentor, she is a brilliant scientist and I am very thankful to have been exposed to this form of intellect so early in my career. She also introduced me to the "Mito Group", a group of researchers focused on the biophysics of mitochondria. The opportunity to be a part of this group was a wonderful experience as an undergraduate. I want to thank Jim Nulton, Peter Salamon, Terry Frey, and Avinoam Rabinovitch for all of their support. I owe a lot of thanks to Jim, who spent countless hours teaching me Matlab, giving me one-on-one lectures, and really pushing me forward.

I want to thank my family. My parents and brother have always been a significant source of support and inspiration in my life and I have leaned on them significantly over the course of my graduate career. I am looking forward to spending more time with them and going on more adventures together. My grandparents have always been supportive while holding high expectations. My grandmom and granddad would take my cousins, brother and I on many trips together, where we had the opportunity to explore and use our imaginations. Starting at an early age, my Opa would give me savings bonds for my birthday to be used only for college. While not exactly a thrilling present for a five year old, it was a gift that enabled my progression through college and the many opportunities that followed.

I am fortunate to have many friends who have supported me throughout the years. My friends in Ann Arbor, Irvine, and San Diego have all played unique and important

roles, most of which I cannot possibly properly thank here. I want to especially thank Özgün Süzer who helped guide me when I was a first year graduate student and who continues to do so today. Sitting between my future wife and I when we first began dating must have been a special kind of hell, and yet he has remained a friend and mentor. I also want to thank my family friends, the Siglers, Likens, Chicos, McCords, and Gilmores, for all of their support over the years.

Finally, none of this would have been possible without the love and support of my future wife, Jessica Donehue. Beyond playing the role of my fiancé, she is a tremendous scientist and I have benefitted greatly from our conversations. I am excited for the next chapter of our lives together.

TABLE OF CONTENTS

LIST OF FIGURES

LIST OF TABLES

LIST OF ABBREVIATIONS

BBO	Beta Barium Borate
CARS	Coherent Anti-Stokes Raman Scattering
DMEM	Dulbecco's Modified Eagle's Medium
ESA	Excited State Absorption
FLIM	Fluorescence Lifetime Imaging Microscopy
FRET	Fluorescence Resonance Energy Transfer
GD	Group Delay
GDD	Group Delay Dispersion
GFP	Green Fluorescent Protein
GSB	Ground State Bleach
MIIPS	Multiphoton Intrapulse Interference Phase Scan
NA	Numerical Aperture
PBS	Phosphate-Buffered Saline
PMT	Photomultiplier Tube
SE	Stimulated Emission
SH	Second Harmonic
SHG	Second Harmonic Generation
SLM	Spatial Light Modulator
Ti:Sapph	Titanium:Sapphire
TL	Transform-Limited
TOD	Third Order Dispersion
TPA	Two Photon absorption
TPEF	Two photon excited fluorescence

ABSTRACT

Pulse-shaping-based nonlinear microscopy: development and applications

By

Daniel Christopher Flynn

Chair: Jennifer P. Ogilvie and Richard M. Laine

The combination of optical microscopy and ultrafast spectroscopy make the spatial characterization of chemical kinetics on the femtosecond time scale possible. Commercially available octave-spanning Ti:Sapphire oscillators with sub-8 fs pulse durations can drive a multitude of nonlinear transitions across a significant portion of the visible spectrum with minimal average power. Unfortunately, dispersion from microscope objectives broadens pulse durations, decreases temporal resolution and lowers the peak intensities required for driving nonlinear transitions. In this dissertation, pulse shaping is used to compress laser pulses after the microscope objective. By using a binary genetic algorithm, pulse-shapes are designed to enable selective two-photon excitation. The pulse-shapes are demonstrated in two-photon fluorescence of live COS-7 cells expressing GFP-variants mAmetrine and tdTomato. The pulse-shaping approach is applied to a new multiphoton fluorescence resonance energy transfer (FRET) stoichiometry method that quantifies donor and acceptor molecules in complex, as well as the ratio of total donor to acceptor molecules. Compared to conventional multi-photon imaging techniques that require laser tuning or multiple laser systems to selectively excite

individual fluorophores, the pulse-shaping approach offers rapid selective multifluorphore imaging at biologically relevant time scales. By splitting the laser beam into two beams and building a second pulse shaper, a pulse-shaping-based pump-probe microscope is developed. The technique offers multiple imaging modalities, such as excited state absorption (ESA), ground state bleach (GSB), and stimulated emission (SE), enhancing contrast of structures via their unique quantum pathways without the addition of contrast agents. Pulse-shaping based pump-probe microscopy is demonstrated for endogenous chemical-contrast imaging of red blood cells.

In the second section of this dissertation, ultrafast spectroscopic techniques are used to characterize structure-function relationships of two-photon absorbing GFP-type probes and optical limiting materials. Fluorescence lifetimes of GFP-type probes are shown to depend on functional group substitution position, therefore, enabling the synthesis of designer probes for the possible study of conformation changes and aggregation in biological systems. Similarly, it is determined that small differences in the structure and dimensionality of organometallic macrocycles result in a diverse set of optical properties, which serves as a basis for the molecular level design of nonlinear optical materials.

Chapter 1 Introduction

1.1 Motivation for Nonlinear Microscopy

The optical characterization of materials is far from a new field, so it may surprise an outsider to find the field's steady progress and increasing sophistication. While today's modern microscopes are often complex, they still have many simple elements seen in the first microscopes, comprising a light source, focusing element, sample stage, and a detector (figure 1.1). In fact, these same simple elements are found in the microscopes developed for this dissertation. The powerful distinction, however, between these early microscopes and those developed for this dissertation is the light source used and the interaction this light has with the sample. In this dissertation, we shape pulses of light to drive specific responses from materials based on their unique quantum pathways, and use these responses as imaging modalities enabling high contrast images of the microscopic world.

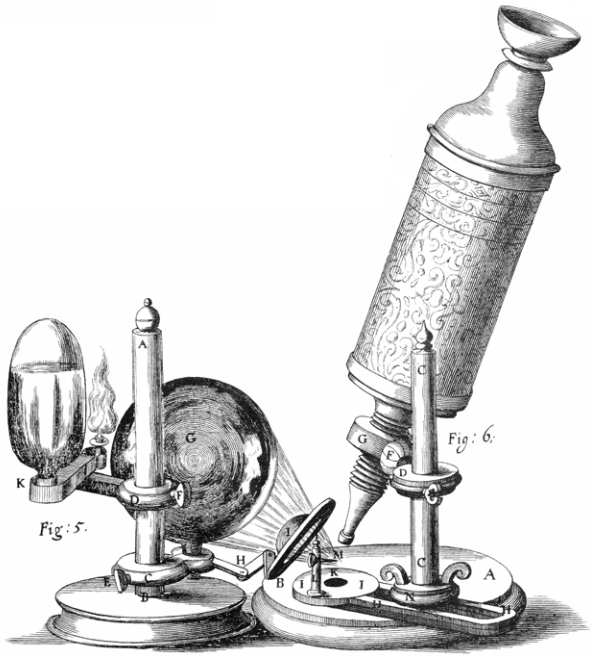

Figure 1.1 Robert Hooke's microscope from scheme 1. of his 1665 Micrographia.

The history of microscopy development is fascinating and there are many reviews on the topic.[1,2] While lenses have been around since ancient times, the first microscope wasn't developed until the sixteenth century. These first microscopes relied on the contrast between absorption and transmission of light to create an image. The images often suffered from minimal contrast due to the lack of absorption of thin samples. To overcome this issue, biologists resorted to staining specimens with dyes. Unfortunately, there was minimal control of the staining process resulting in limited enhancement and poor control over what was labeled. New imaging modalities were also developed. Instead of using absorption and transmission of light, phase, polarization, interference, and fluorescence began to be used as modes of contrast.[2] The ability to resolve smaller and finer details with optical microscopes was also improved. Finely tuned optics now allow for modern microscope objectives to have resolution with minimal aberrations and

to be limited by the diffraction limit. The Abbe equation relates this fundamental limit by defining resolution in terms of wavelength and the numerical aperture (NA) as

$$d = \frac{\lambda}{2NA} \tag{1.1}$$

where NA is defined as $n\sin(\alpha)$, with n being the refractive index of the medium and α the half angle of the objective light collection. The relationship illustrates that visible light microscopy has a resolution limit of approximately 200 nm. Modern techniques are under continuous development to beat the diffraction limit, and current fluorescence based "super-resolution" methods have enabled resolution on the tens of nanometer scale.[3,4]

The first confocal microscope was developed by Marvin Minsky in 1957.[5] Unlike wide-field microscopy, where a light source illuminates an area of the sample that is then imaged with a camera, confocal microscopes enhance lateral resolution and optical-sectioning capabilities by illuminating a single point at a time, using pinholes to reject out-of-focus light. By rastering the sample across the excitation spot, two-dimensional images can be created. With the addition of vertical axis of motion, two-dimensional images may be combined to create three-dimensional images. Over time, variations of confocal microscopy have been developed to increase resolution and contrast, as well as speed up image acquisition time.[6,7]

The invention of the laser has played a pivotal role in the evolution of microscopy. Initially, the laser allowed for the selective excitation of specific chromophores. It wasn't until 1978 that confocal laser scanning microscopy (CLSM) was developed. Using fluorescent markers, Christopher and Thomas Cremer were able to

show the first images acquired via raster scanning with a CLSM.[6] The coherent nature of light as well as the high peak power emitted from lasers has culminated in the new field of nonlinear microscopy, where nonlinear light-matter interactions are used as new modes of contrast. In 1990, two-photon laser scanning fluorescence microscopy was demonstrated for the first time.[7] Compared to one-photon absorption, this mechanism enables enhanced depth penetration, due to decreased scattering, as well as intrinsic three-dimensional sectioning and reduced photodamage. While tunable femtosecond lasers have been used to excite specific fluorophores, the time it takes to tune the laser cavity inhibits imaging of multiple fluorophores at biologically relevant time scales. One technique used to overcome this limitation is to excite multiple fluorophores with overlapping two-photon cross-sections and then spectrally filter the emission.[8] Unfortunately, this method has only worked with up to two fluorophores, as increasing the number of fluorophores results in significant emission crosstalk. Recently, a three-color method was demonstrated using a coherent control technique.[9]

Fluorescence microscopy was further revolutionized with the discovery and use of green fluorescent proteins (GFP).[10-12] Instead of staining cells with dyes or other contrast agents, cells can be genetically altered to express fluorescent proteins. These fluorescent proteins are significantly less toxic to cells than previous techniques, enabling prolonged cellular expression. The ability to tag specific proteins within a cellular system with a variety of spectrally different fluorophores has dramatically increased our ability to selectively observe particular proteins of interest and to follow their role in a wide range of cellular processes. Variations of the genetic expression of GFP structure can result in different emission wavelengths, depicted in figure 1.2.[13] Recently, resonant enhancement

of two-photon transitions in the UV, $S_0 \rightarrow S_n$, have been found to give access to higher lying excited states of GFP variants and hence, increased excitation spectral bandwidth.[14,15] Taking advantage of this extra bandwidth, a two-color imaging methodology has been used to excite both the low-lying and the high-lying electronic states of two separate fluorophores.[16] Furthermore, by integrating multiple broadband lasers into one microscope setup, larger portions of the multiphoton bandwidth are easily accessable.[17,18] Unfortunately, the expense and complicated timing procedures required for these methodologies limit their use to few modern laboratories.

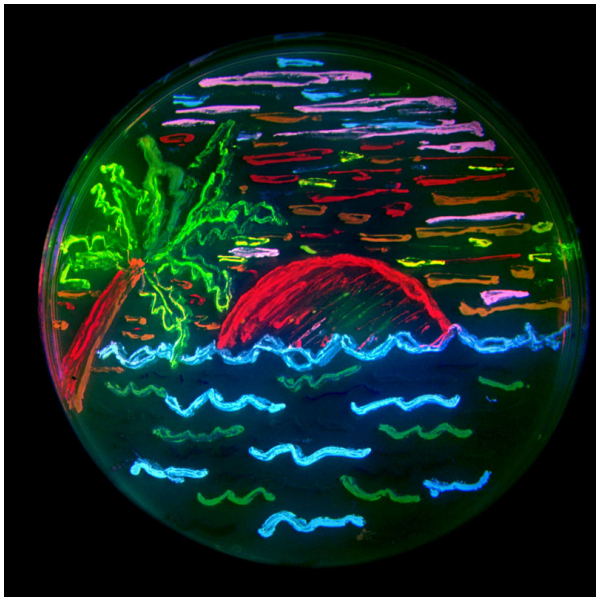

Figure 1.2 A San Diego beach scene drawn with an eight color palette of bacterial colonies expressing fluorescent proteins derived from GFP and the red-fluorescent coral protein dsRed. The colors include BFP, mTFP1, Emerald, Citrine, mOrange, mApple, mCherry and mGrape. Artwork by Nathan Shaner, photography by Paul Steinbach, created in the lab of Roger Tsien in 2006.

Increased sophistication in fluorescent probes has enabled new forms of imaging. Forster resonance energy transfer (FRET) is often referred to as a "spectroscopic ruler", because of its ability to measure molecular interactions on the 1-10 nm scale between

donor and acceptor molecules.[19] Multiple reviews on the various applications of FRET can be found in the literature.[20-22] While, researchers were already using this technique to determine interaction and distance relationships of macromolecules within cells in the 1970s, the continued advancement and application of FRET has led some researchers to claim the field to be currently experiencing a Renaissance.[23,24] Previous limitations to FRET measurements have been the lack of quantitative information. Recently, stoichiometric methods have been developed to determine the fraction of donor and acceptor in complex.[25-27] Since fluorescence lifetime decay, emission spectra and rotational diffusion have been shown to be independent of the excitation mode (1PA or TPA), there is substantial interest in the field to extend FRET stoichiometry to two-photon excitation.[28,29]

Imaging cells with contrast agents is expensive, time consuming, and can be perturbing to the system. Nonlinear spectroscopy offers routes towards using endogenous contrast agents to image cellular systems. Three and four-wave mixing processes have been the primary mechanisms used in imaging. These include, second harmonic generation (SHG)[30], third harmonic generation (THG)[31-33], two photon excited fluorescence (TPEF)[7], coherent anti-stokes Raman (CARS)[34,35], self phase modulation (SPM)[36], interferometric techniques[37], and pump-probe processes[38-40] of endogenous fluorophores. Fluorescence lifetime imaging microscopy (FLIM) has also be used to distinguish chemical constituents.[41]

Pulse shaping based nonlinear microscopy offers significant advantages to current multiphoton imaging techniques. Integrated with octave spanning lasers, pulse shaping can enhance image contrast by compensating for dispersion and enabling selective

multiphoton excitation of a wide range of molecular species using constructive and destructive multiphoton interference. Millisecond switching between pulse shapes enables multi-fluorophore imaging at biologically relevant time scales. Recently, live cell imaging using pulse-shaping has been demonstrated.[9,42,43] Combining pulse-shaping with linear unmixing techniques has also allowed the separation of overlapping fluorescence signals of three fluorescent proteins.[29]

1.2 Nonlinear Optical Properties of Molecules

Ultrafast spectroscopy refers to the spectroscopic technique of using a laser pulse(s) to study chemical dynamics on the femtosecond time scale.[44] The short time scale allows researchers to probe the unique electronic and vibrational dynamics of molecular structures. The high peak power of these pulses gives accesses to a multitude of nonlinear quantum pathways, and offers a glimpse into the underlying mechanisms associated with the structure of molecules. Combining ultrafast spectroscopy with microscopy enables imaging modalities based on these nonlinear quantum pathways and offers structure-function insight.

The time-varying polarization of a molecule due to the application of a time varying electric field results in the creation of new electromagnetic fields. This process is mathematically described by the wave equation

$$\nabla^2 E - \frac{n^2}{c^2}\frac{\partial^2 E}{\partial t^2} = \frac{4\pi}{c^2}\frac{\partial^2 P^{NL}}{\partial t^2} \tag{1.2}$$

The second order derivative of the nonlinear polarization, P^{NL}, describes the acceleration of charges due to the presence of an electric field. Induced polarization from an applied

electric field is dependent on the field strength. In the linear domain, this relationship is mathematically described by

$$P(t) = \chi^{(1)} E(t) \tag{1.3}$$

where $\chi^{(1)}$ is the linear susceptibility. When a powerful electric field is applied, equation 1.2 is no longer valid in describing the induced polarization, and equation 1.3 must be generalized for the nonlinear response. Expressing the polarization as a power series of the electric field strength we obtain a generalized equation for the induced polarization in the time domain

$$\begin{aligned} P(t) &= \chi^{(1)} E(t) + \chi^{(2)} E^2(t) + \chi^{(3)} E^3(t) + \ldots \\ &\equiv P^{(1)}(t) + P^{(2)}(t) + P^{(3)}(t) + \ldots \end{aligned} \tag{1.4}$$

In the frequency domain, this bulk description may be described by the relationship

$$\begin{aligned} P_I(\omega_1) = &\sum_J \chi^{(1)}_{IJ}(-\omega_1;\omega_2) E_J(\omega_2) + \sum_{JK} \chi^{(2)}_{IJK}(-\omega_1;\omega_2,\omega_3) E_J(\omega_2) E_K(\omega_3) + \\ &\sum_{JKL} \chi^{(3)}_{IJKL}(-\omega_1;\omega_2,\omega_3,\omega_4) E_J(\omega_2) E_K(\omega_3) E_L(\omega_4) + \ldots \end{aligned} \tag{1.5}$$

By converting to the frequency domain, the frequencies are explicitly written giving intuition into the field interactions. For example, we can see two fields are required to drive a $\chi^{(2)}$ process, resulting in the creation of a third field. For this reason, the process is referred to as a three-wave mixing process. SHG, SFG, and difference frequency generation (DFG) are all examples of fields generated from this interaction. Four-wave mixing processes are due to third-order nonlinearities, $\chi^{(3)}$.[45] TPA and pump-probe dynamics are examples of four-wave mixing processes. While the optical response of crystal structures may be easily understood in terms of the bulk polarization description,

relating the nonlinear susceptibilities to the structure of small molecules is not obvious. For this case, the polarization can be explicitly written along the ith molecular axis in the microscopic domain

$$P_i(\omega_1) = \sum_j \alpha_{ij}(-\omega_1;\omega_2)E_j(\omega_2) + \sum_{jk} \beta_{ijk}(-\omega_1;\omega_2,\omega_3)E_j(\omega_2)E_k(\omega_3) + \sum_{jkl} \gamma_{ijkl}(-\omega_1;\omega_2,\omega_3,\omega_4)E_j(\omega_2)E_k(\omega_3)E_l(\omega_4) + \ldots \quad (1.6)$$

where α is the linear polarizability, β is called the first hyperpolarizability, and γ is the second hyperpolarizability tensor. These two equations are shown to be equivalent when substituting the nonlinear susceptibility with the local polarizability.[46]

A majority of the work presented in this dissertation will focus on three-wave and four-wave mixing processes. Specifically, TPEF and pump-probe kinetics will be our primary focus. Controlling the properties of the incident light will enable us to drive specific responses from the materials that will be used as imaging modalities.[40] Later, materials will be designed to interact with light in specific manner for applications as biological contrast agents as well as low-pass filters for defense applications.[13,51] A Jablonski diagram (state diagram) is used to illustrate possible electronic pathways associated with a molecule as well as some of the possible multiphoton processes (figure 1.3).[46]

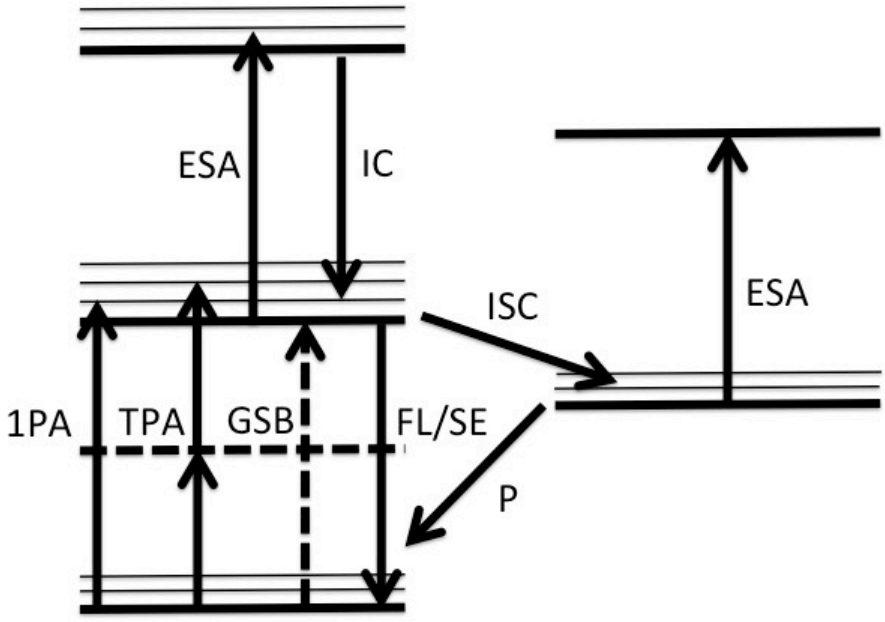

Figure 1.3 Jablonski diagram illustrating one photon absorption (1PA), two photon absorption (TPA), ground state bleach (GSB), fluorescence (FL), stimulated emission (SE), excited state absorption (ESA), intersystem crossing (ISC), and Phosphorescence (P).

1.3 Two-Photon Absorption

Two-photon absorption was first predicted by Maria Goppert-Mayer and published in her doctoral dissertation in 1931.[47] It wasn't until 1961, when lasers became available that the first experimental observation of TPEF was demonstrated.[48] Today, TPEF is a standard technique used in modern microscopy laboratories. TPA is illustrated in the state diagram in figure 1.3.

As was described earlier, two fields drive a nonlinear transition resulting in an excited state population. The polarization from this interaction is described as

$$P_i(\omega_4) = (3/4)\,\mathrm{Im}\left[\chi^{(3)}_{iikk}(-\omega;\omega,\omega,-\omega)\right]E_i(\omega)\left|E_k(\omega)\right|^2 \qquad (1.7)$$

The constructive interference of the two fields does not require a resonant intermediate state (eigenstate of the system), as in the case of SHG. Yet unlike SHG, two-photon

absorption is a four-wave mixing process, $\chi^{(3)}$. The additional field arises from the difference in the ground state and excited state dipole moments.[49] Parity selection rules limit two-photon transitions to non-centrosymmetric molecules, which is not a limitation to most GFP-variants due to their lack of centrosymmetry. When the selection rules are obeyed, the two-photon transition probability may be written as

$$P \propto \left| \sum_{k} \frac{\mu_{mk}\mu_{kn}E^2}{\omega_{kn} - \omega} \right|^2 \tag{1.8}$$

where all possible intermediate virtual states, k, are summed with respect to the two dipole moments, μ, and the transition frequency, ω_{kn}. The fluorescence signal resulting from the two-photon excitation is approximated by

$$S \propto \sigma_{TPA}(\omega) \left| E^{(2)}(\omega) \right|^2 \tag{1.9}$$

where $\sigma_{TPA}(\omega)$ is the two-photon cross-section and $\left|E^{(2)}(\omega)\right|^2$ is the second harmonic power spectrum of the laser pulse. The rate of absorption due to a two-photon transition can be described in terms of the differential equation

$$\frac{dI}{dz} = \xi I^2 \tag{1.10}$$

Here, I is the intensity of the driving field, z is the optical path length, and ξ is the two-photon absorption coefficient that is proportional to the imaginary part of the averaged second-order polarizability, $\xi = \langle \mathrm{Im}(\gamma) \rangle$.[50] The two-photon cross-section can then be defined as

$$\sigma_{TPA} = \frac{\hbar\omega}{N}\xi \tag{1.11}$$

where $\hbar\omega$ is the energy the excitation field and N is the number density of scatters. The units of a two-photon cross-section are in terms of Goeppert-Mayer ($1GM = 10^{-50} cm^4 s$).

1.4 Pump-Probe Pathways

Transient absorption pathways offer multiple routes as imaging modalities. As a four-wave mixing process, the induced polarization may be described as

$$P_i^{(3)}(\omega_4) = \varepsilon_0 \chi_{ijkl}^{(3)} E_j(\omega_3) E_k(\omega_2) E_l(\omega_1) \tag{1.12}$$

In the pump-probe geometry, two of the fields are degenerate. The resulting pathways are excited state absorption (ESA), ground state bleach (GSB) and stimulated emission (SE), as shown in figure 1.3. ESA is a multi-photon transition requiring a resonant intermediate state. Higher lying excited states may not be resonant with the probe frequency, and if the ground state has been depleted, a GSB signal may be detected. SE depopulates an excited state, yielding emission collinear with the probe beam. The lifetimes of these kinetic pathways give insight into a molecule's properties.[51] Recently, these pathways have been used as imaging modalities where endogenous chemical constituents act as contrast agents.[52] Pump-probe imaging is an attractive technique, as it does not require a material to be fluorescent or require the addition of fluorescent tags. Recently the technique has found applications to melanoma detection[53], the study of dynamics in polymer blends for optoelectronics applications[54], imaging of red blood cells[52], and imaging of non-fluorescent chromoproteins.[55] Unfortunately, many transient dynamics are on the sub-100fs time scale and cannot be resolved with current methods.[39]

Pulse-shaping-based pump-probe microscopy offers a route towards imaging such ultrafast dynamics.

1.5 Dissertation Outline and Chapter Overview

In this dissertation, the theory and applications of pulse-shaping-based nonlinear microscopy are presented. The technique is applied to the imaging of live COS 7 cells expressing two-photon absorbing fluorophores, where two-photon FRET stoichiometry is demonstrated. Chemical contrast imaging using pulse shaping based pump-probe spectroscopy is then used to image cells using endogenous cellular contrast agents. The synthesis of two-photon active GFP-type chromophores is discussed in terms of the effects of functional groups substitution position and relative bulk size. Finally, multidimensional supramolecular metallacycles were studied using various ultrafast spectroscopy techniques and found to have potential for applications as nonlinear optical materials.

Chapter 2 provides an overview of pulse shaping to nonlinear microscopy. The theory, development and applications are discussed in detail. Experimental techniques for dispersion compensation and selective excitations are illustrated using SHG signals. Genetic algorithms are used to converge to the ideal phase mask for selective excitation.

Chapter 3 describes the theory and application of pulse-shaping based two-photon FRET stoichiometry. The technique enables the quantification of donor and acceptor in construct in the presence of crosstalk. Cells transfected with mAmetrine, tdTomato and mAmetrine-tdTomato linked construct were imaged and stoichiometric values determined.

Chapter 4 presents chemical-contrast imaging with pulse shaping based pump-probe spectroscopy. An additional pulse shaper is developed and described in detail. As a two-color pump-probe technique, the system uses two separate pulse shapers to image red blood cells using the endogenous heme proteins as contrast agents. ESA, GSB and a thermal lensing mechanism are used as imaging modalities.

Chapter 5 contains a discussion on the synthesis of TPA green fluorescent protein-type fluorophores. Steady-state spectroscopy, fluorescence quantum yields, and time-resolved fluorescence lifetimes of synthesized fluorophores are extensively investigated. These molecules show promise as biological markers for application in the study of conformation changes and aggregation of amyloid peptides, known to play an important role in many neurodegenerative diseases.

In chapter 6 the ultrafast dynamics of platinum containing metallacycles have been investigated by femtosecond fluorescence upconversion and transient absorption. These measurements were carried out in an effort to probe the charge transfer dynamics and the rate of intersystem crossing in metallacycles with different geometries and dimensions. The results show potential for new, longer lived excited state materials with applications to new electronic and optical limiting materials.

Chapter 7 reviews the work presented in this dissertation and gives an outlook to future techniques and applications.

References:

[1] Mertz, J., [Introduction to Optical Microscopy], Roberts & Company (2010).

[2] Biological Engineering Division Massachusetts Institute of Technology Barry R. Masters Visiting Scientist, Peter So Professor of Mechanical and Biological Engineering Massachusetts Institute of Technology, [Handbook of Biomedical Nonlinear Optical Microscopy], Oxford University Press (2008).

[3] Rust, M.J., Bates, M., and Zhuang, X., "Sub-diffraction-limit imaging by stochastic optical reconstruction microscopy (STORM)," Nature Methods 3(10), 793–796 (2006).

[4] Willig, K.I., Kellner, R.R., Medda, R., Hein, B., Jakobs, S., and Hell, S.W., "Nanoscale resolution in GFP-based microscopy," Nature Methods 3(9), 721–723 (2006).

[5] Minsky, M., "Memoir on inventing the confocal scanning microscope," Scanning (1988).

[6] Cremer, C., and Cremer, T., "Considerations on a Laser-Scanning-Microscope with High-Resolution and Depth of Field," Microscopica Acta 81(1), 31–44 (1978).

[7] Denk, W., Strickler, J.H., and Webb, W.W., "Two-photon laser scanning fluorescence microscopy," Science (1990).

[8] Kawano, H., Kogure, T., Abe, Y., Mizuno, H., and Miyawaki, A., "Two-photon dual-color imaging using fluorescent proteins," Nature Methods (2008).

[9] Ogilvie, J.P., Debarre, D., Solinas, X., Martin, J.L., Beaurepaire, E., and Joffre, M., "Use of coherent control for selective two-photon fluorescence microscopy in live organisms," Optics Express 14(2), 759–766 (2006).

[10] Heim, R., Cubitt, A.B., and Tsien, R.Y., "Improved green fluorescence," Nature 373, (1995).

[11] Ormö, M., Cubitt, A.B., Kallio, K., Gross, L.A., and Tsien, R.Y., "Crystal structure of the Aequorea victoria green fluorescent protein," Science (1996).

[12] Tsien, R.Y., "The green fluorescent protein," Annual review of biochemistry (1998).

[13] Clark, T.B., Orr, M.E., Flynn, D.C., and Goodson, T., III, "Synthesis and Optical Properties of Two-Photon Absorbing GFP-type Probes," The Journal of Physical Chemistry C 115(15), 7331–7338 (2011).

[14] Makarov, N.S., Hughes, T., and Rebane, A., "Resonance enhancement of two-photon absorption in fluorescent proteins," The Journal of Physical Chemistry B 111, (2007).

[15] Drobizhev, M., Makarov, N.S., Tillo, S.E., Hughes, T.E., and Rebane, A., "Two-photon absorption properties of fluorescent proteins," Nature Methods 8(5), 393–399 (2011).

[16] Tillo, S.E., Hughes, T.E., Makarov, N.S., and Rebane, A., "A new approach to dual-color two-photon microscopy with fluorescent proteins," BMC … (2010).

[17] Entenberg, D., Wyckoff, J., Gligorijevic, B., Roussos, E.T., Verkhusha, V.V., Pollard, J.W., and Condeelis, J., "Setup and use of a two-laser multiphoton microscope for multichannel intravital fluorescence imaging," Nature Protocols 6(10), 1500–1520 (2011).
[18] Sahai, E., Wyckoff, J., Philippar, U., and Segall, J.E., "Simultaneous imaging of GFP, CFP and collagen in tumors in vivo using multiphoton microscopy," BMC … (2005).
[19] Stryer, L., "Fluorescence energy transfer as a spectroscopic ruler," Annual review of biochemistry (1978).
[20] Jovin, T.M., and Arndt-Jovin, D.J., "Luminescence digital imaging microscopy," Annual review of biophysics and Chemistry (1989).
[21] Herman, B., "Resonance energy transfer microscopy," Methods Cell Biol (1989).
[22] Jares-Erijman, E.A., and Jovin, T.M., "FRET imaging," Nature biotechnology 21(11), 1387–1395 (2003).
[23] Mátyus, L., "New trends in photobiology: Fluorescence resonance energy transfer measurements on cell surfaces. A spectroscopic tool for determining protein interactions," Journal of Photochemistry and Photobiology B: Biology (1992).
[24] Selvin, P.R., "The renaissance of fluorescence resonance energy transfer," Nature structural biology (2000).
[25] Hoppe, A., Christensen, K., and Swanson, J.A., "Fluorescence Resonance Energy Transfer-Based Stoichiometry in Living Cells," Biophysical Journal 83(6), 3652–3664 (2002).
[26] Erickson, M.G., Alseikhan, B.A., Peterson, B.Z., and Yue, D.T., "Preassociation of Calmodulin with Voltage-Gated Ca 2+ Channels Revealed by FRET in Single Living Cells," Neuron (2001).
[27] Raicu, V., Jansma, D., Miller, D., and Friesen, J., "Protein interaction quantified in vivo by spectrally resolved fluorescence resonance energy transfer," Biochemistry Journal(385), 1 April 2005,
[28] Volkmer, A., Subramaniam, V., Birch, D., and Jovin, T.M., "One-and two-photon excited fluorescence lifetimes and anisotropy decays of green fluorescent proteins," Biophysical Journal (2000).
[29] Brenner, M.H., Cai, D., Swanson, J.A., and Ogilvie, J.P., "Two-photon imaging of multiple fluorescent proteins by phase-shaping and linear unmixing with a single broadband laser," Optics Express 21(14), 17256–17264 (2013).
[30] Campagnola, P.J., and Loew, L.M., "Second-harmonic imaging microscopy for visualizing biomolecular arrays in cells, tissues and organisms," Nature biotechnology (2003).
[31] Débarre, D., Supatto, W., Pena, A.-M., Fabre, A., Tordjmann, T., Combettes, L., Schanne-Klein, M.-C., and Beaurepaire, E., "Imaging lipid bodies in cells and tissues using third-harmonic generation microscopy," Nature Methods 3(1), 47–53 (2006).
[32] Squier, J.A., Muller, M., Brakenhoff, G.J., and Wilson, K.R., "Third harmonic generation microscopy," Optics Express 3(9), 315–324 (1998).
[33] Muller, M., Squier, J., Wilson, K.R., and Brakenhoff, G.J., "3D microscopy of transparent objects using third-harmonic generation," Journal of Microscopy-

Oxford 191, 266–274 (1998).
[34] Evans, C.L., Xu, X., Kesari, S., Xie, X.S., and Wong, S., "Chemically-selective imaging of brain structures with CARS microscopy," Optics … (2007).
[35] Ogilvie, J.P., Beaurepaire, E., Alexandrou, A., and Joffre, M., "Fourier-transform coherent anti-Stokes Raman scattering microscopy," Optics Letters 31, 1–3 (2006).
[36] Fischer, M.C., Liu, H.C., Piletic, I.R., and Escobedo-Lozoya, Y., "Self-phase modulation signatures of neuronal activity," Optics Letters 33, 219–221 (2008).
[37] Cui, M., Joffre, M., Skodack, J., and Ogilvie, J.P., "Interferometric Fourier transform coherent anti- stokes Raman scattering," Optics Express1–11 (2006).
[38] Fu, D., Ye, T., Matthews, T.E., Yurtsever, G., and Warren, W.S., "Two-color, two-photon, and excited-state absorption microscopy," Journal of Biomedical Optics 12(5), 054004 (2007).
[39] Min, W., Freudiger, C.W., Lu, S., and Xie, X.S., "Coherent Nonlinear Optical Imaging: Beyond Fluorescence Microscopy," Annual review of physical chemistry 62(1), 507–530 (2011).
[40] Flynn, D.C., Bhagwat, A.R., and Ogilvie, J.P., "Chemical-contrast imaging with pulse-shaping based pump-probe spectroscopy," presented at SPIE BiOS, 22 February 2013, 85881Z–85881Z–10.
[41] van Munster, E.B., and Gadella, T.W.J., [Fluorescence Lifetime Imaging Microscopy (FLIM)], in Advances in Biochemical Engineering/Biotechnology 95(Chapter 6), Springer Berlin Heidelberg, Berlin, Heidelberg, 143–175 (2005).
[42] Pillai, R.S., Boudoux, C., Labroille, G., Olivier, N., Veilleux, I., Farge, E., Joffre, M., and Beaurepaire, E., "Multiplexed two-photon microscopy of dynamic biological samples with shaped broadband pulses," Optics Express 17(15), 12741–12752 (2009).
[43] Walowicz, K.A., Pastirk, I., Lozovoy, V.V., and Dantus, M., "Multiphoton intrapulse interference. 1. Control of multiphoton processes in condensed phases," Journal of Physical Chemistry A 106(41), 9369–9373 (2002).
[44] Zewail, A.H., "Femtochemistry: Atomic-Scale Dynamics of the Chemical Bond Using Ultrafast Lasers (Nobel Lecture) - Zewail - 2000 - Angewandte Chemie International Edition - Wiley Online Library," Angewandte Chemie International Edition (2000).
[45] Maker, P., and Terhune, R., "Study of Optical Effects Due to an Induced Polarization Third Order in the Electric Field Strength," Phys.Rev. 137(3A), A801–A818 (1965).
[46] Nalwa, H.S., and Miyata, S., [Nonlinear Optics of Organic Molecules and Polymers], CRC Press (1996).
[47] Göppert-Mayer, M., "Elementary processes with two quantum transitions" 18(7-8), 466–479 (2009).
[48] Kaiser, W., and Garrett, C., "Two-Photon Excitation in CaF_{2}: Eu^{2+}," Physical Review Letters 7(6), 229–231 (1961).
[49] Drobizhev, M., Makarov, N.S., Tillo, S.E., Hughes, T.E., and Rebane, A., "Describing Two-Photon Absorptivity of Fluorescent Proteins with a New Vibronic Coupling Mechanism," Journal of Physical Chemistry B 116(5), 1736–1744 (2012).

[50] Papadopoulos, M.G., Sadlej, A.J., and Leszczynski, J., [Non-Linear Optical Properties of Matter], Springer (2007).
[51] Flynn, D.C., Ramakrishna, G., Yang, H.-B., Northrop, B.H., Stang, P.J., and Goodson, T., III, "Ultrafast Optical Excitations In Supramolecular Metallacycles with Charge Transfer Properties" 132(4), 1348–1358 (2010).
[52] Ye, T., Fu, D., and Warren, W.S., "Nonlinear Absorption Microscopy†," Photochemistry and Photobiology 85(3), 631–645 (2009).
[53] Matthews, T.E., Piletic, I.R., Selim, M.A., Simpson, M.J., and Warren, W.S., "Pump-Probe Imaging Differentiates Melanoma from Melanocytic Nevi," Science Translational Medicine 3(71), 71ra15–71ra15 (2011).
[54] Polli, D., Grancini, G., Clark, J., Celebrano, M., Virgili, T., Cerullo, G., and Lanzani, G., "Nanoscale Imaging of the Interface Dynamics in Polymer Blends by Femtosecond Pump-Probe Confocal Microscopy," Advanced Materials 22(28), 3048–3051 (2010).
[55] Min, W., Lu, S., Chong, S., Roy, R., Holtom, G.R., and Xie, X.S., "Imaging chromophores with undetectable fluorescence by stimulated emission microscopy," Nature 461(7267), 1105–1109 (2009).

Chapter 2 Pulse Shaping

2.1 Introduction

Only a few years after the first laser was demonstrated in 1960, picosecond pulsed lasers began to be developed.[1,2] The nature of these pulses of light gave researchers access to a long sought-after goal: controlling chemical reactions with light.[3] Short pulse durations have high peak intensities that can drive specific nonlinear transitions in molecules. Since the 1980s, various methods have been devised for manipulating light to obtain today's few femtosecond pulses. Multiple reviews on these techniques can be found in the literature.[4,5]

The phase of light has been shown to be an important variable for controlling light-matter interactions beyond stimulated emission.[6] Using spectral phase manipulation, the analogy of a musical score can be used to describe the optical control of a laser pulse (figure 2.1). The ability to tune pulse shapes to drive specific nonlinear molecular interactions has resulted in the rebirth of coherent control.[7] For example, the technique has been used to optically control molecular dissociation and ionization pathways[8], semiconductor current[9], emission direction[10], refine molecules to a certain state, and atomic wave packets.[11] More recently, the technique has found biological applications.[12,13]

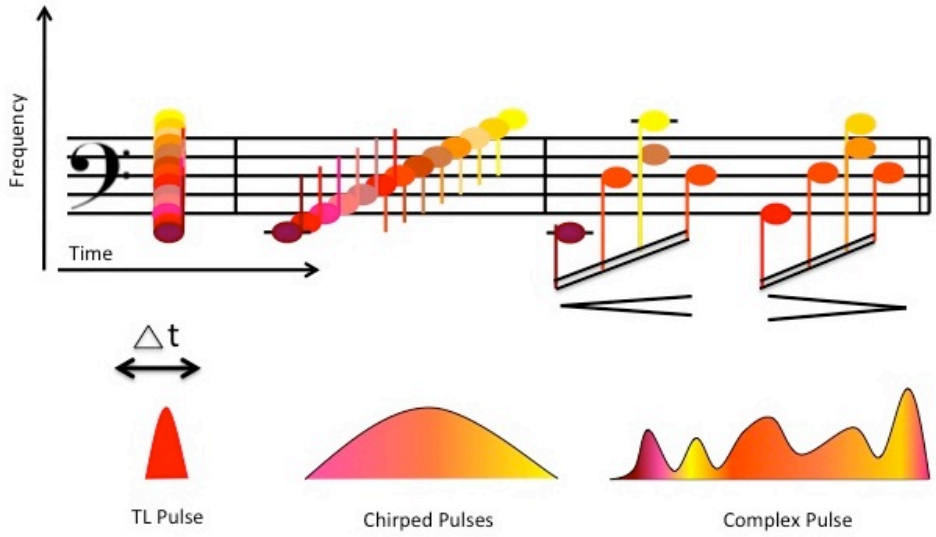

Figure 2.1 Pulse shaping analogy to that of a musical score

The electronic structure of a material determines its nonlinear response to a pulse shape. This section discusses pulse shaping with respect to one-photon and multi-photon transitions as well as TPA via virtual intermediate states. Assuming pulse durations shorter than the lifetime of an excited state, the analytical expression for the excited state population, a_f via a one-photon transition is explicitly given by

$$a_f \propto \frac{\mu_{fg}}{i\hbar}\int_{-\infty}^{t} E(t)\exp(-i\omega_0 t_1)dt \tag{2.1}$$

where $\omega_0 = (E_f - E_g)/\hbar$ representing the transition frequency, μ_{fg} is the dipole moment, $E(t)$ is the electric field amplitude, and $\exp(-i\omega_0 t_1)$ is the phase.[14,15] The Fourier components of the electric field, E, are at $\pm\omega_0$ illustrating a one-photon transition is independent of the spectral phase of the field. For this reason, only amplitude shaping can be used for selective one-photon excitation.

When there are no resonant one-photon transitions, a two-photon transition may be possible. In this case, the excited state population is explicitly given by

$$a_f \propto \frac{-1}{\hbar^2}\sum_n \mu_{fn}\mu_{ng}\int_{-\infty}^{t}\int_{-\infty}^{t} E(t_1)E(t_2)\times\exp\left(i\omega_{fn}t_1\right)\exp\left(i\omega_{ng}t_2\right)dt_1dt_2 \tag{2.2}$$

where the variables μ_{ng} and μ_{fn} are the dipole moment matrix elements between the ground state and intermediate state and intermediate state and final state respectfully. Since TPA is a nonresonant transition, the previous equation may be rewritten as[16]

$$a_f = \frac{-1}{\hbar^2}\sum_n \frac{\mu_{fn}\mu_{ng}}{\omega_{ng}-\omega/2}\int_{-\infty}^{\infty}\tilde{E}(\Omega)\tilde{E}(\omega-\Omega)d\Omega \tag{2.3}$$

where $\tilde{E}(\Omega)$, the electric field in the frequency domain, is the Fourier transform of $E(t)$. The amplitude of the excited state population can then be written in terms of a transition probability, $P_{TPA}=\left|a_f\right|^2$ resulting in the relation[15,17]

$$P_{TPA} = \frac{1}{\hbar^4}\left|\sum_n \frac{\mu_{fn}\mu_{ng}}{\omega_{ng}-\omega/2}\right|^2\left|\int_{-\infty}^{\infty}\tilde{E}(\Omega)\tilde{E}(\omega-\Omega)d\Omega\right|^2 \tag{2.4}$$

This equation has the form of $P_{TPA}(\omega)=g_{TPA}(\omega)S_2(\omega)$, where the components are

$$g_{TPA}(\omega)=\frac{1}{\hbar^4}\left|\sum_n \frac{\mu_{fn}\mu_{ng}}{\omega_{ng}-\omega/2}\right|^2 \tag{2.5}$$

$$S_2(\omega)=\left|\int_{-\infty}^{\infty}\tilde{E}(\Omega)\tilde{E}(\omega-\Omega)d\Omega\right|^2 \tag{2.6}$$

Since the excitation occurs into a distribution of final states (spectral density of states) $\rho(\omega)$, the transition probability is a convolution of the form

$$P_{TPA} \approx \int g_{TPA}(\omega) S_2(\omega) \rho(\omega) d\omega \tag{2.7}$$

where the two-photon cross-section can be directly related to the terms in equation 2.7 by $\sigma_{TPA} \propto g_{TPA}(\omega)\rho(\omega)$.[18,19]

Using phase shaping, we can manipulate the two-photon transition probability by altering the second order electric field, S_2, which contains the E^2 dependence from the two fields. To illustrate this process, the electric field term from equation 2.6, $\tilde{E}(\omega)$, can be expanded as $\tilde{E}(\Omega) = A(\Omega)\exp\left(i\Phi(\Omega)\right)$ where $A(\Omega)$ and $\Phi(\Omega)$ represent the spectral amplitude and spectral phase, respectfully. By explicitly defining the second order electric field as

$$S_2(\omega) = \left| \int_{-\infty}^{\infty} A(\omega/2 + \Omega) A(\omega/2 + \Omega) \exp\left[i\left(\Phi(\omega/2 + \Omega) + \Phi(\omega/2 - \Omega) \right) \right] d\Omega \right|^2 \tag{2.8}$$

we can see how two photons centered around half the transition frequency ω can sum to reach the total frequency, $\omega = (\omega/2 + \Omega) + (\omega/2 - \Omega)$. Broadband pulses containing many frequency components can have a multitude of combinations from different frequencies adding up to a two-photon transition frequency (figure 2.2).

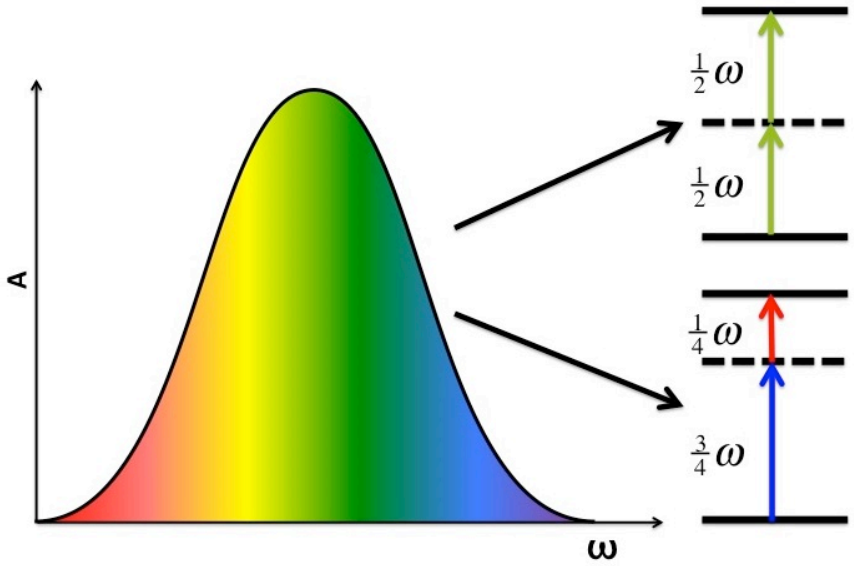

Figure 2.2 Example of fundamental field combinations for TPA. A cartoon of a broadband Gaussian pulse in the frequency domain is shown on the left. On the right, two state diagrams illustrate possible two-photon transitions from individual fields within the broadband pulse.

Analysis of equation 2.8 gives insight into the second order electric field spectral phase dependence. For example, it can be seen that a constant spectral phase results in the constructive interference of all frequency components producing a broadband (maximized) SH field. Deviation from a flat spectral phase directly affect S_2 and the resulting transition probability. In such a case, frequency components with the same spectral phase will constructively interfere, while frequency components out of phase will destructively interfere resulting in the excitation of specific states. The symmetry of the spectral phase can greatly affect the two-photon transition probability.[12,14,20] For example, an antisymmetic spectral phase function having the property

$$\Phi\left(\omega/2+\Omega\right)=-\Phi\left(\omega/2-\Omega\right) \tag{2.9}$$

will result in the cancelation of the exponential terms in equation 2.8. A pulse with this spectral phase will be temporally broadened while having a two-photon transition probability equivalent to that of a TL pulse.[15] Symmetry arguments can also be used for selective excitation.[20] In the case of a resonant two-photon transition (ESA), a TL pulse has been shown to not maximize the excited state population.[16] Furthermore, some molecules exhibit increased fluorescence using chirped excitation pulses. Using positively chirped pulses, green fluorescent proteins were shown to have 50% more population in the excited state.[21] As the mechanism responsible for the four-wave mixing process is third-order polarization, many other pathways may also be accessible. Moreover, given sufficient intensity and nonlinear susceptibility of the material, our description may be extended to higher-order processes, described by the more general description

$$P_{g\to f} \propto \left| \int_{-\infty}^{\infty} E^{n}(t) \exp(i\omega_0 t)\, dt \right|^2 \tag{2.10}$$

This chapter will focus on the use of pulse shaping for dispersion compensation of microscope optics and the selective excitation of fluorescent proteins via TPA. The chapter begins with a discussion on how to measure selective excitation and pulse compression with SHG. Next, the pulse shaper and a spatial light modulator (SLM) are discussed in detail. Dispersion from microscope optics and the effect it has on a laser pulse shape are then described. This leads to a discussion on pulse compression and selective excitation techniques.

2.2 SHG as a Measure of Selective Excitation

SHG has been demonstrated to be good measure of selective excitation and pulse compression.[20] In the previous section, the convolution of the second-order electric field with a two-photon cross-section was shown to determine the two-photon transition probability. The same pulse shape optimized for selective SHG can therefore be applied to TPA-dyes. The state diagram and geometry of interaction for SHG is illustrated in figure 2.3.

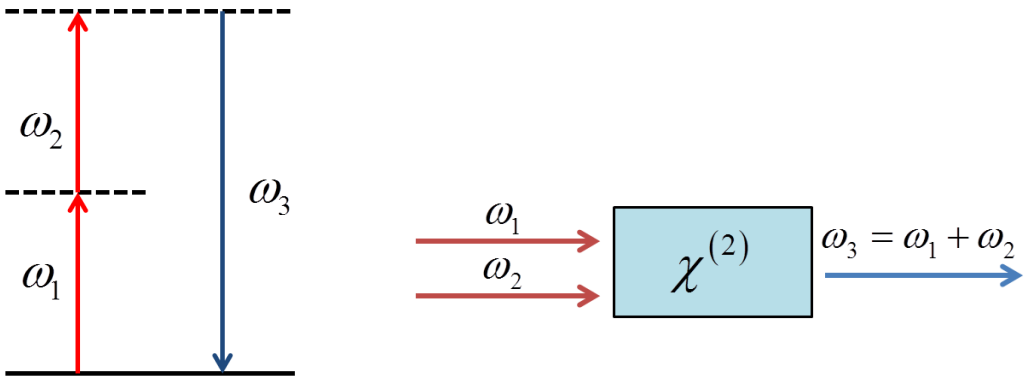

Figure 2.3 SHG energy level diagram and geometry of interaction.

The nonlinear interaction for SHG is described by the relationship

$$E_2(\omega_2) \propto \int E_1(\omega_1) E_1(\omega_2 - \omega_1) d\omega_1 \tag{2.11}$$

where the two fields, E_1, are described by

$$E_1(\omega_1) \approx \exp\left[-\left(\frac{\omega_1}{\Delta\omega_1}\right)^2\right] \times \exp\left[iA\cos\left(\Delta t \cdot \omega_1 + \phi(\omega_1)\right)\right] \tag{2.12}$$

where ω_1 is the frequency with respect to the central frequency, $\Delta\omega_1$ is the spectral width, A is the amplitude, $\phi(\omega)$ is the phase and Δt the inverse of the repetition rate.[22] The resulting SH field, E_2, has been shown to be approximately

$$E_2(\omega_2) \approx \exp\left[-\frac{1}{2}\left(\frac{\omega_2}{\Delta\omega_1}\right)^2\right] \times J_0\left(2A\cos\left(\frac{1}{2}\Delta t \cdot \omega_2 + \varphi(\omega_2)\right)\right) \tag{2.13}$$

The SH field no longer carries the phase modulation of the fundamental fields. Instead, the SH field is amplitude modulated by the zero-order Bessel function, J_0. By altering the phase term, $\varphi(\omega)$, the fundamental fields constructively and destructively interfere allowing control of the SH spectrum. The relationship $S_2(\omega) = |E_2(\omega)|^2$ enables us to calculate the transition probability for non-resonant TPA in molecular systems of interest, from the SH spectra of a nonlinear crystal.

There is an important distinction between phase modulation and amplitude modulation for pulse shaping. The former allows us to obtain narrow selective excitations within the transform limit of the SH. Amplitude modulation requires removing intensity from specific frequency components. The convolution of amplitude modulated fundamental fields smears out the intended excitation and fails to obtain narrow selective excitations. Furthermore, unlike phase shaping, amplitude shaping reduces power from the fields.

2.3 Phase Shaping Method

Phase shaping is the process of manipulating a waveform's phase to have a specific temporal shape. There exist both static and dynamic pulse shaping techniques for this purpose. Static techniques include the use of prisms, chirped mirror, and

gratings. Static pulse shaping is used in chapters five and six of this dissertation for generating laser pulses with 100 fs durations.

Recent advances in dispersion compensating materials have resulted in lasers with sub-8 fs pulse durations.[23] The broad bandwidth enables the excitation of a wide range of materials of interest for microscopy. The work described in chapters three and four will use a broadband Ti:Sapphire laser (Venteon: Pulse One Oscillator) as a light source. This laser replaces prisms with chirped mirrors that support transform-limited (TL) pulses having greater than 300 nm bandwidth. The oscillator uses passive modulation where the optical Kerr effect generates extra frequencies through SPM.[5] Chirped mirrors ensure the effects of dispersion from SPM are compensated and the modes remain in phase constructively interfering to make pulses. When the cavity is properly aligned, the laser output approaches the TL, as approximated by the time-bandwidth product, $TBP \leq \Delta t \cdot \Delta\omega$, (TBP = 0.44) resulting in pulse durations of less than 8 fs and having maximum peak power.

Dynamic pulse shaping techniques reviewed extensively by Weiner include the use of spatial light modulators, deformable mirrors, and acousto-optic modulators.[24,25] In these cases, the pulse shaper acts as a programmable dynamic filter, where a waveform may be synthesized according to user specifications.[26] In this dissertation, pulse shaping is performed using an SLM integrated into a 4-f pulse-shaper optical device (figure 2.4). A diffraction grating angularly disperses a broadband laser pulse, which is collimated and focused onto the SLM. The lens Fourier transforms the angular dispersion to spatially dispersed frequencies onto the SLM. A static phase mask on the SLM, at the Fourier plane of the lens, imparts a spectral phase to the pulse of light. A second lens and grating

spatially recombine the altered beam of light. Symmetry across the filter (SLM) ensures the optic ensemble is in a zero dispersion configuration.[24] In this manner, if the SLM were to be removed the input pulse and output pulse should be identical.

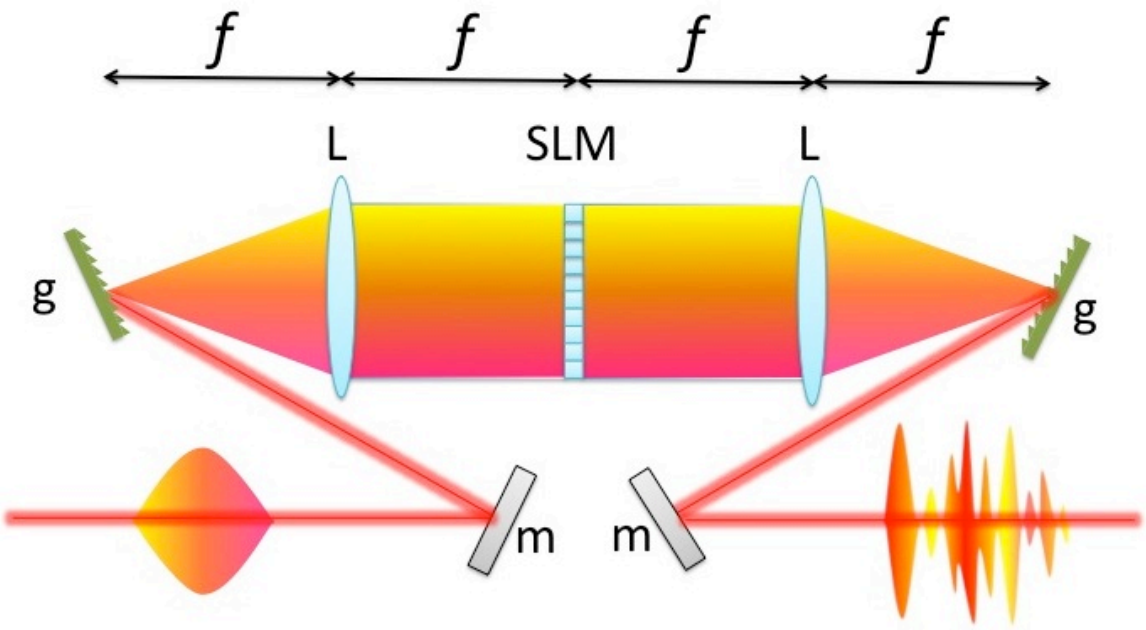

Figure 2.4 Diagram of a 4f pulse shaper. The input beam is spatial dispersed with a grating and Fourier transformed into the frequency domain with a lens. A spatial light modulator manipulates the spectral phase of the individual frequency components at the Fourier plane and then recombined.

Our pulse shaper was assembled by Biophotonics Solutions Inc. and includes a Perkin Elmer (Phase only) SLM as our dynamic Fourier filter. The pulse shaper is in the folded geometry, requiring only one grating and spherical mirror as seen in figure 2.5.[27] In this configuration, the pulse propagates through the SLM twice doubling the possible optical retardance.

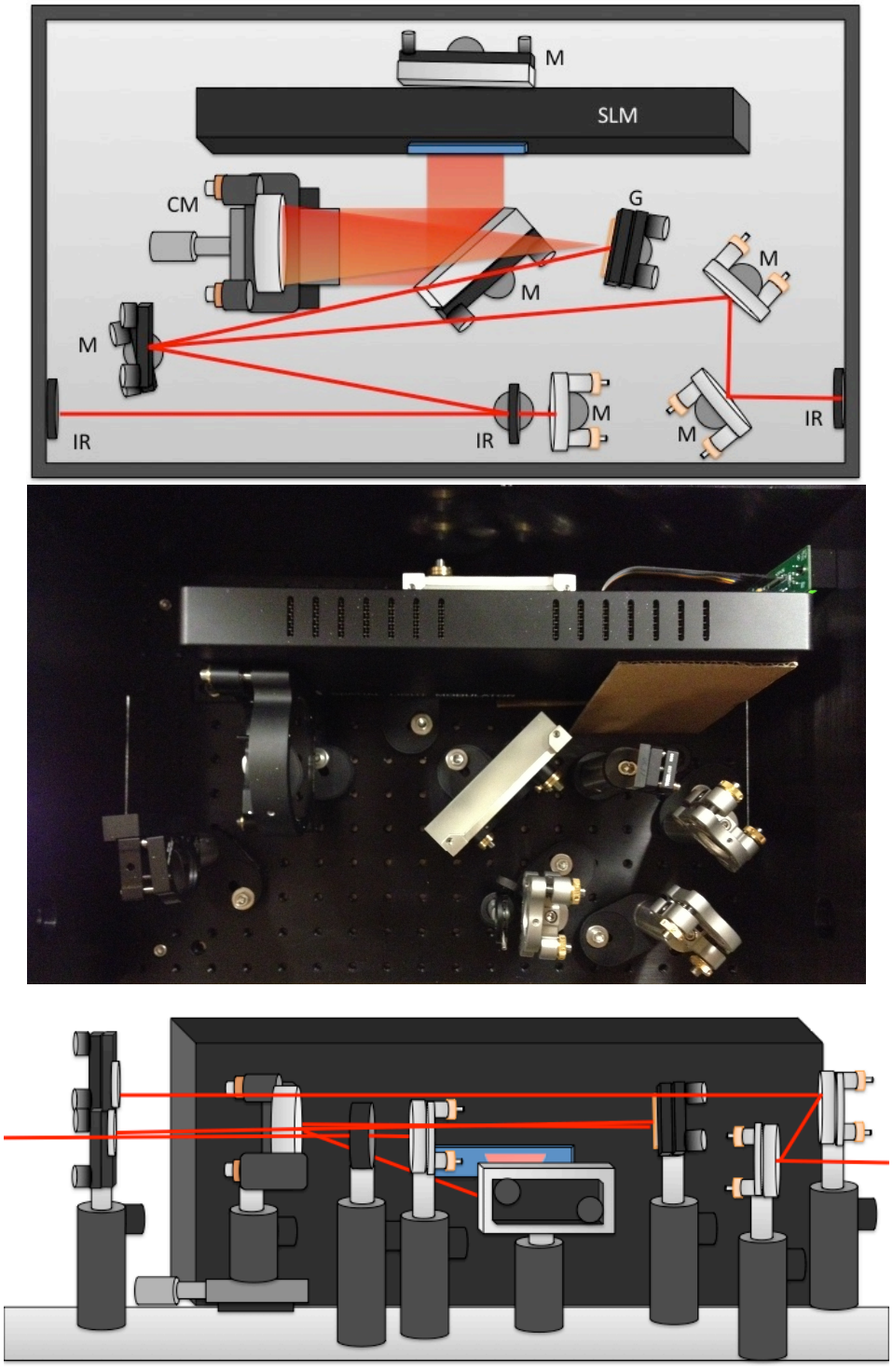

Figure 2.5 Pulse shaper geometry. Top: Top-down perspective of pulse shaper schematic, including flat mirrors (m), curved mirrors (cm), spatial light modulator (SLM), grating (G), and irises (IR). Middle: Picture of pulse shaper from top-down perspective. Bottom: Side view perspective of pulse shaper schematic.

The Perkin Elmer SLM-640 modulates light using nematic liquid crystals (LC) to alter the spectral phase.[28,29] The LC orientation is controlled at each of the 640 pixels by discrete voltages.

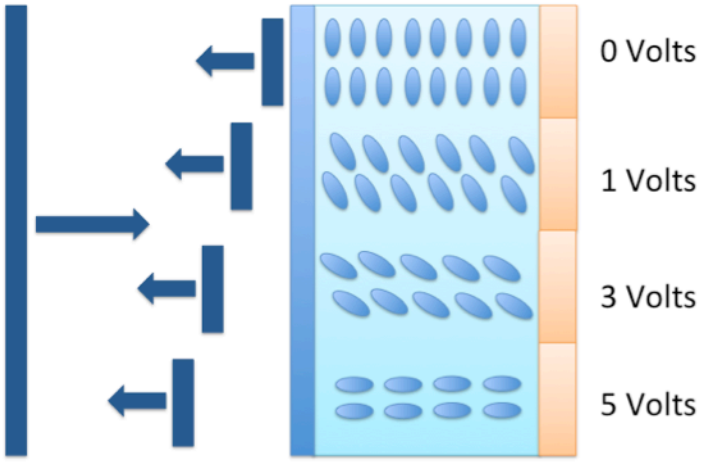

Figure 2.6 SLM liquid crystal cartoon illustrating liquid crystal response to voltage and associated spectral phase delay

The index of refraction is controlled by the LC's voltage sensitive extraordinary axis, while the index of refraction polarized along the orthogonal axis remains unchanged (figure 2.6). The liquid crystals have a response time of 35ms (2π radians at 900nm). The controlling electronics operate with a 12-bit (4096 levels) enabling a high degree of precision.

The grating equation describes the distribution of wavelength onto the SLM by the relationship

$$m\lambda = d(\sin\alpha + \sin\beta) \tag{2.14}$$

where m is the diffraction order, d is the spot size, and α is the angle from normal incidence and β is the diffraction angle.[30] The spectral phase should be applied in the

frequency domain due to the Fourier relationship between time and frequency. As the relationship between wavelength and frequency is nonlinear, $\nu = {}^{2\pi c}/_{\lambda}$, the applied spectral phase mask should be displayed in the frequency domain. An example of a spectral phase mask mapped from the wavelength domain to the frequency domain is illustrated in figure 2.7.

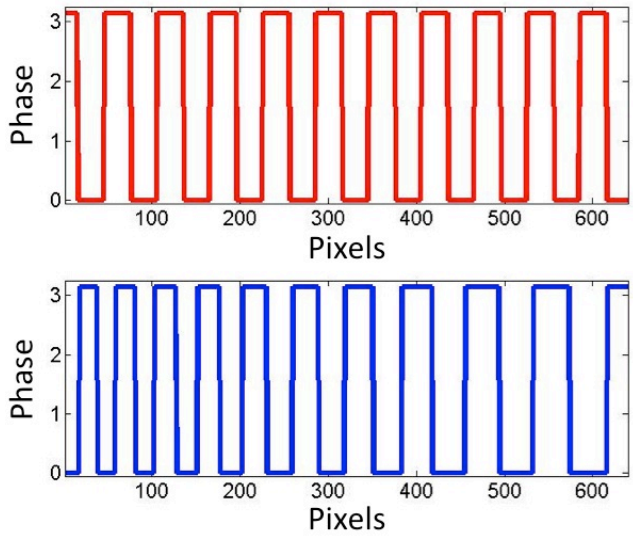

Figure 2.7 Phase mask conversion from the wavelength domain to the frequency domain. Top: A binary phase mask incorrectly displayed in the wavelength domain. Bottom: A binary phase mask correctly displayed in the frequency domain.

Greater detail into the SLM characterization and alignment are given in chapter 4 section 3 with respect to a home built pulse shaper.

2.4 Dispersion

The focus of this dissertation is on the integration of ultrafast spectroscopy with nonlinear microscopy. In order to drive nonlinear interactions, high peak intensities are required. Unfortunately, dispersion from microscope optics results in temporal broadening (figure 2.8). The increased pulse duration reduces peak intensities, resulting

in diminished capability to drive nonlinear transitions as well as limited temporal resolution. In this section we discuss the relationship between dispersion, spectral phase and pulse duration.

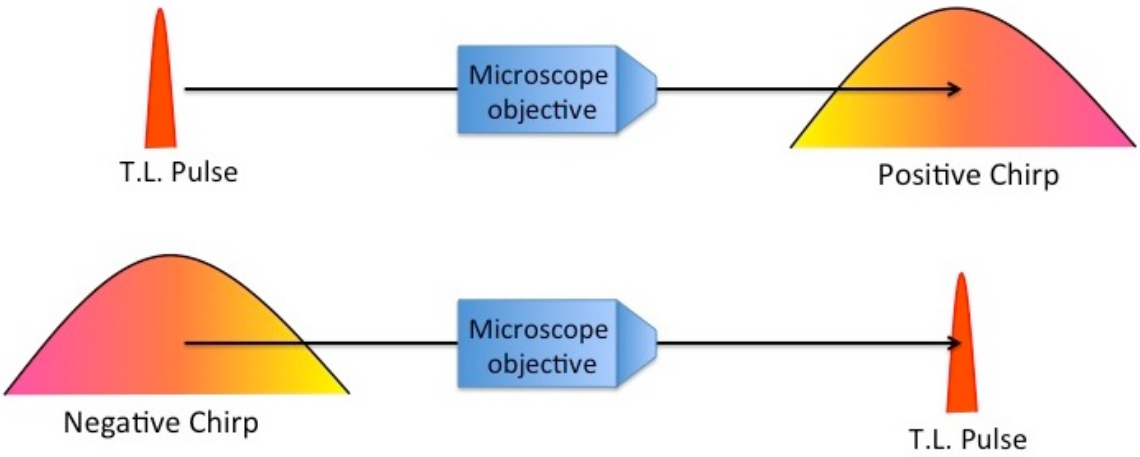

Figure 2.8 Cartoon of microscope objective dispersion broadening laser pulse and applying negative chirp to result in a transform-limited pulse at the sample.

A laser pulse can be described as an electric field both in the time domain and the frequency domain. The Fourier relation of the electric field in the frequency domain, $\tilde{E}(\omega)$, to the time domain, $E(t)$, is given by:

$$E(t) = \int_{-\infty}^{\infty} \tilde{E}(\omega)\exp(i\omega t)\,d\omega \tag{2.15}$$

where the electric field in the frequency domain is given as

$$\tilde{E}(\omega) = \left|\tilde{E}(\omega)\right|\exp\left[i\phi(\omega)\right] \tag{2.16}$$

In the frequency domain, the electric field may be broken down into an amplitude component $\tilde{E}(\omega)$, and a spectral phase component $\phi(\omega)$. When the spectral phase is expanded in a Taylor series as

$$\phi(\omega)=\phi(\omega_0)+\phi'(\omega_0)(\omega-\omega_0)+\frac{1}{2}\phi''(\omega_0)(\omega-\omega_0)^2+\frac{1}{6}\phi'''(\omega_0)(\omega-\omega_0)^3+\ldots \quad (2.17)$$

the individual terms can be associated with specific dispersive effects. The following details these associations:

$\phi(\omega_0)$ - The absolute phase corresponding to the phase between the carrier frequency and electric field envelope.

$\phi'(\omega_0)$ - Group delay (GD) corresponds to the pulse delayed in time

$\phi''(\omega_0)$ - Group delay dispersion (GDD or GVD) corresponds to the linear delay of individual frequencies resulting in the broadening of the pulse. This type of dispersion is also called chirp.

$\phi'''(\omega_0)$ - Third order dispersion (TOD) results in the edge frequencies trailing or proceeding the central frequency of the pulse.

Relating the spectral phase terms to the index of refraction gives insight into how material properties alter the laser pulse. The index of refraction is most commonly written as

$$n=\frac{c}{v_{phase}} \quad (2.18)$$

where c is the speed of light in a vacuum and v_{phase} is the phase velocity of light. The Sellmeier equation relates the wavelength to the index of refraction, by coefficients specific to known materials

$$n^2(\lambda)=1+\frac{B_1\lambda^2}{\lambda^2-C_1}+\frac{B_2\lambda^2}{\lambda^2-C_2}+\frac{B_3\lambda^2}{\lambda^2-C_3} \quad (2.19)$$

illustrating the nonlinear relationship between wavelength and its phase velocity. The constructive interference of multiple wavelengths as they propagate through a material leads to an envelope that propagates at the group velocity described by

$$v_g = v_{phase}\left[1 - \frac{k}{n}\frac{dn}{dk}\right]$$

where k is the wavenumber $\left(\nu = 2\pi c/\lambda\right)$ and n is the refractive index. From this relation we can see that the group velocity and the phase velocity travel at the same speed when the refractive index is independent of wavenumber (or wavelength). Since this is not the case for most materials, we see the physics of this relationship manifest itself in the form of group delay (GD), group delay dispersion (GDD) or group velocity dispersion (GVD), third order dispersion (TOD), and higher order terms. An example of the physical manifestation of GDD would be the broadening of the pulse envelope as the pulse propagates through a material. In this manner, the spectral phase can be easily visualized in terms of its relation to GDD

$$\phi'\left(\omega_0\right) = \frac{1}{v_g\left(\omega_0\right)} \tag{2.20}$$

as well as GVD

$$\phi''\left(\omega_0\right) = \frac{d}{d\omega}\left[\frac{1}{v_g\left(\omega_0\right)}\right] \tag{2.21}$$

with higher order terms following similar relationships.

When a pulse is TL, the spectral phase is constant and can be assumed to be zero, $\phi(\omega) = 0$, leading to constructive interference of every frequency, resulting in the

shortest pulse duration supported by the given bandwidth.[4] After transmission through various optics, the spectral phase is no longer constant, $\phi(\omega)=\phi_D(\omega)\neq 0$, where the new spectral phase due to dispersion is given by $\phi_D(\omega)$. Determining the spectral phase for each frequency, we can compensate for the dispersion by adding a compression phase term, $\phi_C(\omega)=-\phi_D(\omega)$, which will allow us to obtain a flat spectral phase

$$\phi(\omega)=\phi_D+\phi_C=0 \tag{2.22}$$

and a TL pulse at the sample (figure 2.8).

2.5 Pulse Characterization

The previous section discussed the affect of dispersion on ultrashort pulses. The ability to characterize a pulse enables one to compensate for dispersion as well as to generate pulses for selective excitation. While there are many pulse characterization techniques, all require interaction with a nonlinear material. Earlier, SHG was shown to be one measure of a pulse shape. Unfortunately, the SH spectrum does not tell us the spectral phase required for pulse compression. Instead, we must use techniques that retrieve the phase of the pulse. The most common of these techniques include Spectral Phase Interferometry for Direct Electric Field Reconstruction (SPIDER), Frequency Resolved Optical Gating (FROG) and its derivatives and Multi Photon Interference Phase Scan (MIIPS).[31-34] Of the aforementioned techniques, we use the MIIPS algorithm.

MIIPS is a successful technique for quickly determining the phase of a laser pulse.[19,35-37] Here we rewrite equation 2.8 in a manner to help discuss the MIIPS process.

$$E_2(\omega)=\left|\int\left|E(\omega+\Omega)\right|\left|E(\omega-\Omega)\right|\times\exp\left\{i\left[\varphi(\omega+\Omega)+\varphi(\omega-\Omega)\right]d\Omega\right\}\right|^2 \tag{2.23}$$

The SH field is shown to be dependent on the constructive interference of the phase from the independent fundamental fields. A phase of zero will result in maximizing the second harmonic intensity. By Taylor expansion of the spectral phase only nonzero even terms of the expansion can alter E_2.[37] A spectral phase is introduced, $f(\omega)$, to the unknown phase φ in order to cancel portions of the spectral phase. The algorithm chooses to maximize the second harmonic intensity when the output phase $\varphi(\omega)=\phi(\omega)+f(\omega)$ is minimized. To do this, the second derivative of the phase must equal zero, $\varphi''(\omega)=\phi''(\omega)+f''(\omega)=0$. The first iteration of the MIIPS process uses the reference function $f=\alpha\cos(\gamma\omega-\delta)$. Where the relationship

$$\phi''(\omega)=-f''(\omega)=\alpha\gamma^2\cos(\gamma\omega-\delta_{\max}(\omega)) \tag{2.24}$$

is used to retrieve the second derivative of the unknown spectral phase, $\phi(\omega)$. Once $\phi(\omega)$ is determined, the SLM applies the phase $-\phi(\omega)$ to cancel the dispersion. As the dispersion is typically very complex as can be seen in the higher order terms of the Taylor expansion, multiple iterations are required. Pulse compression is performed with the BioPhotonics Solutions Inc. MIIPS software. In our MIIPS traces, it takes on average 8 iterations until the resulting laser pulse is TL and generates the greatest second harmonic intensity (figure 2.9).

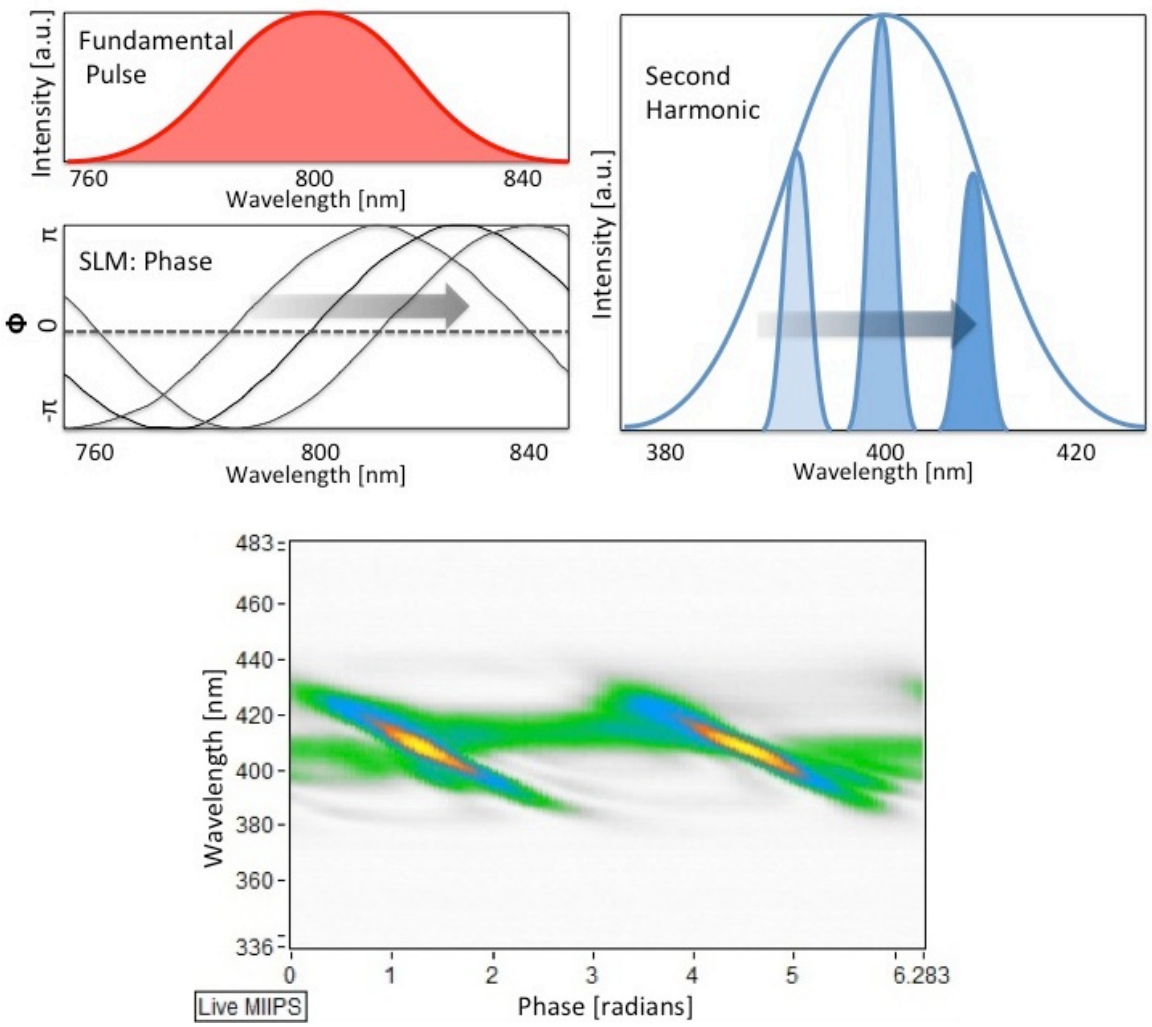

Figure 2.9 MIIPS Scan. Top: Cartoon illustrating the MIIPS technique. Bottom: Experimental MIIPS trace of a TL pulse.

Using the MIIPS process we have been able to compensate dispersion due to microscope objectives and other dispersive elements within the beam path. Even so, there is only so much dispersion that can be compensated for with this technique. This limitation is due to the finite number of pixels (640) and the index of refraction of the liquid crystals. The best approach is to limit the number of dispersive elements within the beam path. Collection optics must be transparent to the TL supported SH bandwidth to ensure sufficient collection efficiency. The MIIPS algorithm relies on feedback from

an Ocean Optics spectrometer and therefore requires strong coupling into the fiber. Achromatic lenses significantly improve coupling by reducing focal shifts, sphereochromatism, and other aberrations. Using the MIIPS technique, the resulting SH spectra is presented in figure 2.10.

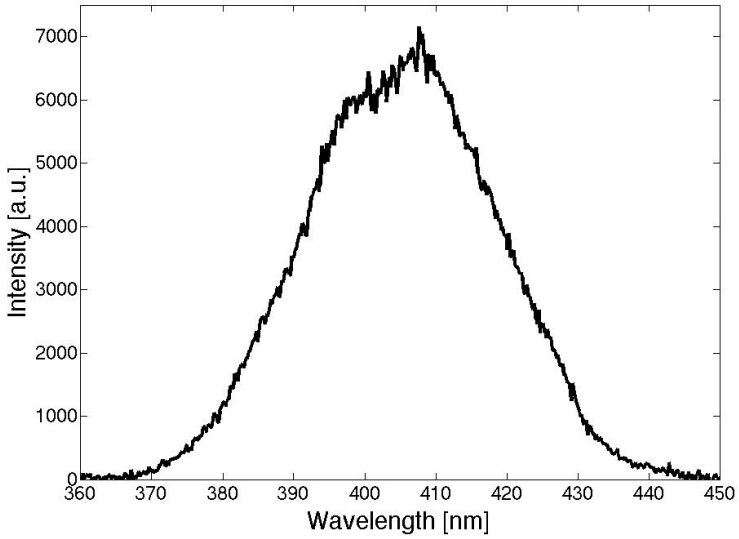

Figure 2.10 SH spectra after pulse compression using MIIPS algorithm.

2.6 Pulse Duration Measurement

On installation of the our oscillator, pulse characterization was done using the SPIDER technique.[38] A pulse duration of 6.9 fs was achieved after 4 bounces on DCM7 chirped mirrors and transmission through a CaF_2 wedge pair. Having a repetition rate of 82 MHz and mode-locked average power ranging from 570 to 630 mW the Venteon: One oscillator has capability of generating pulse energies >7 nJ and peak powers >1 MW. Focused down to small spot sizes, the high peak intensities can easily drive a multitude of nonlinear responses from materials of interest.

Intensity interferometric autocorrelation of the laser pulse was used to characterize the pulse durations after the microscope objective. A typical interferometric

autocorrelation measurement requires a beam splitter to create two separate beam paths that are later combined onto a nonlinear crystal after propagating different distances. The resulting second harmonic intensity, $I(\tau)$, recorded by the spectrometer as a function of pulse delay, τ, is

$$I(\tau) = \int_{-\infty}^{\infty} \left| \left(E(t) + E(t-\tau) \right)^2 \right| dt \tag{2.25}$$

Plotting the intensity at varying time delays creates an interference pattern that is used to characterize the pulse duration.

Instead of integrating a beamsplitter and delay stage into our experiment, we use the multiple independent comb shaping technique to perform an autocorrelation.[39] In this case, two pulses are generated from an original pulse by uploading a binary phase mask to the SLM. Applying a linear chirp to one of the pulses controls the time delay between the two pulses. Results from this technique before and after compensation are presented in figure 2.11.

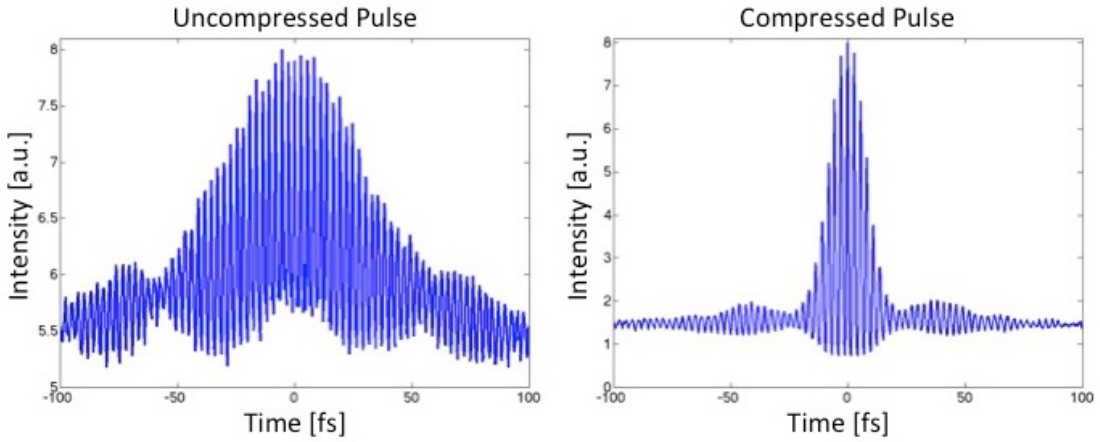

Figure 2.11 Autocorrelation measurement. Left: Autocorrelation before pulse compression. Right: Autocorrelation after pulse compression with MIIPS algorithm.

Relating the intensity autocorrelation to pulse duration requires *a priori* knowledge of the pulse shape. Here we assume a secant hyperbolic pulse shape, allowing us to relate the autocorrelation width, τ_{ac}, to the pulse during, τ, via a deconvolution factor 1.54

$$\tau = \tau_{ac}/1.54 \tag{2.26}$$

resulting in a pulse duration of approximately 11fs. Recall that our laser bandwidth supports a transform-limited pulse duration of approximately 7 fs. The discrepancy in these values is due to attenuation of the laser beam from microscope optics (microscope objective specifically) and attenuation of the resulting SH signal from the collection optics.

2.7 Selective TPEF

Pulse shaping can be used to populate the excited states of specific TPA molecules without populating spectrally similar TPA molecules.[12,35] In doing so, we can image individual fluorophores with minimal cross-talk associated with the other fluorophores emission. Using an SLM, the technique allows for the creation of high contrast images at biologically relevant time scales (ms).

Previously, we demonstrated that a compressed pulse results in a broadband SH spectrum, spanning 370-440 nm (figure 2.10). This bandwidth represents TPE spectra that may be used to excite TPA molecules. Using this pulse shape, we would be unable to distinguish between different fluorophores (having overlapping absorption and emission spectra) and the resulting image would have minimal contrast. Instead, we want to selectively excite fluorophores whose two-photon cross-sections reside in our excitation window without exciting other near lying fluorophores. To do this, we add a

destructive interference phase mask, φ_D, to our compression mask, φ_C, to obtain a selective excitation phase mask $\varphi_S = \varphi_C + \varphi_D$.[19] Assuming the compression phase mask results in a laser pulse with a flat spectral phase at the sample, $\varphi_C = 0$, we can write the selective excitation second harmonic as

$$E_2(\omega) = \left| \int \left| E(\omega + \Omega) \right| \left| E(\omega - \Omega) \right| \times \exp\left\{ i \left[\varphi_D(\omega + \Omega) + \varphi_D(\omega - \Omega) \right] d\Omega \right\} \right|^2 \tag{2.27}$$

where φ_D must now be determined.

2.7.1 Selective Excitation: Sinusoidal Phase Mask

Selective excitation may be accomplished by modulating the spectral phase with a sinusoidal function

$$\varphi_D = A \sin(k\omega - \delta) \tag{2.28}$$

By varying the amplitude, A, wavenumber, k, and phase, δ, terms for the sinusoid, a multitude of selective excitations may be created. The following illustrates the SHG dependence on the amplitude and frequency terms. Figure 2.12 shows the SHG selective excitation given sinusoidal phase masks with an amplitude ratio of 1:4:8:16.

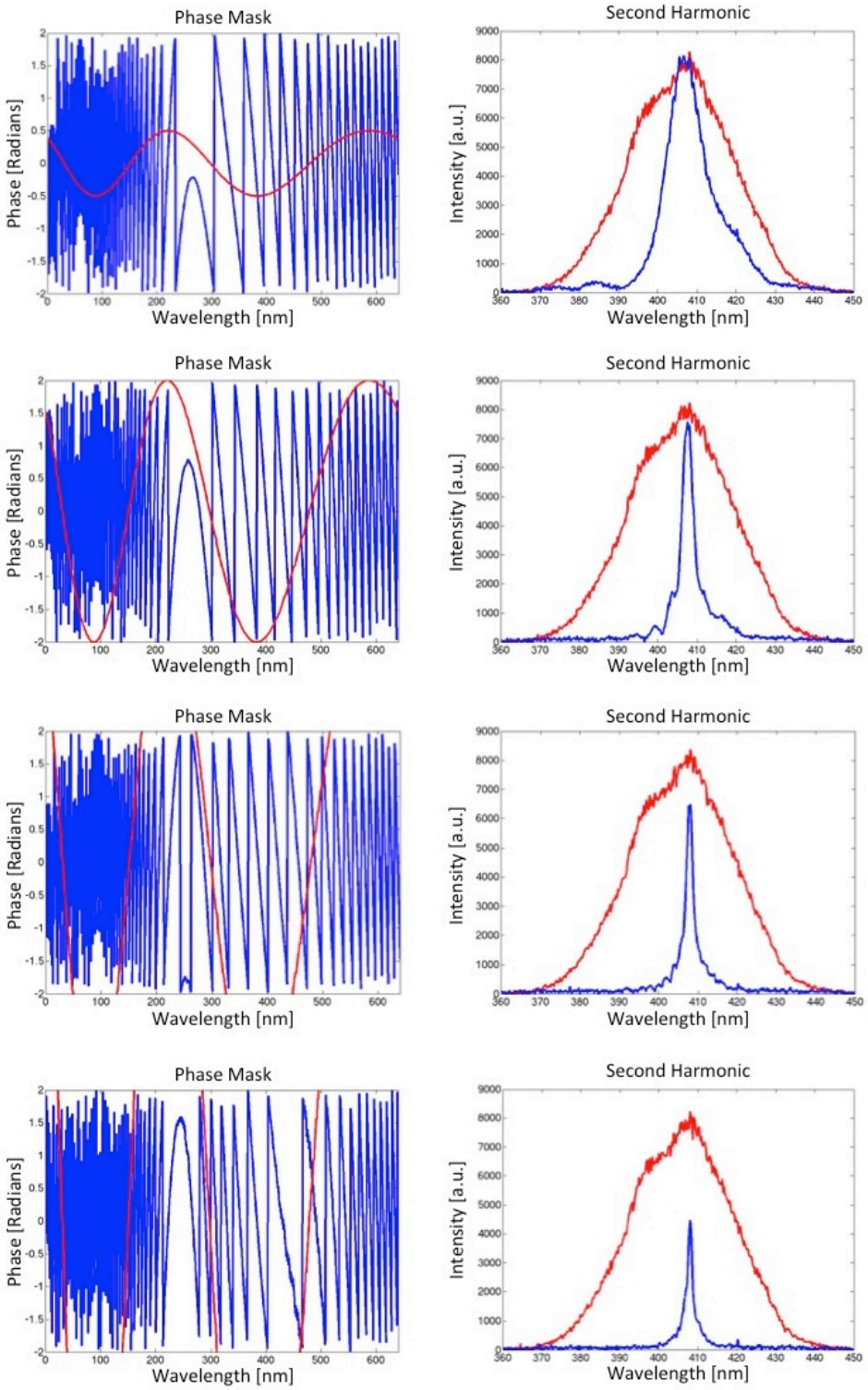

Figure 2.12 Selective excitation using sinusoidal phase modulation with varying amplitude of 1:4:8:16.

The increase in amplitude initially narrows the selective excitation to approximately 5nm FWHM. Further increasing the amplitude decreases the SH intensity. The frequency of the phase term used resulted in only one selective excitation, which is not always the case.

Frequency modulation of the sinusoidal phase mask resulted in multiple selective excitations. Here a frequency ratio of 5:10:20 were used to illustrate the SHG dependence (figure 2.13).

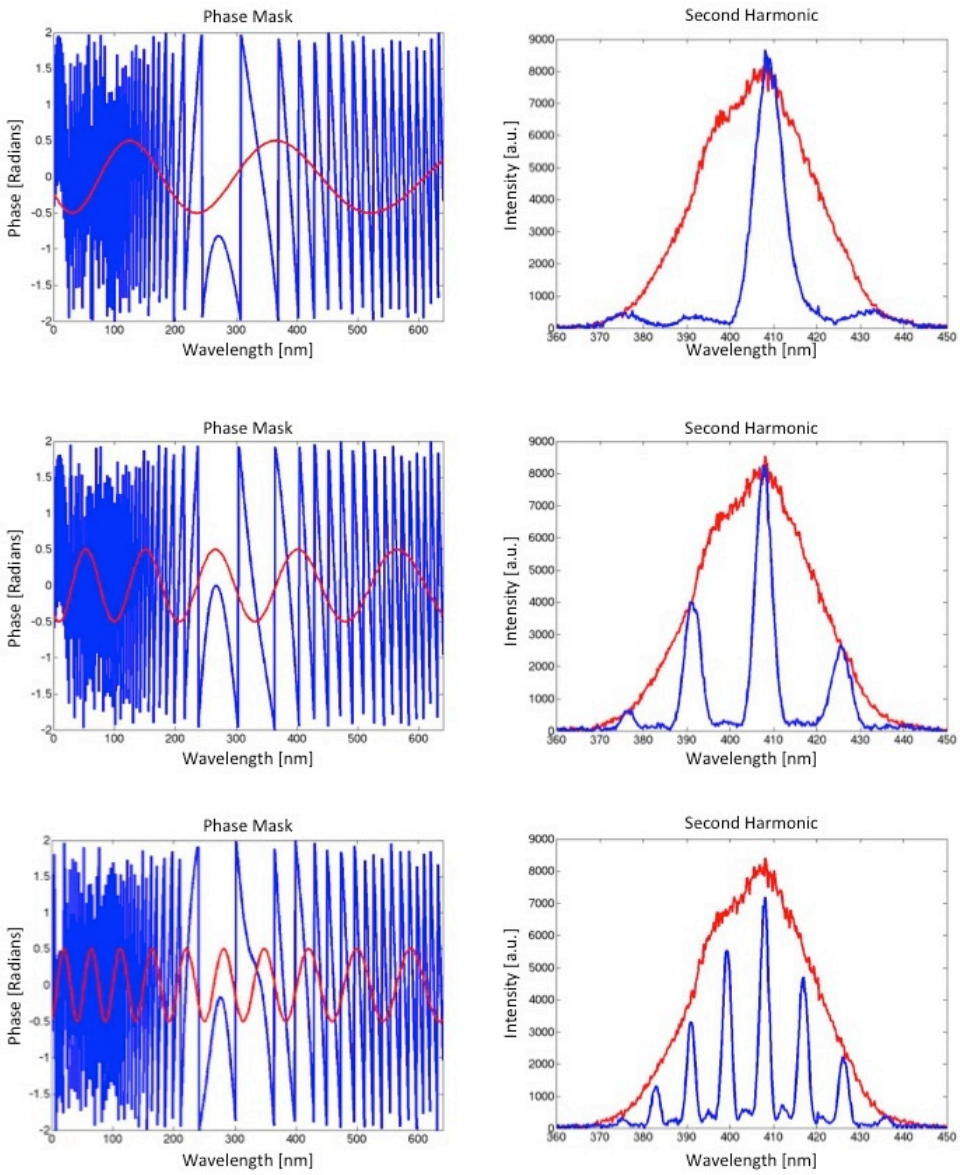

Figure 2.13 Selective excitation using sinusoidal phase modulation with varying frequency of 5:10:20.

Further increasing the frequency to the limit of a single cycle equaling 2 pixels on the SLM results in SHG approaching complete destructive interference. The multiple selective excitations within one pulse could possibly be used to excite multiple fluorophores in one pulse without the excitation of others.

The combinations of sinusoidal phase masks may result in the generation of arbitrary waveforms for selective excitations. The complexity involved in designing a selective excitation from such a combination is compounded by the number of pixels of the SLM as well as their discrete number of states. A more direct approach for determining selective excitation phase masks has been found in the form of binary selective excitation.

2.7.2 Binary Selective Excitation

Dantus and coworkers demonstrated selective two-photon excitation using a binary phase mask.[40] The technique uses symmetry arguments for arranging the 0 and π values within the phase array to optimize the destructive and constructive interference. Specifically, the SH intensity is maximized at a chosen frequency using a phase mask with a change in symmetry or no change in symmetry. Destructive interference across all frequencies and thereby a decrease in the SH elsewhere, requires a phase mask that is asymmetric both locally and globally.

A basic binary phase mask for generating selective excitations at the limits of our SH bandwidth resulted in limited success (figure 2.14). The selective excitation phase mask was generated by combining a square wave pulse train, ranging from 0 to π, with a zero phase array. Unfortunately, only broad selective excitations can be created using this technique.

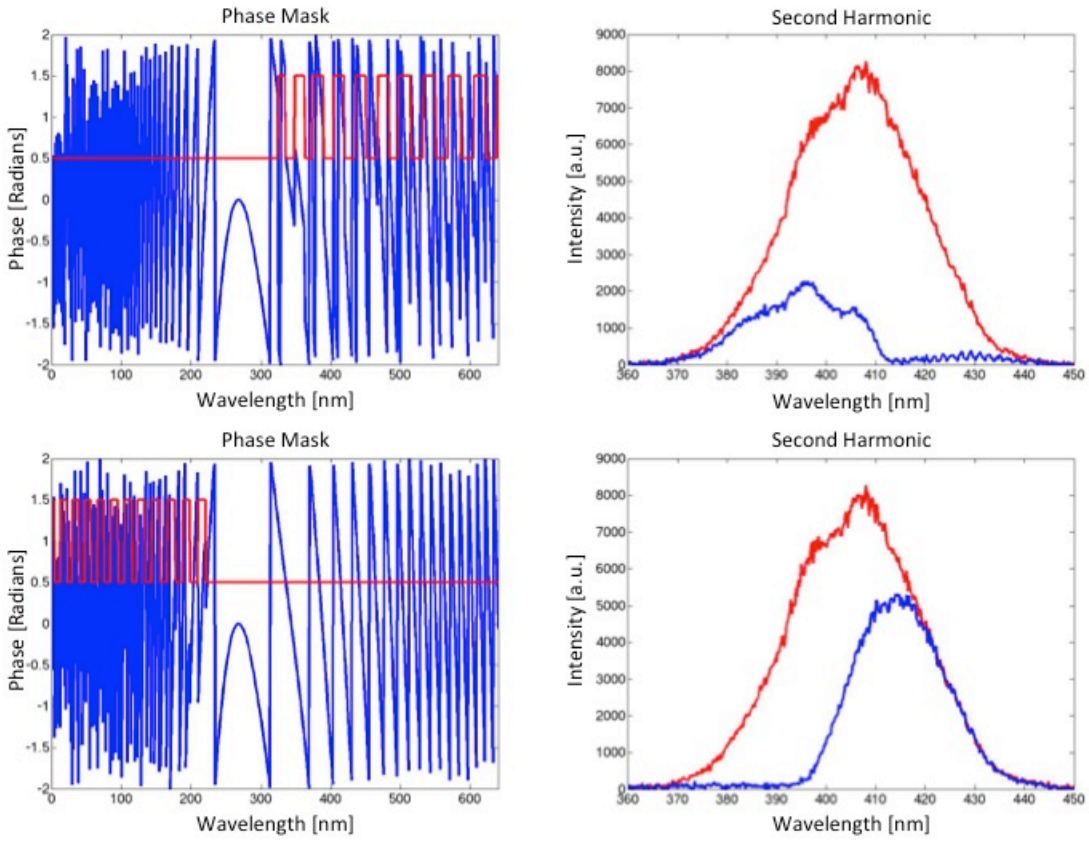

Figure 2.14 Binary selective excitation using a modified Heaviside step function.

The failure to obtain narrow selective excitations is due to the local symmetries in the phase masks resulting in constructive interference.

Our goal is to generate a narrow second harmonic peak at a chosen frequency and no SH intensity at other frequencies. To accomplish this feat, a majority of the phase array should be asymmetric so that frequencies may destructively interfere. This can be accomplished using prime numbers as a shifting register between 0 and π within the linear array.[20] Phase masks built using this algorithm varied in success, with different phase masks having a combination of improvements and deficiencies with respect to the others. For example, some selective excitations would have high intensity peaks, but would also have a high level of background intensity. Other masks had the opposite

features, having low selective excitation intensity accompanied with low background. Combining the best attributes and discarding unwanted traits is assumed to be the best approach for generating an ideal selective excitation phase mask. Similar to the Fourier synthesis technique though, the solution is nontrivial.

2.7.3 Genetic Algorithm Pulse Shape Optimization

The difficulty of determining the ideal spectral phase mask for selective excitation may be greatly reduced by employing nonlinear global optimization algorithms. Treating each of the 640 pixels of the SLM as unknown variables, a binary genetic algorithm was used to optimize selective excitations. Figure 2.15 illustrates the genetic algorithm optimization process in terms of determining the breed of dog with the quietest bark.[41] First, arrays containing randomly distributed zeros and ones are applied to the function of interest. The resulting values are ranked and the top corresponding arrays are chosen for the mating process. The mating process mixes the values in the arrays creating offspring arrays. The offspring arrays replace the initial poor performing arrays, which are then subjected to mutations, in the form of changes in some of the array values. The new arrays are then fed back into the test function and the processes is iterated until the algorithm converges, ideally, to the global minimum. We used a genetic algorithm created by MATLAB (2013b, The MathWorks, Natick, MA) within the global optimization toolbox.

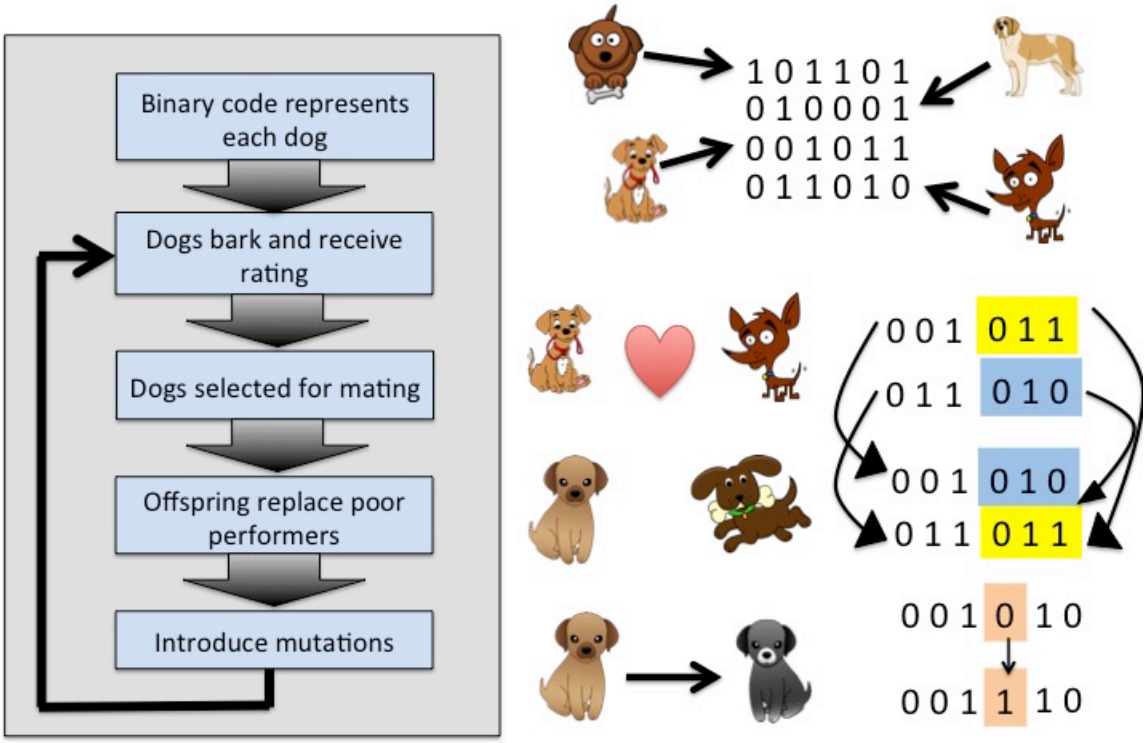

Figure 2.15 Binary genetic algorithm cartoon adapted to illustrate minimization of a dog's bark.[41]

Various optimization techniques have been applied to pulse shaping. [42,43] [44,45] Both experimental feedback loops and computational models integrated with global optimization algorithms have been shown to have benefits and limitations. The experimental feedback technique allows for the optimization of a pulse shape without requiring the in depth knowledge of the complex optics required for a computational model. The SLM simply applies a spectral phase to the laser pulse frequencies, which is then focused onto a BBO, generating the corresponding SH. The SH is detected by a spectrometer and then compared to the ideal spectrum. A fitness value is generated and the process is repeated according to an optimization algorithm until a phase mask results in the ideal SH spectrum (figure 2.16).

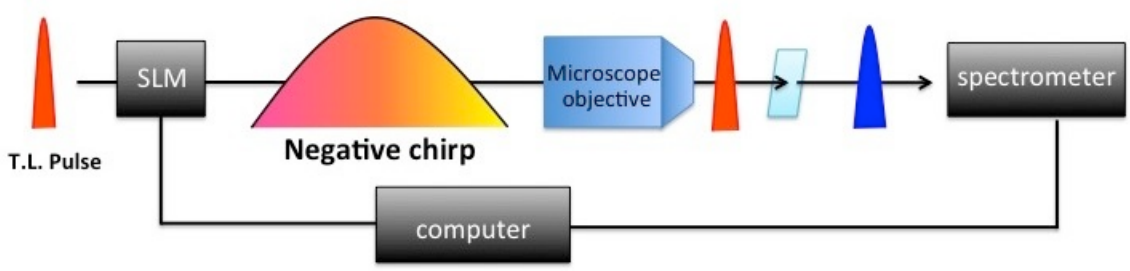

Figure 2.16 Experimental feedback loop integrated with a genetic algorithm.

Unfortunately, this technique requires significant time to converge to the chosen pulse shape. In our studies, it took approximately 3 hours to converge to the ideal phase mask for a chosen selective excitation. This was primarily due to slow communication between equipment, although experimental noise also contributed. Even with these limitations, the system was able to converge to a solution in many instances (figure 2.17).

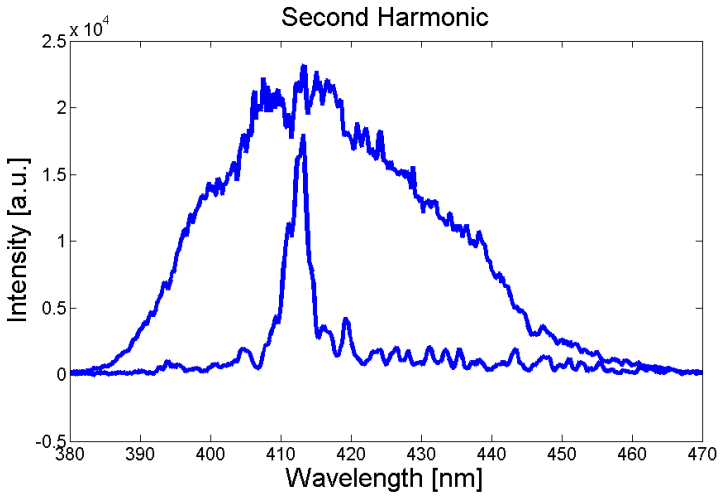

Figure 2.17 Ideal selective excitation obtained from experimental genetic algorithm.

Another limitation to this technique is the lack of knowledge gained about the system. When the selective excitation failed to converge to a chosen threshold, no model was present to give insight into mechanism for the failure. For these reasons, a computational model was found to be a better approach.

Iteration of the genetic algorithm over a computational model resulted in the convergence to an ideal selective excitation phase mask in minutes. The model assumes an originally flat phase and then adds a destructive interference phase mask to obtain an ideal selective excitation. If the actual phase is not flat, the selective excitation will diverge from the model. It is important to have the amplitude of the Venteon spectrum corrected for optic attenuation. This is especially the case for the microscope objective, where the transmission drops off significantly after 920 nm (figure 2.18).

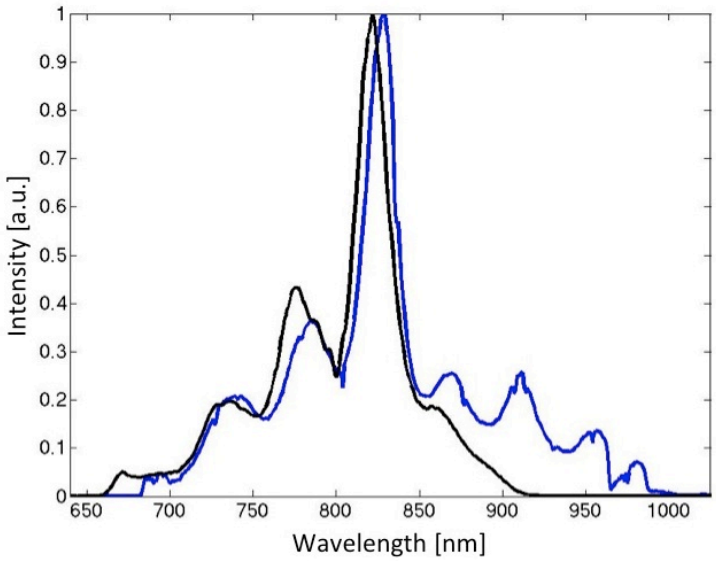

Figure 2.18 Fundamental spectrum with and without attenuation from microscope objective. The blue spectrum is without attenuation and the black spectra is after microscope objective attenuation.

The resulting theoretical model for the optimized phase mask is shown in figure 2.19 (left). The corresponding experimental selective excitation using the optimized phase mask found using the theoretical genetic algorithm is shown in figure 2.19 (right). Both the theoretical model and experimental result are very similar, particularly in terms of their selective excitation spectra. A noticeable difference between the model and experimental result is in the TL-SH spectra. Here we can see that the model expects the TL-SH to span out to approximately 340nm, whereas experimentally the TL-SH

bandwidth is limited to 360nm. This difference is due to attenuation from the collection optics. The microscope condenser in specific has minimal transmission below 360 nm.

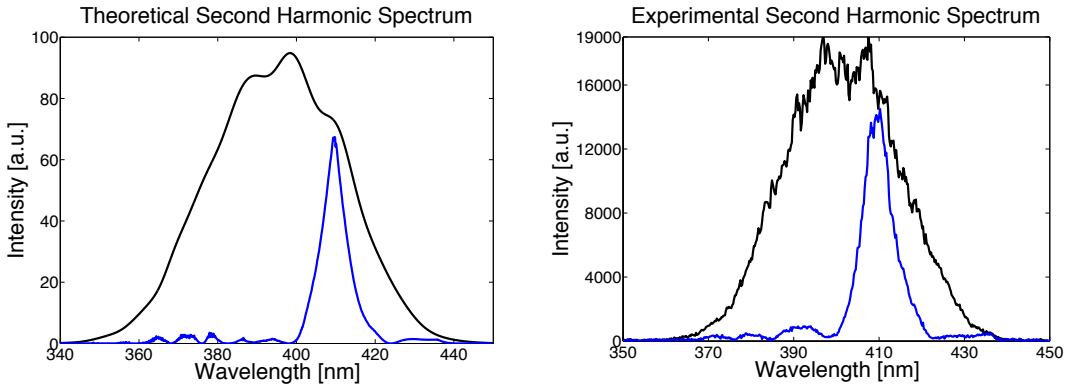

Figure 2.19 Left: Theoretical model of selective excitation from optimized phase mask. Right: Experimental selective excitation spectrum using optimized phase mask produced from theoretical model.

The additional value of generating optimized phase mask computationally is the ability to add additional constraints to the system. For example, the selective excitation of a single TPA chromophore in the presence of multiple overlapping TPA cross-sections within the TL-SH bandwidth can easily be included in the model.

2.8 Conclusions

We have demonstrated techniques for compensating dispersion and generating selective excitations within a TL-SH bandwidth. SHG is an ideal system in that it has no resonances within our bandwidth. The response of complex molecular systems to these pulse shapes is not always equivalent. First, there may be one-photon resonances within the fundamental bandwidth. If this is the case, a transition via the one-photon resonance will occur due to the stronger oscillator strength. Furthermore, SHG is a three-wave mixing process requiring a second order polarization of the medium. The crystal structure and symmetry of a BBO crystal is designed to have to have large second-order

polarization to generate SH and does not have excited states in the visible (only virtual states). This is not the case for molecules, which may have drastically different symmetries. For example, the final state from a TPA transition is real (can be populated), and the relationship between the pulse duration and the excited state lifetime can result in different responses. In the next chapter, we will apply pulse shaping to selectively excite GFP variants. These fluorophores have been designed to have large two-photon cross-sections and as well as long lived excited states (nanoseconds). These designer probes enabling us to apply our pulse shaping techniques for selective TPE FRET stoichiometry.

References:

[1] Maiman, T.H., "Stimulated optical radiation in ruby," Nature 187, 493–494 (1960).

[2] DeMaria, A.J., Ferrar, C.M., and Danielson, G.E., "MODE LOCKING OF A Nd3+-DOPED GLASS LASER," Applied Physics Letters (1966).

[3] Brumer, P., and Shapiro, M., "Coherence Chemistry: Controlling Chemical Reactions with Lasers," Accounts of Chemical Research 22(12), 407–413 (2001).

[4] Weiner, A., [Ultrafast Optics], Wiley (2011).

[5] Rulliere, C., [Femtosecond laser pulses: principles and experiments], Springer (2004).

[6] Bucksbaum, P.H., "Photonics: An atomic dimmer switch : Article : Nature," Nature 396(6708), 217–219 (1998).

[7] Brumer, P., and Shapiro, M., "ONE PHOTON MODE SELECTIVE CONTROL OF REACTIONS BY RAPID OR SHAPED LASER-PULSES - AN EMPEROR WITHOUT CLOTHES," Chemical Physics 139(1), 221–228 (2001).

[8] Gordon, R.J., and Rice, S.A., "ACTIVE CONTROL OF THE DYNAMICS OF ATOMS AND MOLECULES," Annual review of physical chemistry 48(1), 601–641 (1997).

[9] Dupont, E., Corkum, P., Liu, H., Buchanan, M., and Wasilewski, Z., "Phase-Controlled Currents in Semiconductors," Physical Review Letters 74(18), 3596–3599 (1995).

[10] Yin, Y.-Y., Elliott, D.S., Shehadeh, R., and Grant, E.R., "Two-pathway coherent control of photoelectron angular distributions in molecular NO," Chemical Physics Letters 241(5-6), 591–596 (1995).

[11] Ohmori, K., "Wave-packet and coherent control dynamics," Annual review of physical chemistry (2009).

[12] Ogilvie, J.P., Debarre, D., Solinas, X., Martin, J.L., Beaurepaire, E., and Joffre, M., "Use of coherent control for selective two-photon fluorescence microscopy in live organisms," Optics Express 14(2), 759–766 (2006).

[13] Nuernberger, P., Vogt, G., Brixner, T., and Gerber, G., "Femtosecond quantum control of molecular dynamics in the condensed phase," Physical Chemistry Chemical Physics 9(20), 2470 (2007).

[14] Silberberg, Y., "Quantum Coherent Control for Nonlinear Spectroscopy and Microscopy," Annual review of physical chemistry 60(1), 277–292 (2009).

[15] Meshulach, D., and Silberberg, Y., "Coherent quantum control of multiphoton transitions by shaped ultrashort optical pulses," Physical Review A 60(2), 1287 (1999).

[16] Dudovich, N., Dayan, B., Gallagher Faeder, S., and Silberberg, Y., "Transform-Limited Pulses Are Not Optimal for Resonant Multiphoton Transitions," Physical Review Letters 86(1), 47–50 (2001).

[17] Meshulach, D., and Silberberg, Y., “Coherent quantum control of two-photon transitions by a femtosecond laser pulse,” Nature1–4 (1998).
[18] Boyd, R.W., [Nonlinear Optics, Third Edition], 3rd ed., Academic Press (2008).
[19] Walowicz, K.A., Pastirk, I., Lozovoy, V.V., and Dantus, M., “Multiphoton intrapulse interference. 1. Control of multiphoton processes in condensed phases,” Journal of Physical Chemistry A 106(41), 9369–9373 (2002).
[20] Lozovoy, V.V., and Dantus, M., “Systematic Control of Nonlinear Optical Processes Using Optimally Shaped Femtosecond Pulses,” ChemPhysChem 6(10), 1970–2000 (2005).
[21] Bardeen, C.J., Yakovlev, V.V., Squier, J.A., and Wilson, K.R., “Quantum control of population transfer in green fluorescent protein by using chirped femtosecond pulses” 120(50), 13023–13027 (1998).
[22] Hacker, M., Netz, R., Roth, M., Stobrawa, G., Feurer, T., and Sauerbrey, R., “Frequency doubling of phase-modulated, ultrashort laser pulses,” Applied Physics B 73(3), 273–277 (2001).
[23] Monmayrant, A., Weber, S., and Chatel, B., “A newcomer's guide to ultrashort pulse shaping and characterization,” Journal of Physics B: Atomic, Molecular and Optical Physics 43(10), 103001 (2010).
[24] Weiner, A.M., Heritage, J.P., and Kirschner, E.M., “High-resolution femtosecond pulse shaping,” JOSA B (1988).
[25] Weiner, A.M., [Ultrafast Optics], Ultrafast optics, 1–595 (2009).
[26] Weiner, A.M., “Femtosecond pulse shaping using spatial light modulators,” Review of Scientific Instruments 71, 1929–1960.
[27] Xu, B., Coello, Y., Lozovoy, V.V., Harris, D.A., and Dantus, M., “Pulse shaping of octave spanning femtosecond laser pulses,” Optics Express (2006).
[28] PerkinElmer, Inc., “SLM-128 and SLM-640,” PerkinElmer, 1–4 (2013).
[29] “SLM Spatial Light Modulator,” 1–45 (2006).
[30] Palmer, C.A., [Diffraction Grating Handbook], Richardson Grating Laboratory, 7th Edition (2000).
[31] Horstmeyer, R., “Reconstructing Ultrashort Pulses: Frequency Resolved Optical Gating and Phase Space Functions”1–18 (2010).
[32] Trebino, R., [Frequency-Resolved Optical Gating], Springer (2000).
[33] Iaconis, C., and Walmsley, I.A., “Self-Referencing Spectral Interferometry forMeasuring Ultrashort Optical Pulses,” IEEE JOURNAL OF QUANTUM ELECTRONIC 35(4), 501–509 (1999).
[34] Pastirk, I., Cruz, J., Walowicz, K.A., and Lozovoy, V.V., “Selective two-photon microscopy with shaped femtosecond pulses,” Opt … (2003).
[35] Lozovoy, V.V., Pastirk, I., Walowicz, K.A., and Dantus, M., “Multiphoton intrapulse interference. II. Control of two- and three-photon laser induced fluorescence with shaped pulses,” Journal of Chemical Physics 118(7), 3187–3196 (2003).
[36] Cruz, Dela, J.M., Pastirk, I., Lozovoy, V.V., Walowicz, K.A., and Dantus, M., “Multiphoton intrapulse interference 3: Probing microscopic chemical environments,” Journal of Physical Chemistry A 108(1), 53–58 (2004).
[37] Lozovoy, V.V., Pastirk, I., and Dantus, M., “Multiphoton intrapulse interference. IV. Ultrashort laser pulse spectral phase characterization and compensation,”

Optics Letters 29(7), 775–777 (2004).
[38] Iaconis, C., and Walmsley, I.A., "Spectral phase interferometry for direct electric-field reconstruction of ultrashort optical pulses," Optics Letters (1998).
[39] Pestov, D., Lozovoy, V.V., and Dantus, M., "Multiple Independent Comb Shaping (MICS): phase-only generation of optical pulse sequences," Optics Express (2009).
[40] Comstock, M., Lozovoy, V.V., Pastirk, I., and Dantus, M., "Multiphoton intrapulse interference 6; binary phase shaping," Multiple values selected 12(6), 1061 (2004).
[41] Haupt, R.L., and Haupt, S.E., [Practical Genetic Algorithms], Wiley, Newark, NJ (2004).
[42] Bardeen, C.J., Yakovlev, V.V., Wilson, K.R., Carpenter, S.D., Weber, P.M., and Warren, W.S., "Feedback quantum control of molecular electronic population transfer," Chemical Physics Letters 280(1-2), 151–158 (1997).
[43] Judson, R., and Rabitz, H., "Teaching lasers to control molecules," Physical Review Letters 68(10), 1500–1503 (1992).
[44] Assion, A., Baumert, T., Bergt, M., Brixner, T., and Kiefer, B., "Control of chemical reactions by feedback-optimized phase-shaped femtosecond laser pulses," Science (1998).
[45] Baumert, T., Brixner, T., Seyfried, V., Strehle, M., and Gerber, G., "Femtosecond pulse shaping by an evolutionary algorithm with feedback," Applied Physics B 65, 779–782 (1997).

Chapter 3 Pulse-Shaping-Based Two-Photon FRET Stoichiometry

3.1 Introduction

Förster Resonance Energy Transfer (FRET) based microscopy is a technique that provides information on molecular interactions within biological systems.[1] Often referred to as the "spectroscopic ruler", the energy transfer dependence is proportional to $1/r^6$, where 'r' is the intermolecular distance, which results in energy transfer only when the donor and acceptor molecules are within close proximity (1-10nm).[2] This technique has given insight into a wide range of molecular interactions within living cells.[1,3] Until recently, FRET has been measured in arbitrary units, inhibiting stoichiometric inference of the system of interest.[4,5] A "three-cube FRET" technique for quantifying Ca^{2+} channel subunit interaction with channel-calmodulin has been demonstrated but had conflicting *in vitro* results.[6] Hoppe *et al*. extended the work by demonstrating one-photon FRET stoichiometry in live cells where the fraction of donor and acceptor in complex as well as the ratio of total donor and acceptor molecules present were quantified for CFP- and citrine-labeled molecules in living cells.[7] Later, Raicu *et al.* used spectrally-resolved one-photon FRET to quantify the protein interaction in living yeast cells.[8]

Here we extend FRET stoichiometry approaches to two-photon FRET. Two-photon FRET techniques have been previously used for a myriad of applications such as

generating brighter images using an efficient absorber as donor to transfer excitation to an efficient emitter,[9] studying intra-cellular biochemistry,[10,11] developing efficient deep-tissue photodynamic therapy,[12,13] inducing release of caged glutamate for neuroscience experiments[14] and real-time monitoring of drug release by measuring FRET between a PEGylated carbon quantum-dot (drug carrier and donor) and the drug DOX (acceptor).[15] Merging the positive attributes of two-photon excitation with FRET stoichiometry could extend the applicability of FRET stoichiometry to a greater number of biological systems. Multi-photon FRET stoichiometry was first demonstrated by extending the spectrally-resolved FRET technique to two-photon excitation for the study of protein complex superstructure and distribution[16] and protein-protein interactions.[17] This measurement requires fluorescence spectra to be recorded per pixel throughout the experiment; the image acquisition results in 2-D images of wavelength vs. x-dimension and y-dimension and could last several minutes. Tunable Ti:Sapphire lasers are time consuming to tune to different selective excitations, thus limiting the potential applications to the study of relatively slow dynamics in real biological systems. We use a broadband Ti:sapphire oscillator generating a bandwidth of 650-1000 nm, which allows simultaneous excitation of multiple fluorophores having two-photon cross-sections within the excitation bandwidth. Focusing the 6-femtosecond pulse at the sample plane results in high peak intensities that can drive multiphoton processes without the high average power often associated with phototoxicity in cells (damage).[18] Microscope objectives comprising multiple optical elements, necessary for achieving a diffraction-limited spot size, produce significant temporal dispersion resulting in a decrease in peak intensity. Using pulse compression to compensate for microscope dispersion, we can achieve pulse durations

approaching ~12 fs (FWHM), which can efficiently drive nonlinear transitions in GFP-type probes.

Pulse shaping has been demonstrated to suppress autofluorescence in live cells.[19,20] Using a similar technique, we rapidly switch between pulse shapes to excite specific fluorophores within our bandwidth on the millisecond time scale.[21-23] The significant decrease in time required to excite specific fluorophores enables rapid image acquisition. Multiple fluorophores required for FRET stoichiometry results in spectral congestion in the absorption and emission profiles. The combination of phase shaping and spectral filtering to select non-overlapping emission enhances contrast (decreases cross-talk) and results in better discrimination.

In this manuscript we develop a generalized stoichiometry theory to account for cross-talk associated with two-photon microscopy. We apply the technique to live COS-7 cells, where the direct quantification of donor and acceptor molecules in complex as well as the molar ratio of acceptor to donor *in vitro* is demonstrated, and show that this technique can be used to quantify cellular dynamics on biologically relevant time scales. Our stoichiometric function is parameterized from images taken of cells expressing only donor, acceptor or donor-acceptor construct (guaranteed FRET) using two pulse shapes optimized for excitation of either the donor or acceptor. The state diagram in figure 3.1 illustrates the signaling pathways as well as the corresponding molecular interaction for the cases of donor and acceptor in and out of construct. The parameters are proportionality constants represented by the symbols: $\alpha,\beta,\theta,\eta,\gamma,\xi$. A description of each variable can be found in table 3.1 with the corresponding mathematical description found in the derivation section.

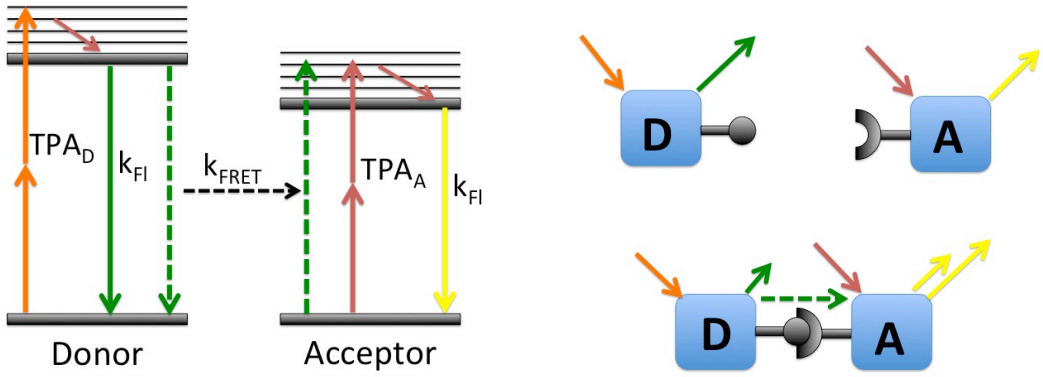

Figure 3.1 Two-photon FRET stoichiometry description. The donor (mAmeterine) and acceptor (tdTomato) are selectively excited with the emission split with a dichroic and detected with two PMTs. When the donor and acceptor are not in construct, no FRET occurs, and a majority of the emission from the donor is collected in the donor channel and a majority of the acceptor emission is collected in the acceptor channel. In construct, FRET occurs between the donor and acceptor resulting in increased emission from the acceptor with the donor pulse shape and decreased emission from the donor.

The images collected are labeled I_A, I_D, and I_F corresponding to the image at acceptor excitation and emission wavelengths, an image at donor excitation and emission wavelengths, and an image of donor excitation and acceptor emission wavelengths respectfully. The results stoichiometric equation describing the fraction of acceptor in complex, f_A, the fraction of donor in complex, f_D, and the molar ratio of acceptor to donor, R, is shown in equation 3.1.

$$f_A = \gamma_{TPE}\left[\frac{\frac{\eta}{\eta-\beta}I_F - \frac{\beta\eta}{\eta-\beta}I_D}{\frac{\theta\alpha}{\theta-\alpha}I_A - \frac{\theta\alpha}{\theta-\alpha}I_F} - 1\right]\frac{1}{E}$$

$$f_D = \left[1 - \frac{\left(\frac{1}{\eta-\beta}\right)\left(\eta I_D - I_F\right)}{\xi\left(\left(\frac{\eta\theta-\beta\alpha}{(\theta-\alpha)(\eta-\beta)}\right)I_F - \left(\frac{\beta\eta}{\eta-\beta}\right)I_D - \left(\frac{\alpha\theta}{\theta-\alpha}\right)I_A\right) + \left(\frac{1}{\eta-\beta}\right)\left(\eta I_D - I_F\right)}\right]\frac{1}{E} \qquad (3.1)$$

$$R = \frac{f_D}{f_A} = \frac{[A_T]}{[D_T]}$$

Table 3.1 Glossary of symbols for FRET stoichiometry.

Symbols	Description
I_A	Intensity or image at the acceptor excitation and acceptor emission.
I_D	Intensity or image at the donor excitation and donor emission.
I_F	Intensity or image at the donor excitation and acceptor emission.
E	Efficiency calculated from FLIM measurements
R	The molar ratio of acceptor to donor measured by FRET stoichiometry.
f_A	Fraction of acceptor in complex as measured by FRET stoichiometry.
f_D	Fraction of donor in complex as measured by FRET stoichiometry.
α	Proportionality constant relating acceptor fluorescence at the acceptor excitation to the donor excitation.
β	Proportionality constant relating donor fluorescence detected at the acceptor emission relative to that detected at the donor emission.
θ	Proportionality constant relating donor fluorescence at the acceptor excitation to the donor excitation.
η	Proportionality constant relating acceptor fluorescence detected at the acceptor emission relative to that detected at the donor emission.
γ	Ratio of the extinction coefficient of the acceptor to the donor at the donor excitation.
ζ	Proportionality constant relating the sensitized acceptor emission to the decrease in donor fluorescence due to FRET.

3.2 Materials and Methods

3.2.1 COS-7 Cell Culture and Transfection

COS-7 cells were grown in Dulbecco's Modified Eagle Medium (Ref: 11885-084, supplemented with 10% fetal bovine serum and 1% penicillin/streptomycin mixture) at $37^{\circ}C$ in 5% CO_2. COS-7 cells were plated on 35-mm tissue culture dishes 24 hours prior to transfection. Three different plasmid DNAs were used for transfection, mAmetrine, tdTomato, and an mAmetrine-tdTomato linked construct. The operating frame of mAmetrine was inserted in frame into ptdTomato-N1 vector (Clontech) by an amino acid polypeptide linker (ASGAPVAT) between the NheI and AgeI sites to create the mAmetrine-tdTomato linked construct. Transfections were performed when cells were 50% confluent, where $0.5\mu g$ of plasmid DNA was combined with $100\mu L$ of serum-free media and $3\mu L$ of FuGene. The following construct combinations were used to transfect different plates: mAmetrine, tdTomato, mAmetrine + tdTomato, mAmetrine-tdTomato, mAmetrine-tdTomato + tdTomato , mAmetrine-tdTomato + mAmetrine plasmids ('-' denotes the amino acid linker, whereas '+' denotes a mixture). 24 hours after transfection, cells were imaged in Ringer's Buffer while being maintained at $37^{\circ}C$ using a heated stage during data collection.

3.2.2 Imaging

The microscope setup used in this experiment is shown in figure 2. Pulses from an 82 MHz Ti:sapphire oscillator (Venteon: Pulse one), with >300 nm bandwidth centered at ~800 nm, were phase-shaped by a MIIPS® 640 Box (BioPhotonic Solutions Inc.) equipped with a 640-pixel SLM (PerkinElmer) in a folded 4-f geometry. The phase-

shaped beam is sent into the scan head of a Prairie Technologies modified Olympus BX51WI upright microscope for imaging. A water-immersion microscope objective (Olympus UPlanApo 60X, 1.2NA) was used to focus onto the sample and collect epi-fluorescence signal. The excitation power at the sample was approximately 2 mW. The emitted signal was separated from the excitation light with a dichroic mirror (Chroma 660DCXXR), filtered with a low-pass filer (Chroma E650SP), and spectrally split into two PMT channels (λ_D^{em} and λ_A^{em}) using a dichroic (Chroma 550DCXR) allowing for multicolor detection.

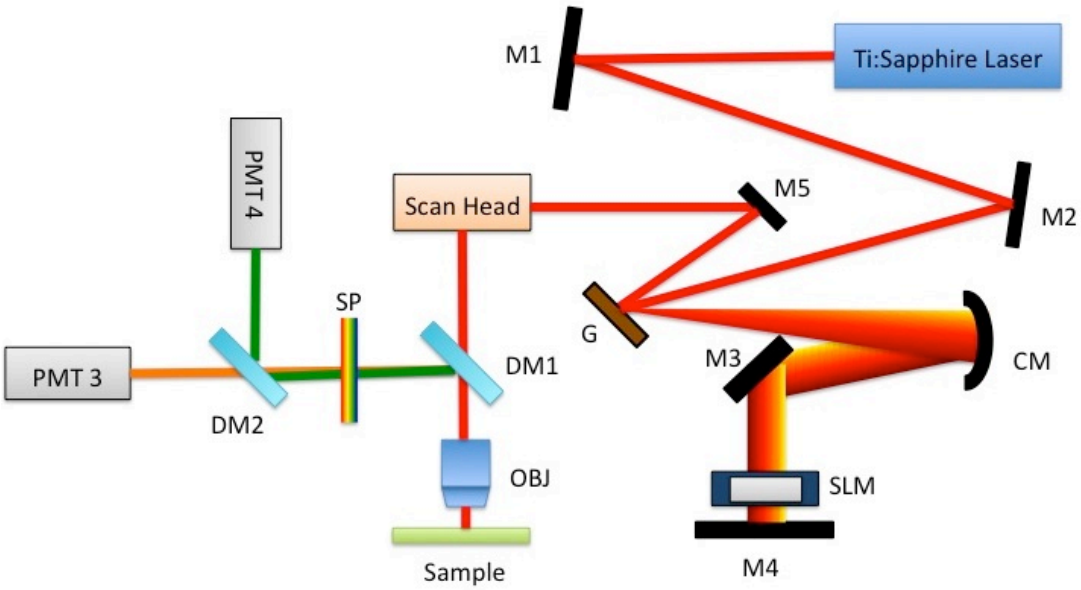

Figure 3.2 Experimental setup: M1-M5: mirrors, G = grating, CM = curved mirror, SLM = spatial light modulator, DM1 = 660DCXXR dichroic mirror, DM2 = 550DCXR dichroic mirror, OBJ = 60X 1.2 NA water immersion objective, SP = E650SP short pass filter.

Multiphoton intrapulse interference phase scan (MIIPS) was used to pre-compensate for dispersion caused by the microscope optics and achieve a near TL pulse at the sample.[20,24-26] An additional phase mask was added to the compression phase mask

to shape pulses for selective excitation. Pulse shapes were chosen according to the donor and acceptor two-photon absorption spectra (figure 3.3A). A model of our system combined with a genetic algorithm [MATLAB toolbox, Mathworks] was used to determine the phase mask for the ideal selective excitation of the donor and acceptor molecules. An ideal selective excitation is one that primarily excites either the donor or acceptor molecule, with minimal excitation of the other molecule. The resulting fluorescence has reduced cross-talk using this technique. The amplitude and phase of the laser spectrum after pre-compensation are accounted for in the model to accurately reflect the experimental system. Figure 3.3C shows the ideal selective excitations from our computational model. Differences between the computational model in figure 3.3C and the experimental results found in figure 3.3B are due to attenuation from the experimental collection optics.

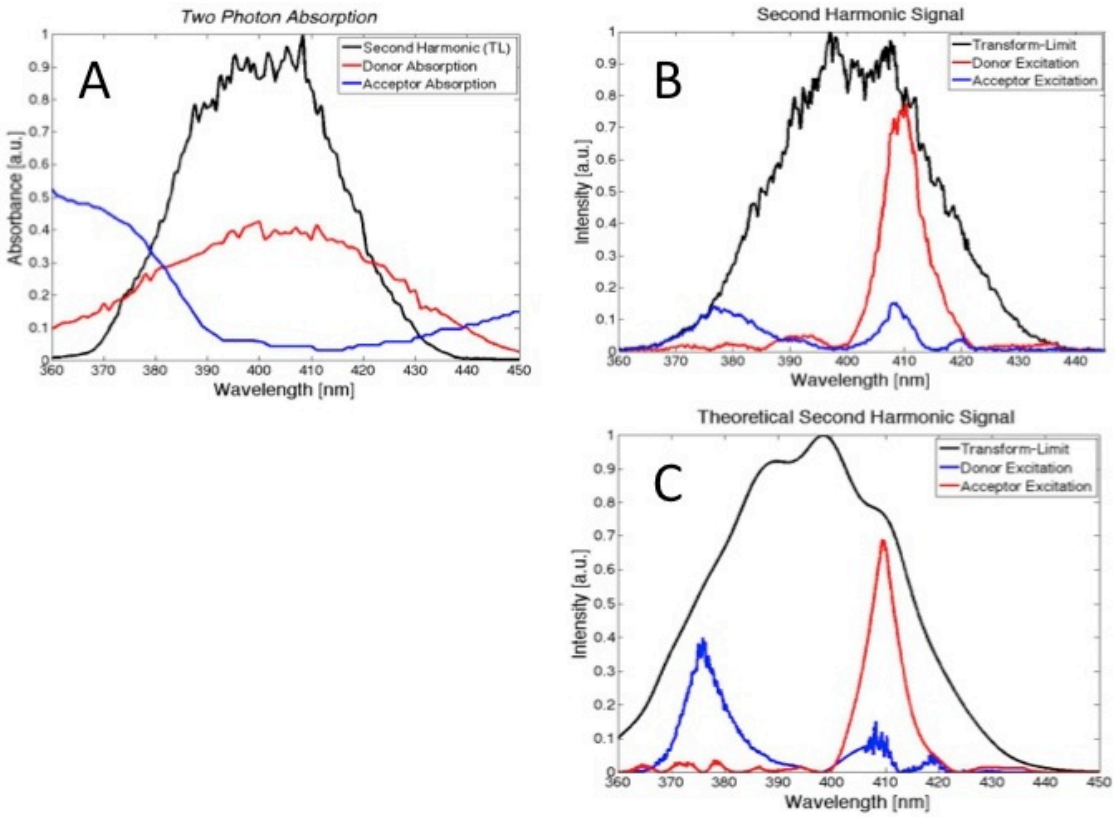

Figure 3.3 Two-photon absorption of donor (mAmetrine) and acceptor (tdTomato), with second harmonic overlap (A).[29] Selective two-photon excitation of donor (red) and acceptor (blue) and second harmonic overlap (black) (B). Computational model of ideal selective two-photon excitation from genetic algorithm, the phase of which is supplied to the experimental SLM.

The poor selectivity of the acceptor pulse (blue) is made up for by the substantial selectivity of the donor pulse. Differences in fluorophore quantum yield and filter choices require the pulse shapes to achieve comparable image quality for the different fluorophores given the same average power. The resulting balanced emission detection is optimized for signal to noise, reduces image acquisition time, and reduces unnecessary illumination of the sample. An initial population of a hundred binary phase masks are generated using a prime number based destructive interference scheme.[20,27] Convergence to the ideal phase mask took approximately 2 minutes for each mask. This approach is

significantly faster than a genetic algorithm feedback loop integrated into the experimental systems, which can take hours to converge depending on excitation type and initial population.[28] The SLM response time of 35 ms allows for rapid switching between pulse shapes. The two excitation conditions and two detection channels generate 4 distinct images: labeled I_A, I_D, I_F and I_N.

3.2.3 Image Processing

Each microscope image is comprised of 512 x 512 pixels with a total image size of $223\mu m$ x $223\mu m$. An image acquisition time of approximately 50 s was a result of the 12 μs pixel dwell time and averaging of 16 exposures. Image processing and analysis was performed in MATLAB. All images were background-subtracted using the average shuttered PMT dark counts and shading-corrected using the shading profile from a fluorescence slide. After correction for background and shading, corrected images were analyzed with a watershed algorithm and a single binary mask was used to select individual cells from images.[30] Thresholding algorithms were used to choose pixels with intensities in the PMT linear response regime (away from saturation as well as dark noise floor).

3.2.4 Determination of Efficiency by Fluorescence Lifetime

The fluorescence lifetime of cells expressing donor (mAmetrine) and the linked donor-acceptor (mAmetrine-tdTomato) construct were measured with a fluorescence lifetime imaging microscope (FLIM) configured for time-correlated single photon counting. The FLIM measurements were performed using an Olympus IX-81 microscope with a 60X 1.2NA water immersion objective. A supercontinuum excitation

source (Fianium SC 400-6-PP) having a repetition rate of 20 MHz, ~100-ps pulse duration and configured with an acousto-optic tunable filter was used for picking the excitation wavelengths. Single photon detection was performed with two Hamamatsu H7422P-40 PMTs.

The donor lifetime was fit to a bi-exponential decay both in the absence as well as presence of FRET. From the average fluorescence lifetime of mAmetrine and of mAmetrine-tdTomato in complex, the FRET efficiency, E, was determined to be 0.29 inside cells according to the relation:

$$E = \left[1 - \frac{\tau_{DA}}{\tau_D} \right] \tag{3.2}$$

where $\tau_D = 3.19ns$ and $\tau_{DA} = 2.26ns$ are the experimentally measured fluorescence lifetimes of mAmetrine alone and mAmetrine-tdTomato linked construct respectively.

3.3 Derivation of Two-Photon FRET Stoichiometry

The two-photon FRET stoichiometry theory proposed in this manuscript is a generalization of the one-photon variant published by Hoppe *et al.*.[7] The same notation, $F_x\left(\lambda_{\#}^{*}\lambda_{\#}^{*}\right)$, will be used for consistency. The subscript X represents the origin of the fluorescence signal, either D for donor, A for acceptor, or T for fluorescence due to FRET. The # subscript identifies the wavelengths corresponding to the variables D or A. Finally, the * superscript denotes the excitation and emission condition. As an example of this notation, the term $F_D\left(\lambda_A^{ex}\lambda_D^{ex}\right)$ refers to fluorescence signal from the donor

molecules when excited at the acceptor's excitation wavelengths and collected at the donor's emission wavelengths.

A microscope image is made up of three signals: emission from the acceptor, F_A, emission from the donor, F_D, and emission from the donor-acceptor complex, F_C. Signals from the donor-acceptor complex may be further broken down into emission from the donor, F_{DC}, emission from the acceptor not due to FRET, F_{AC}, and emission from the acceptor due to FRET, F_T. As FRET efficiency is not 100%, donor molecules in complex will have some emission resulting in $F_{DC} \neq 0$. Similarly, the acceptor in the complex may be directly excited by the same wavelengths used to excite the donor, resulting in direct acceptor emission, F_{AC}. It is not possible to distinguish fluorescence from the donor in complex from that of the free donor. Likewise, signal from the acceptor in complex cannot be distinguished from that of the free acceptor. As the terms F_D and F_A already contain the signal associated with F_{DC} and F_{AC}, the latter two terms will not be independently considered. The signal recorded at any given pixel in a microscope image can therefore be simplified into the three components: donor emission, F_D, acceptor emission (not due to FRET), F_A, and acceptor emission due to FRET, F_T.

The following derivation will relate microscope images to the previously mentioned terms. Three images are considered, a FRET image, I_F, an acceptor image, I_A, and a donor image, I_D, defined in terms of the contributing fluorophores' signals:

$$\begin{aligned} I_F &= F\left(\lambda_D^{ex}\lambda_A^{em}\right) = F_D\left(\lambda_D^{ex}\lambda_A^{em}\right) + F_A\left(\lambda_D^{ex}\lambda_A^{em}\right) + F_T\left(\lambda_D^{ex}\lambda_A^{em}\right) \\ I_A &= F\left(\lambda_A^{ex}\lambda_A^{em}\right) = F_D\left(\lambda_A^{ex}\lambda_A^{em}\right) + F_A\left(\lambda_A^{ex}\lambda_A^{em}\right) + F_T\left(\lambda_A^{em}\lambda_A^{em}\right) \\ I_D &= F\left(\lambda_D^{ex}\lambda_D^{em}\right) = F_D\left(\lambda_D^{ex}\lambda_D^{em}\right) + F_A\left(\lambda_D^{ex}\lambda_D^{em}\right) + F_T\left(\lambda_D^{em}\lambda_D^{em}\right) \end{aligned} \tag{3.3}$$

Depending on the experimental conditions used, namely, the choice of fluorophores, excitation wavelengths, and emission filters, some of the terms in these three equations may go to zero. For example, Hoppe *et al.* assumed

$$F_T\left(\lambda_D^{ex}\lambda_D^{em}\right)=0$$
$$F_T\left(\lambda_A^{ex}\lambda_A^{em}\right)=0 \tag{3.4}$$

since they selected fluorophores with minimal cross-talk in the one-photon excitation regime. For the purposes of this derivation, the most general case is considered and all terms are kept. This is pertinent in the case of two-photon excitation, where the donor and acceptor have significant two-photon cross-section overlap. For example, the donor's excited state can be populated with excitation at the acceptor's excitation wavelengths. Similarly, the donor emission channel may be contaminated with signal originating from acceptor emission. Finally, when FRET does occur, the F_D terms must accommodate the associated decrease in signal contribution from donor fluorescence. For these reasons, the relations in equation 3.4 are no longer valid.

The first step in the two-photon FRET stoichiometry derivation requires us to find an expression for f_A, the fraction of acceptor molecules in complex, in terms of microscope observables. We start with a modified two-photon excitation FRET efficiency:[31]

$$E=\frac{\sigma_A\left(\lambda_D^{ex}\right)}{\sigma_D\left(\lambda_D^{ex}\right)}\left[\frac{F_{AD}\left(\lambda_D^{ex}\lambda_A^{em}\right)}{F_A\left(\lambda_D^{ex}\lambda_A^{em}\right)}-1\right]\left(\frac{1}{f_A}\right) \tag{3.5}$$

where F_{AD} is the fluorescence from the acceptor in the presence of the donor and F_A is the fluorescence from the acceptor in the absence of the donor. The ratio of the acceptor and donor two-photon cross-sections at the donor's excitation wavelengths will be referred to

as γ throughout the derivation, $\gamma = \sigma_A\left(\lambda_D^{ex}\right)/\sigma_D\left(\lambda_D^{ex}\right)$. The term $F_{AD}\left(\lambda_D^{ex}\lambda_a^{em}\right)$ can be written as

$$F_{AD}\left(\lambda_D^{ex}\lambda_A^{em}\right) = F_A\left(\lambda_D^{ex}\lambda_A^{em}\right) + F_T\left(\lambda_D^{ex}\lambda_A^{em}\right) \tag{3.6}$$

where this signal originates only from the acceptor. In an actual experiment, this term will contain some donor emission that overlaps with acceptor emission channel. This is accounted for by rewriting $F_{AD}\left(\lambda_D^{ex}\lambda_A^{ex}\right)$ in terms of the microscope image, I_F, resulting in the relationship

$$F_{AD}\left(\lambda_D^{ex}\lambda_A^{em}\right) = I_F - F_D\left(\lambda_D^{ex}\lambda_A^{em}\right) \tag{3.7}$$

Since $F_D\left(\lambda_D^{ex}\lambda_A^{ex}\right)$ must also be expressed in terms of the images I_A, I_D, and I_F, we introduce the cross-talk constant β given by

$$\beta = \frac{F_D\left(\lambda_D^{ex}\lambda_A^{em}\right)}{F_D\left(\lambda_D^{ex}\lambda_D^{em}\right)} = \frac{I_F}{I_D} \tag{3.8}$$

relating the donor fluorescence detected at the acceptor emission wavelength relative to that detected at the donor wavelength emission (due to the dichroic splitting ratio). We can then solve for $F_D\left(\lambda_D^{ex}\lambda_D^{ex}\right)$ in terms of microscope images with the relationship

$$F_D\left(\lambda_D^{ex}\lambda_D^{em}\right) = I_D - F_A\left(\lambda_D^{ex}\lambda_D^{em}\right) - F_T\left(\lambda_D^{ex}\lambda_D^{em}\right) \tag{3.9}$$

We define the constant, η, which corresponds to the ratio

$$\eta = \frac{F_A\left(\lambda_D^{ex}\lambda_A^{em}\right)}{F_A\left(\lambda_D^{ex}\lambda_D^{em}\right)} = \frac{F_A\left(\lambda_A^{ex}\lambda_A^{em}\right)}{F_A\left(\lambda_A^{ex}\lambda_D^{em}\right)} = \frac{I_A}{I_N} \tag{3.10}$$

and accounts for how the dichroic mirror splits the acceptor fluorescence between detection channels. Substituting η into equation 3.10, we find

$$F_D\left(\lambda_D^{ex}\lambda_D^{em}\right) = I_D - \left(\frac{1}{\eta}\right)F_A\left(\lambda_D^{ex}\lambda_A^{em}\right) - F_T\left(\lambda_D^{ex}\lambda_D^{em}\right) \tag{3.11}$$

Since the acceptor will fluoresce at the same wavelengths whether it is excited directly or via FRET, η can also be used to quantify how the F_T signal splits between detection channels with the relationship

$$\eta = \frac{F_T\left(\lambda_D^{ex}\lambda_A^{em}\right)}{F_T\left(\lambda_D^{ex}\lambda_D^{em}\right)} = \frac{F_T\left(\lambda_A^{ex}\lambda_A^{em}\right)}{F_T\left(\lambda_A^{ex}\lambda_D^{em}\right)} \tag{3.12}$$

Substituting equation 3.12 into equation 3.11 results in

$$F_D\left(\lambda_D^{ex}\lambda_D^{em}\right) = I_D - \frac{1}{\eta}\left(F_A\left(\lambda_D^{ex}\lambda_A^{em}\right) + F_T\left(\lambda_D^{ex}\lambda_A^{em}\right)\right) \tag{3.13}$$

Equation 3.13 can then be substituted into equation 8 to obtain

$$F_{AD}\left(\lambda_D^{ex}\lambda_A^{em}\right) = I_F - \beta\left[I_D - \frac{1}{\eta}\left(F_A\left(\lambda_D^{ex}\lambda_A^{em}\right) + F_T\left(\lambda_D^{ex}\lambda_A^{em}\right)\right)\right] \tag{3.14}$$

Since $F_{AD}\left(\lambda_D^{ex}\lambda_A^{ex}\right)$ has already been defined as

$$F_{AD}\left(\lambda_D^{ex}\lambda_A^{em}\right) = F_A\left(\lambda_D^{ex}\lambda_A^{em}\right) + F_T\left(\lambda_D^{ex}\lambda_A^{em}\right) \tag{3.15}$$

substituting equation 3.14 and equation 3.15 leads to the relationship for $F_{AD}\left(\lambda_D^{ex}\lambda_A^{em}\right)$ as

$$F_{AD}\left(\lambda_D^{ex}\lambda_A^{em}\right) = \frac{I_F - \beta I_D}{1 - \frac{\beta}{\eta}} \tag{3.16}$$

Now we may turn our attention to solving $F_A\left(\lambda_D^{ex}\lambda_A^{ex}\right)$ in terms of microscope observables. First, the constant α is defined as

$$\alpha = \frac{F_A\left(\lambda_D^{ex}\lambda_A^{em}\right)}{F_A\left(\lambda_A^{ex}\lambda_A^{em}\right)} = \frac{I_F}{I_A} \tag{3.17}$$

similar to that of the one-photon theory. Using the earlier definition for the image I_A, we can rearrange the terms to have the relationship

$$F_A\left(\lambda_A^{ex}\lambda_A^{em}\right) = I_A - F_D\left(\lambda_A^{ex}\lambda_A^{em}\right) - F_T\left(\lambda_A^{ex}\lambda_A^{em}\right) \tag{3.18}$$

An additional constant, θ, is defined as

$$\theta = \frac{F_D\left(\lambda_D^{ex}\lambda_D^{em}\right)}{F_D\left(\lambda_A^{ex}\lambda_D^{em}\right)} = \frac{F_D\left(\lambda_D^{ex}\lambda_A^{em}\right)}{F_D\left(\lambda_A^{ex}\lambda_A^{em}\right)} \tag{3.19}$$

which is the ratio of donor fluorescence obtained when excited with donor vs. acceptor excitation wavelength. Implementing θ and β into equation 3.18 yields the relationship

$$F_A\left(\lambda_A^{ex}\lambda_A^{em}\right) = I_A - \left(\frac{\beta}{\theta}\right)F_D\left(\lambda_D^{ex}\lambda_D^{em}\right) - F_T\left(\lambda_A^{ex}\lambda_A^{em}\right) \tag{3.20}$$

Using equations 3.13 and 3.15 in equation 3.20 results in

$$F_A\left(\lambda_A^{ex}\lambda_A^{em}\right) = I_A - \left(\frac{\beta}{\theta}\right)\left[I_D - \left(\frac{1}{\eta}\right)F_{AD}\left(\lambda_D^{ex}\lambda_A^{em}\right)\right] - F_T\left(\lambda_A^{ex}\lambda_A^{em}\right) \tag{3.21}$$

Since FRET efficiency is constant regardless of donor excitation wavelength, the constant θ can be used to relate the $F_T\left(\lambda_A^{ex}\lambda_A^{ex}\right)$ term for the case of donor excitation as

$$F_T\left(\lambda_A^{ex}\lambda_A^{em}\right) = \frac{1}{\theta}F_T\left(\lambda_D^{ex}\lambda_A^{em}\right) = \frac{1}{\theta}\left[F_{AD}\left(\lambda_D^{ex}\lambda_A^{em}\right) - F_A\left(\lambda_D^{ex}\lambda_A^{em}\right)\right] \tag{3.22}$$

Substituting equation 3.22 into equation 3.21 and replacing the terms $F_{AD}\left(\lambda_D^{ex}\lambda_A^{ex}\right)$ with previously found value in equation 3.16, $F_A\left(\lambda_D^{ex}\lambda_A^{em}\right)$ is rewritten as

$$F_A\left(\lambda_D^{ex}\lambda_A^{em}\right)=\frac{\theta\alpha}{\theta-\alpha}I_A-\frac{\theta\alpha}{\theta-\alpha}I_F \tag{3.23}$$

Having solved for both $F_A\left(\lambda_D^{ex}\lambda_A^{em}\right)$ and $F_{AD}\left(\lambda_D^{ex}\lambda_A^{em}\right)$ in terms of image parameters, the FRET efficiency (equation 3.5) may be expressed as

$$E=\gamma\left[\frac{\frac{\eta}{\eta-\beta}I_F-\frac{\beta\eta}{\eta-\beta}I_D}{\frac{\theta\alpha}{\theta-\alpha}I_A-\frac{\theta\alpha}{\theta-\alpha}I_F}-1\right]\frac{1}{f_A} \tag{3.24}$$

In its current state, equation 3.24 has three unknowns, E, γ, and f_A. Our technique requires *a priori* knowledge of the FRET efficiency, E, which may be determined experimentally via FLIM measurements (as discussed in the previous section) prior to the stoichiometric measurements. The variable γ may then be solved for by imaging a sample only containing the donor-acceptor construct, and assigning $f_A = 1$. Once γ has been determined, our last unknown, f_A, can be found for samples containing an unknown quantity of acceptor molecules in complex.

The next step in our derivation is to determine the fraction of donor in complex, f_D. In this case, an alternate equation for FRET efficiency is used based on the characteristic decrease in donor fluorescence

$$E=\left[1-\frac{F_{DA}\left(\lambda_D^{ex}\lambda_D^{em}\right)}{F_{DO}\left(\lambda_D^{ex}\lambda_D^{em}\right)}\right]\left(\frac{1}{f_D}\right) \tag{3.25}$$

Here, $F_{DA}\left(\lambda_D^{ex}\lambda_D^{em}\right)$ represents the signal from the donor in the presence of the acceptor, and $F_{DO}\left(\lambda_D^{ex}\lambda_D^{em}\right)$ represents the signal from the donor in the absence of the acceptor. These two terms must be defined in terms of images taken in the microscope. First, $F_{DA}\left(\lambda_D^{ex}\lambda_D^{em}\right)$ is defined by rearranging equation 3.3 for I_D to obtain

$$F_{DA}\left(\lambda_D^{ex}\lambda_D^{em}\right)=F\left(\lambda_D^{ex}\lambda_D^{em}\right)=I_D-F_A\left(\lambda_D^{ex}\lambda_D^{em}\right)-F_T\left(\lambda_D^{em}\lambda_D^{em}\right) \tag{3.26}$$

The last two terms have previously been defined and equation 3.26 may be reduced to

$$F_{DA}\left(\lambda_D^{ex}\lambda_D^{em}\right)=\frac{1}{\eta-\beta}\left[\eta I_D-I_F\right] \tag{3.27}$$

Solving for $F_{DO}\left(\lambda_D^{ex}\lambda_D^{em}\right)$ is performed following the same protocol as the original one-photon FRET stoichiometry theory[7] using

$$F_{DO}\left(\lambda_D^{ex}\lambda_D^{em}\right)=F_T\left(\lambda_D^{ex}\lambda_A^{em}\right)\xi+F_{DA}\left(\lambda_D^{ex}\lambda_D^{em}\right) \tag{3.28}$$

where the constant ξ accounts for the excitation transferred from donor to acceptor which would otherwise have emitted in the donor channel. Thus, ξ is a function of quantum yields of donor and acceptor as well as detection efficiencies of donor and acceptor detection channels. While the last term is defined in equation 3.27, the first term, $F_T\left(\lambda_D^{ex}\lambda_A^{em}\right)$, is found by rearranging equation 3.3 for I_F resulting in

$$F_T\left(\lambda_D^{ex}\lambda_A^{em}\right)=I_F-F_D\left(\lambda_D^{ex}\lambda_A^{em}\right)-F_A\left(\lambda_D^{ex}\lambda_A^{em}\right) \tag{3.29}$$

where expressions for $F_D\left(\lambda_D^{ex}\lambda_A^{em}\right)$ and $F_A\left(\lambda_D^{ex}\lambda_A^{em}\right)$ are found using β, equations 3.27 and 3.23, respectively. The resulting expression for $F_T\left(\lambda_D^{ex}\lambda_A^{em}\right)$ is

$$F_T\left(\lambda_D^{ex}\lambda_A^{em}\right)=I_F\left(\frac{(\eta\theta-\beta\alpha)}{(\theta-\alpha)(\eta-\beta)}\right)-I_D\left(\frac{\beta\eta}{(\eta-\beta)}\right)-I_A\left(\frac{\alpha\theta}{(\theta-\alpha)}\right) \tag{3.30}$$

Combining these results into equation 3.25 results in the FRET efficiency relation

$$E=\left[1-\frac{\left(\frac{1}{\eta-\beta}\right)(\eta I_D-I_F)}{\xi\left(\left(\frac{\eta\theta-\beta\alpha}{(\theta-\alpha)(\eta-\beta)}\right)I_F-\left(\frac{\beta\eta}{\eta-\beta}\right)I_D-\left(\frac{\alpha\theta}{\theta-\alpha}\right)I_A\right)+\left(\frac{1}{\eta-\beta}\right)(\eta I_D-I_F)}\right]\frac{1}{f_D} \tag{3.31}$$

Imaging a sample containing only the donor-acceptor construct ensures $f_D=1$, and knowing the FRET efficiency, E, the variable ξ can be determined. The last unknown, f_D, can then be found for samples containing an unknown quantity of donor molecules in complex. Taking the initial one-photon assumptions, where $F_A\left(\lambda_D^{ex}\lambda_D^{ex}\right)$ and $F_D\left(\lambda_A^{ex}\lambda_A^{ex}\right)$ are zero, η and θ go to infinity and our relations for γ, ξ, f_A, and f_D converge to the one-photon theory.

The final stoichiometric quantity desired is R, the molar ratio of acceptor molecules to donor molecules. This can be found by simply taking the ratio of the two expressions, f_D and f_A.

$$R=\frac{f_D}{f_A}=\frac{[A_T]}{[D_T]} \tag{3.32}$$

3.4 Determination of Parameters: α, β, η, θ, γ, ξ

The parameters α and β are calculated according to the equations:

$$\alpha=\frac{F_A\left(\lambda_D^{ex}\lambda_A^{em}\right)}{F_A\left(\lambda_A^{ex}\lambda_A^{em}\right)}=\frac{I_F}{I_A} \tag{3.33}$$

$$\beta = \frac{F_D\left(\lambda_D^{ex}\lambda_A^{em}\right)}{F_D\left(\lambda_D^{ex}\lambda_D^{em}\right)} = \frac{I_F}{I_D} \tag{3.34}$$

from cells expressing only acceptor and donor respectively. This step is identical to previously published work (7). The α and β values for our system were found to be 0.33 and 0.25. In a similar manner, η and θ are determined from cells expressing only acceptor and only donor respectively, given by the relations:

$$\eta = \frac{F_A\left(\lambda_D^{ex}\lambda_A^{em}\right)}{F_A\left(\lambda_D^{ex}\lambda_D^{em}\right)} = \frac{F_A\left(\lambda_A^{ex}\lambda_A^{em}\right)}{F_A\left(\lambda_A^{ex}\lambda_D^{em}\right)} = \frac{I_A}{I_N} \tag{3.35}$$

$$\theta = \frac{F_D\left(\lambda_D^{ex}\lambda_D^{em}\right)}{F_D\left(\lambda_A^{ex}\lambda_D^{em}\right)} = \frac{I_D}{I_N} \tag{3.36}$$

The η and θ values were found to be 5.92 and 2.22. Using equations for f_A and f_D, in which I_A, I_D, and I_F were collected from 59 cells expressing only the FRET construct, γ and ξ were found using the relationship

$$\gamma_{TPE} = E\left[\frac{\frac{\eta}{\eta-\beta}I_F - \frac{\beta\eta}{\eta-\beta}I_D}{\frac{\theta\alpha}{\theta-\alpha}I_A - \frac{\theta\alpha}{\theta-\alpha}I_F} - 1\right]^{-1} \tag{3.37}$$

and

$$\xi = \frac{\gamma_{TPE} E\left(\frac{1}{\eta-\beta}(\eta I_D - I_F)\right)}{(1-E)\left(\left(\frac{\eta\theta-\beta\alpha}{(\theta-\alpha)(\eta-\beta)}\right)I_F - \left(\frac{\beta\eta}{\eta-\beta}\right)I_D - \left(\frac{\alpha\theta}{\theta-\alpha}\right)I_A\right)} \tag{3.38}$$

The γ and ξ values were found to be 0.30 and 1.03. From these values, the average f_A, f_D and R for a single cell as well as for an entire set of images was determined.

3.5 Results

The stoichiometry of an unknown system requires images I_A, I_D, and I_F from applying different excitation pulse shapes and emission filters. FRET decreases fluorescence from the donor and increases fluorescence from the acceptor (figure 3.1). In this case, the image I_D decreases in intensity and the I_F image increases in intensity. Overlapping excitation and emission spectra result in significant cross-talk between the PMT channels. The additional cross–talk terms, η and θ, correct for the spectral overlap of the two fluorophores enabling greater accuracy in the determination of γ, ξ, f_A, f_D, and R. 23 cells (acceptor only) were analyzed to calculate α and η, 42 cells (donor only) were analyzed for β and θ, and 59 cells (donor-acceptor linked construct) were analyzed for γ and ξ. The boundary conditions for f_A and f_D were tested to illustrate the increased accuracy of our theory to that of the one photon theory (table 3.2). For example, the 43 cells expressing unlinked donor and acceptor are expected to have f_A and f_D values of zero. All stoichiometry measurements of f_A, f_D, and R result in the expected value for the cell transfection type. The one-photon FRET stoichiometry has

similar results to the cross-talk corrected stoichiometry in the pure FRET case, but dramatically deviates in accuracy in the case of no FRET (table 3.2).

Table 3.2 FRET stoichiometry results for cell expression of combinations of linked and unlinked molecules. Expected values are in parenthesis.

	mAm-tdT	**mAm + tdT**	**mAm-tdT + tdT**	**mAm-tdT + mAm**
Number of Cells:	59	42	17	18
f_D ± SD (TPA)	1.00 ± 0.15 (1)	0.04 ± 0.06 (0)	0.76 ± 0.32 (1)	0.17 ± 0.07
f_A ± SD (TPA)	1.00 ± 0.25 (1)	0.06 ± 0.13 (0)	0.21 ± 0.10	0.77 ± 0.33 (1)
f_D ± SD (1PA)	1.00 ± 0.16 (1)	-0.21 ± 0.10 (0)	0.51 ± 0.35 (1)	0.01 ± 0.10
f_A ± SD (1PA)	1.00 ± 0.22 (1)	-0.30 ± 0.20 (0)	0.17 ± 0.13	0.03 ± 0.34 (1)

Cell images analyzed with our technique are shown color coded in Fig. 3.4 – 3.7 according to the fluorophores' expression in individual cells. The concentrations of donor and acceptor fluorophores vary between cells requiring our algorithm to accurately select individual cells for comparison. Variability between cells can result in large standard deviations. The functions used to characterize the ratio of donor and acceptor in complex require the presence of both the donor and acceptor. When a cell does not express any acceptor or donor, the measure of the molecule in complex becomes inaccurate due to the increased influence of noise in the corresponding channel. Images of cells expressing donor and acceptor not in complex are more susceptible to this error as can be seen in Fig 5. Cells expressing excess donor and excess acceptor are presented in Fig. 6 and Fig. 7 respectively.

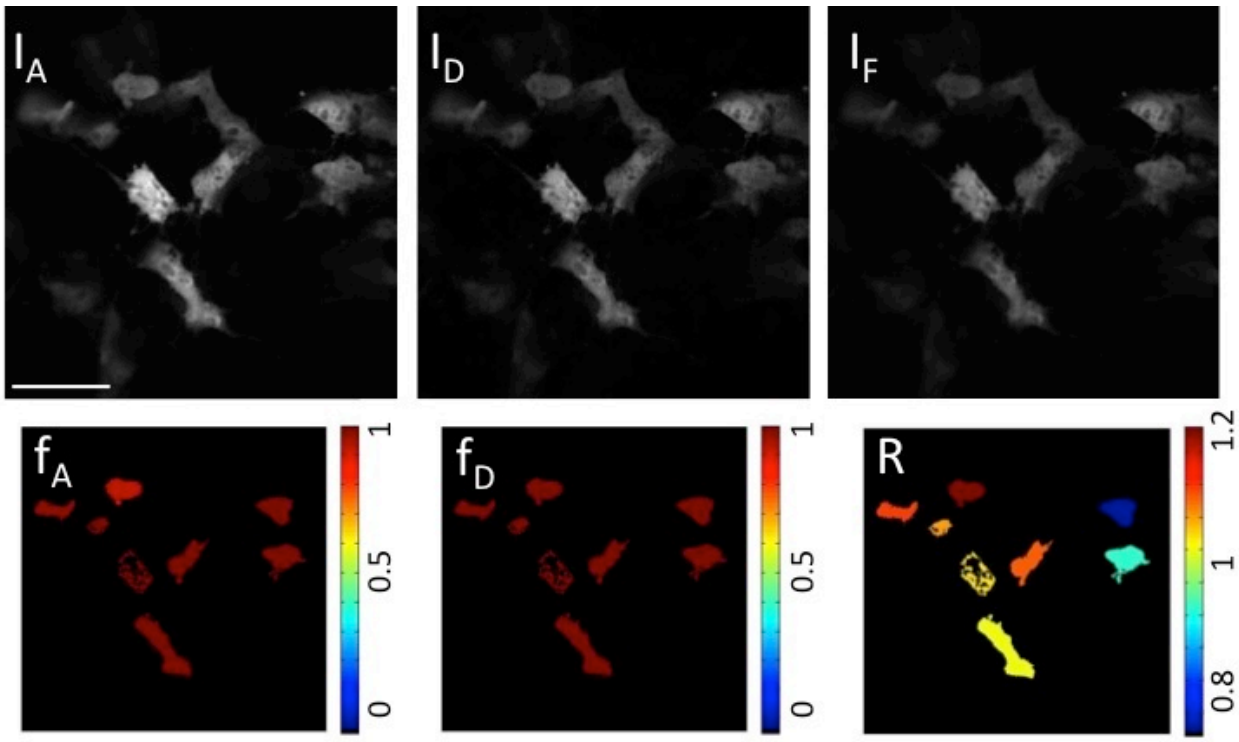

Figure 3.4 Top: Raw microscope images from channels I_A, I_D, and I_F for cells expressing linked construct mAmetrine-tdTomato. Bottom: Color coded cells after analysis for the cells expressing linked construct mAmetrine-tdTomato giving the ratio of acceptor in construct (f_A), ratio of donor in construct (f_D), and absolute concentration ratio (R). Scale bar insert $55\mu m$

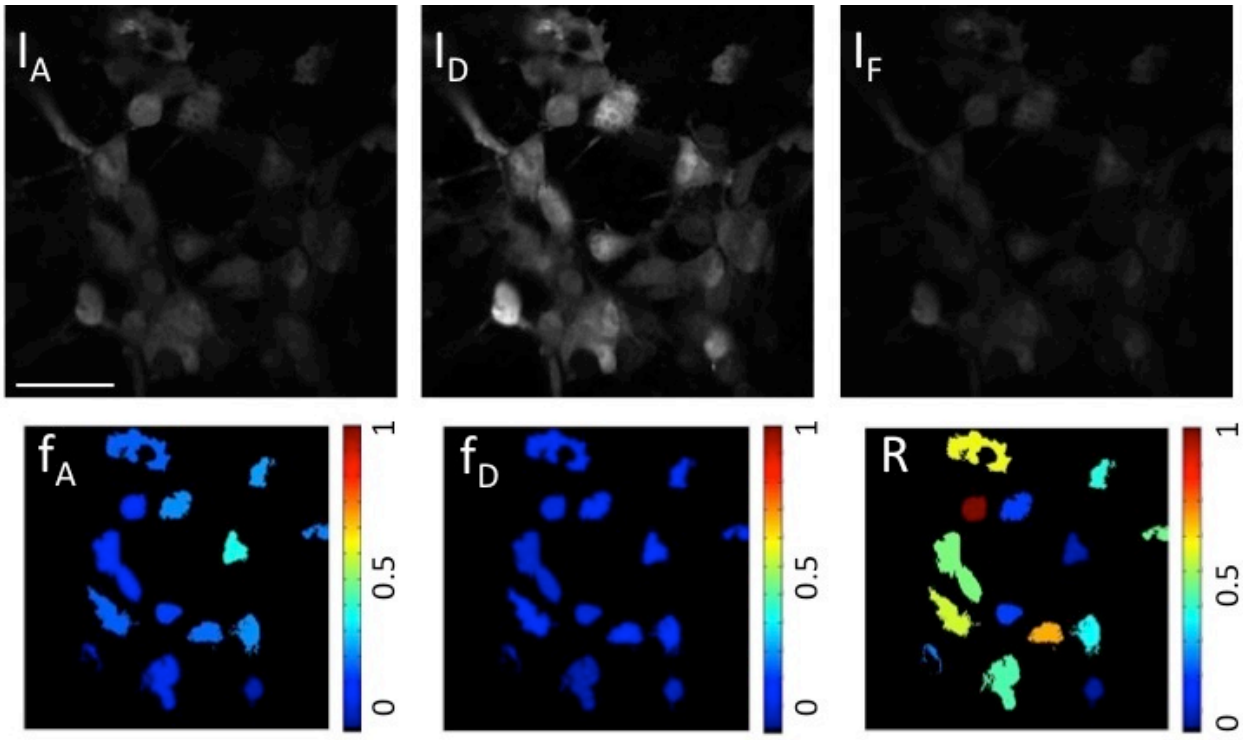

Figure 3.5 Raw microscope images from channels I_A, I_D, and I_F for cells expressing unlinked mAmetrine and tdTomato. Bottom: Color coded cells after analysis for cells expressing unlinked mAmetrine and tdTomato giving the ratio of acceptor in construct (f_A), ratio of donor in construct (f_D), and absolute concentration ratio (R). Scale bar insert $55\mu m$

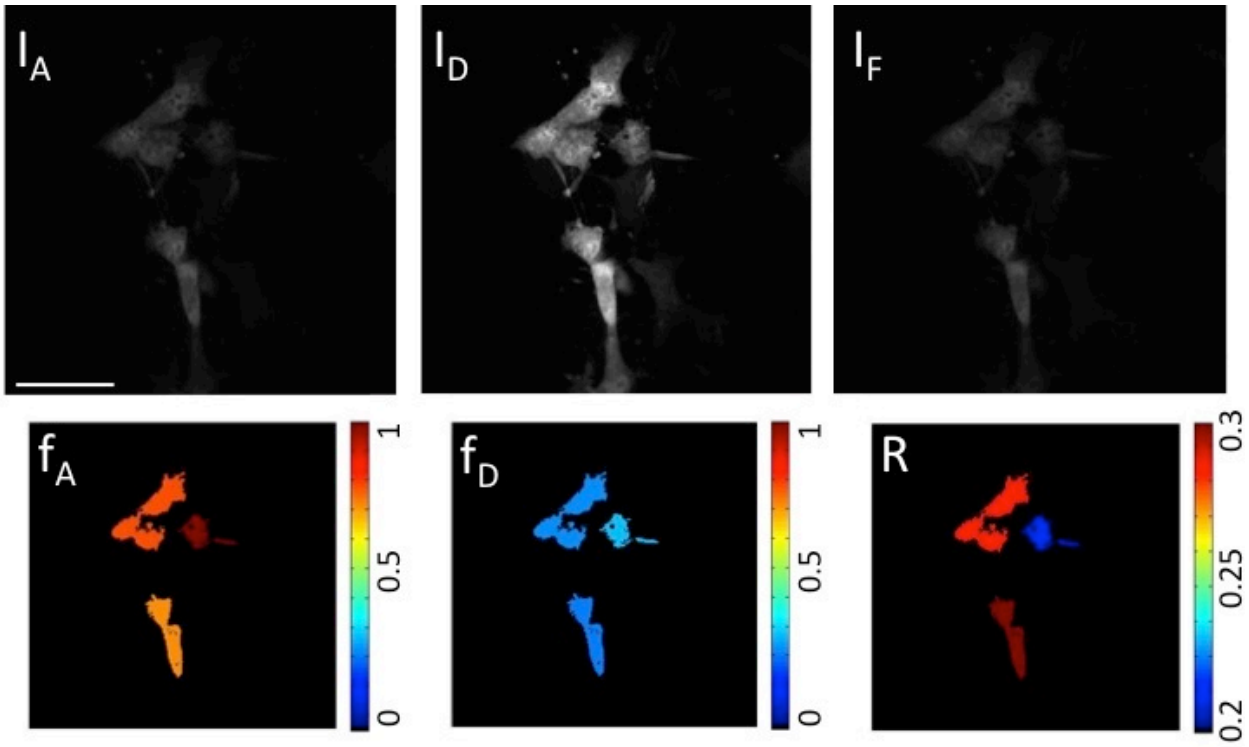

Figure 3.6 Raw microscope images from channels I_A, I_D, and I_F for cells expressing linked construct mAmetrine-tdTomato plus excess mAmetrine. Bottom: Color coded cells after analysis for linked cells expressing construct mAmetrine-tdTomato plus excess mAmetrine giving the ratio of acceptor in construct (f_A), ratio of donor in construct (f_D), and absolute concentration ratio (R). Scale bar insert $55\mu m$

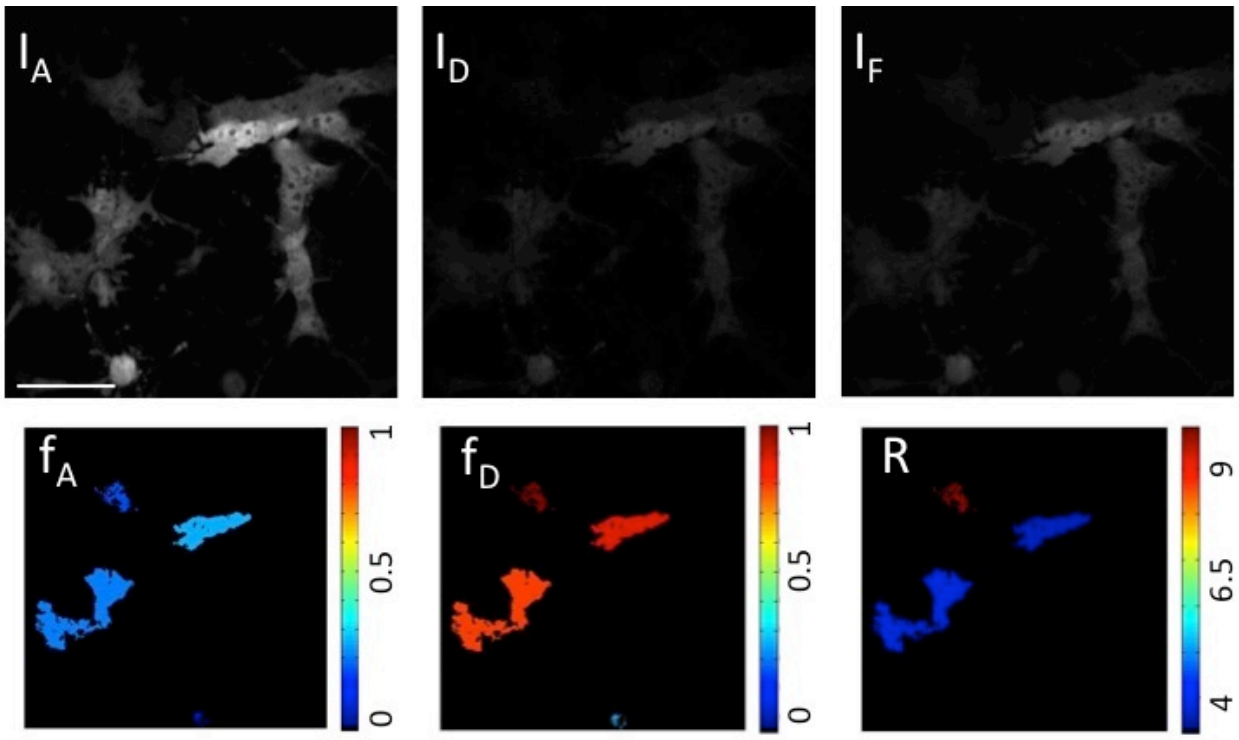

Figure 3.7 Raw microscope images from channels I_A, I_D, and I_F for cells expressing linked construct mAmetrine-tdTomato plus excess tdTomato. Bottom: Color coded cells after analysis for linked cells expressing construct mAmetrine-tdTomato plus excess tdTomato giving the ratio of acceptor in construct (f_A), ratio of donor in construct (f_D), and absolute concentration ratio (R). Scale bar insert $55\mu m$

Calculation of the donor in construct versus acceptor in construct determines the absolute concentration ratio of acceptor $[A_T]$ to donor $[D_T]$ via the relation, $R=[A_T]/[D_T]$. Excess acceptor will result in R > 1, excess donor will result in R < 1, and equal mole fraction of donor and acceptor results in R = 1. To test the method for calculating f_A, f_D and R, cells expressing the FRET construct plus excess acceptor, and FRET construct plus excess donor were imaged with our technique. In the case where the FRET construct plus acceptor is expressed, the observed f_A was found to be approximately 0.2. The observed f_D was ~ 0.8 (expected 1.0), with a large standard deviation suggesting high variability between cells as well as a systematic drift possibly due to low signal to

noise ratio in the donor channel. In the case where the FRET construct plus donor is expressed, the observed f_D was found to be approximately 0.2, suggesting a similar expression to the previous case. The measure of f_A also decreased to approximately 0.8, possibly showing susceptibility to the background noise.

FRET stoichiometry was able to accurately predict boundary conditions as well as combinations of molecules both in and out of construct. Large standard deviations for the average value for each system were possibly due to variance in cell expression and fluorophore photobleaching over the time duration of the experiment. Low expression of donor or acceptor resulted in an increase in standard deviation. At high average laser power (>2mW), cell autofluorescence contaminated the intensity channels, which prevented increasing the signal significantly above noise floor and decreased stoichiometry accuracy. An average power no greater than 2 mW was maintained throughout the experiments to reduce contributions from autofluorescence.

3.6 Discussion

Pulse-shaping based two-photon FRET stoichiometry has been applied to imaging live COS-7 cells. A one-photon stoichiometry theory was generalized to account for cross-talk in the two-photon excitation case. Two-photon selective excitation using pulse shaping allowed for quick transition between fluorophore excitation (on the order of 30 ms). The improved time resolution compared with tuning a Ti:sapphire laser allows for the possibility observing how the cellular stoichiometry evolve over time.

References:

[1] Selvin, P.R. 1995. [13] Fluorescence resonance energy transfer. Methods in enzymology.

[2] Alberts, B., A. Johnson, J. Lewis, M. Raff, K. Roberts, et al. 2007. Molecular Biology of the Cell, Fifth Edition. Garland Science.

[3] Selvin, P.R. 2000. The renaissance of fluorescence resonance energy transfer. Nature structural biology.

[4] Gordon, G.W., G. Berry, X.H. Liang, B. Levine, and B. Herman. 1998. Quantitative fluorescence resonance energy transfer measurements using fluorescence microscopy. Biophys. J.

[5] Xia, Z., and Y. Liu. 2001. Reliable and global measurement of fluorescence resonance energy transfer using fluorescence microscopes. Biophys. J.

[6] Erickson, M.G., B.A. Alseikhan, B.Z. Peterson, and D.T. Yue. 2001. Preassociation of Calmodulin with Voltage-Gated Ca 2+ Channels Revealed by FRET in Single Living Cells. Neuron.

[7] Hoppe, A., K. Christensen, and J.A. Swanson. 2002. Fluorescence Resonance Energy Transfer-Based Stoichiometry in Living Cells. Biophys. J. 83: 3652–3664.

[8] Raicu, V., D. Jansma, D. Miller, and J. Friesen. 2005. Protein interaction quantified in vivo by spectrally resolved fluorescence resonance energy transfer. Biochemistry Journal. : 265–277.

[9] Brousmiche, D.W., J.M. Serin, J.M.J. Fréchet, G.S. He, T.-C. Lin, et al. 2003. Fluorescence Resonance Energy Transfer in a Novel Two-Photon Absorbing System. J. Am. Chem. Soc. 125: 1448–1449.

[10] Wallrabe, H., M. Stanley, A. Periasamy, and M. Barroso. 2003. One- and two-photon fluorescence resonance energy transfer microscopy to establish a clustered distribution of receptor-ligand complexes in endocytic membranes. J. Biomed. Opt. 8: 339.

[11] Mills, J.D., J.R. Stone, D.G. Rubin, D.E. Melon, D.O. Okonkwo, et al. 2003. Illuminating protein interactions in tissue using confocal and two-photon excitation fluorescent resonance energy transfer microscopy. J. Biomed. Opt. 8: 347.

[12] Chou, K.-L., N. Won, J. Kwag, S. Kim, and J.-Y. Chen. 2013. Femto-second laser beam with a low power density achieved a two-photon photodynamic cancer therapy with quantum dots. J. Mater. Chem. B. 1: 4584.

[13] Fowley, C., N. Nomikou, A.P. McHale, B. McCaughan, and J.F. Callan. 2013. Extending the tissue penetration capability of conventional photosensitisers: a carbon quantum dot–protoporphyrin IX conjugate for use in two-photon excited photodynamic therapy. Chem. Commun. 49: 8934.

[14] Picard, S., E.J. Cueto-Diaz, E. Genin, G. Clermont, F. Acher, et al. 2013. Tandem triad systems based on FRET for two-photon induced release of glutamate. Chem. Commun. 49: 10805.

[15] Tang, J., B. Kong, H. Wu, M. Xu, Y. Wang, et al. 2013. Carbon Nanodots Featuring Efficient FRET for Real-Time Monitoring of Drug Delivery and Two-Photon Imaging. Adv. Mater. 25: 6569–6574.

[16] Raicu, V., M.R. Stoneman, R. Fung, M. Melnichuk, D.B. Jansma, et al. 2009. Determination of supramolecular structure and spatial distribution of protein complexes in living cells. Nature Photon. 3: 107–113.

[17] Thaler, C., S.V. Koushik, P.S. Blank, and S.S. Vogel. 2005. Quantitative Multiphoton Spectral Imaging and Its Use for Measuring Resonance Energy Transfer. Biophys. J. 89: 2736–2749.

[18] Zipfel, W.R., R.M. Williams, and W.W. Webb. 2003. Nonlinear magic: multiphoton microscopy in the biosciences. Nature Biotechnology.

[19] Ogilvie, J.P., D. Debarre, X. Solinas, J.L. Martin, E. Beaurepaire, et al. 2006. Use of coherent control for selective two-photon fluorescence microscopy in live organisms. Opt. Express. 14: 759–766.

[20] Lozovoy, V.V., and M. Dantus. 2005. Systematic Control of Nonlinear Optical Processes Using Optimally Shaped Femtosecond Pulses. ChemPhysChem. 6: 1970–2000.

[21] Brenner, M.H., D. Cai, S.R. Nichols, S.W. Straight, A.D. Hoppe, et al. 2012. Pulse shaping multiphoton FRET microscopy. SPIE BiOS. 8233: 82260R–82260R–7.

[22] Brenner, M.H., D. Cai, J.A. Swanson, and J.P. Ogilvie. 2013. Two-photon imaging of multiple fluorescent proteins by phase-shaping and linear unmixing with a single broadband laser. Opt. Express. 21: 17256–17264.

[23] Flynn, D.C., A.R. Bhagwat, and J.P. Ogilvie. 2013. Chemical-contrast imaging with pulse-shaping based pump-probe spectroscopy. In: Periasamy A, K König, PTC So, editors. SPIE. pp. 85881Z–85881Z–10.

[24] Cruz, Dela, J.M., I. Pastirk, V.V. Lozovoy, K.A. Walowicz, and M. Dantus. 2004.

Multiphoton intrapulse interference 3: Probing microscopic chemical environments. J. Phys. Chem. A. 108: 53–58.

[25] Coello, Y., V.V. Lozovoy, T.C. Gunaratne, B.W. Xu, I. Borukhovich, et al. 2008. Interference without an interferometer: a different approach to measuring, compressing, and shaping ultrashort laser pulses. J. Opt. Soc. Am. B-Opt. Phys. 25: A140–A150.

[26] Xu, B.W., J.M. Gunn, J.M. Dela Cruz, V.V. Lozovoy, and M. Dantus. 2006. Quantitative investigation of the multiphoton intrapulse interference phase scan method for simultaneous phase measurement and compensation of femtosecond laser pulses. J. Opt. Soc. Am. B-Opt. Phys. 23: 750–759.

[27] Comstock, M., V.V. Lozovoy, I. Pastirk, and M. Dantus. 2004. Multiphoton intrapulse interference 6; binary phase shaping. Multiple values selected. 12: 1061.

[28] Baumert, T., T. Brixner, V. Seyfried, M. Strehle, and G. Gerber. 1997. Femtosecond pulse shaping by an evolutionary algorithm with feedback. Appl Phys B. 65: 779–782.

[29] Drobizhev, M., Makarov, N.S., Tillo, S.E., Hughes, T.E., and Rebane, A., "Describing Two-Photon Absorptivity of Fluorescent Proteins with a New Vibronic Coupling Mechanism," Journal of Physical Chemistry B 116(5), 1736–1744 (2012).

[30] Gonzalez, R.C., and R.E. Woods. 2011. Digital Image Processing. Pearson Higher Ed.

[31] Lakowicz, J.R. 2007. Principles of Fluorescence Spectroscopy. Springer.

Chapter 4 Pump-Probe Microscopy

4.1 Introduction

In the previous chapter, pulse shaping was used to compress a pulse after a microscope objective to the TL. Using binary phase masks, selective excitation pulses were created and used to image cells expressing multiple GFP variants. In this section, we describe the addition of a second beam and pulse shaper to the optical setup. The addition enables the optical control of material responses beyond fluorescence. The analogy of a musical score is revisited to illustrate not just the increase in dynamic range, but to highlight the increased sophistication to our technique.

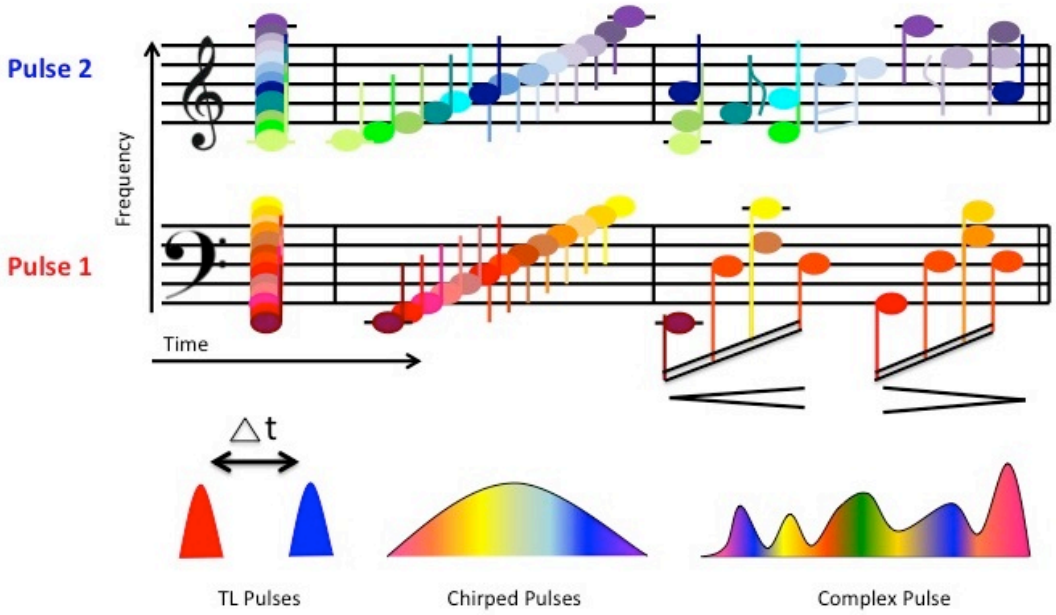

Figure 4.1 Musical score cartoon illustrating increase in dynamic range and optical control.

4.2 Experimental Design

The home built multiphoton microscope (Figure 4.2) employs a femtosecond oscillator (Venteon Pulse: One, 80 MHz, 600 mW avg. power, >300 nm bandwidth) having transform-limited pulses with 7-fs pulse duration and 650 - 1000 nm spectrum (Figure 4.3a). The fundamental beam is split by a beamsplitter (BS), directing 70% of the fundamental beam as the pump beam and the remaining 30% for generating the probe beam via second harmonic (SH) generation. The pump beam is modulated with an electro-optic modulator (Conoptics Model 350-160 KD*P) at 2 MHz (50% duty cycle). The modulated pump beam is then sent to a spatial light modulator (SLM) based pulse-shaping setup (BioPhotonic Solutions MIIPS BOX 640) that compensates for the large dispersion from the microscope objective and electro-optic modulator using the MIIPS algorithm to obtain a near-transform-limited pulse duration at the sample.[1,2] The

optimized phase mask compresses the pump pulse at the focus generating a SH spectrum with 40 nm FWHM bandwidth (Figure 4.3b). From the interferometric autocorrelation of the pump pulse (Figure 4.3c), and assuming a hyperbolic secant squared pulse, a sub-40fs pulse is incident at the sample.

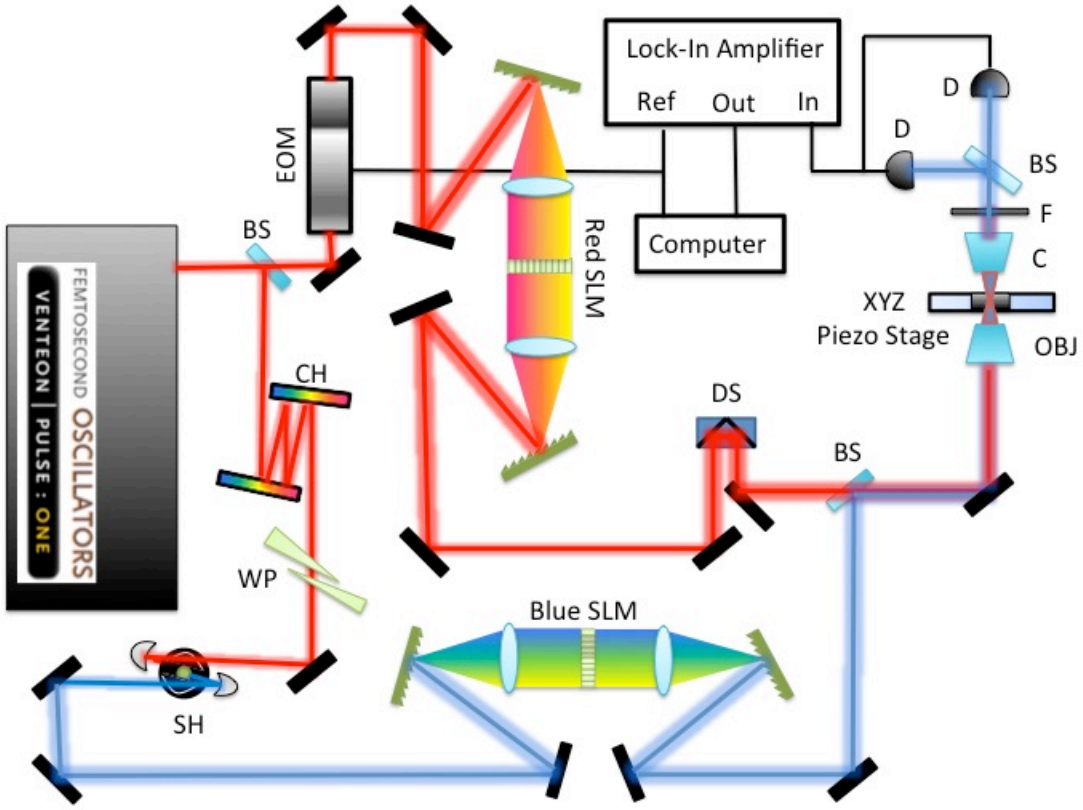

Figure 4.2 Pump-probe microscopy setup; BS: beam splitter, EOM: Electro-Optic modulator, CH: chirped mirrors, WP: wedge pair, SH: second harmonic setup, DS: delay stage, OBJ: 40X 0.6 NA objective, C: 0.8 NA condenser, F: filter, D: balanced diodes.

The second harmonic probe beam is obtained by compensating for second order dispersion of air with a combination of chirped mirrors and a wedge pair combination. The nearly transform-limited pulse is then focused onto a 100 μm thick BBO crystal with a spherical mirror (f = 12mm) as discussed by Furbach *et. al.* providing SH light with

approximately 3 mW average power and a large spectral bandwidth (Figure 4.3d).[3] The probe beam is then directed to a second home-built pulse shaping setup using a SLM (Boulder Nonlinear Systems) in order to compensate for the dispersion of the microscope objective.

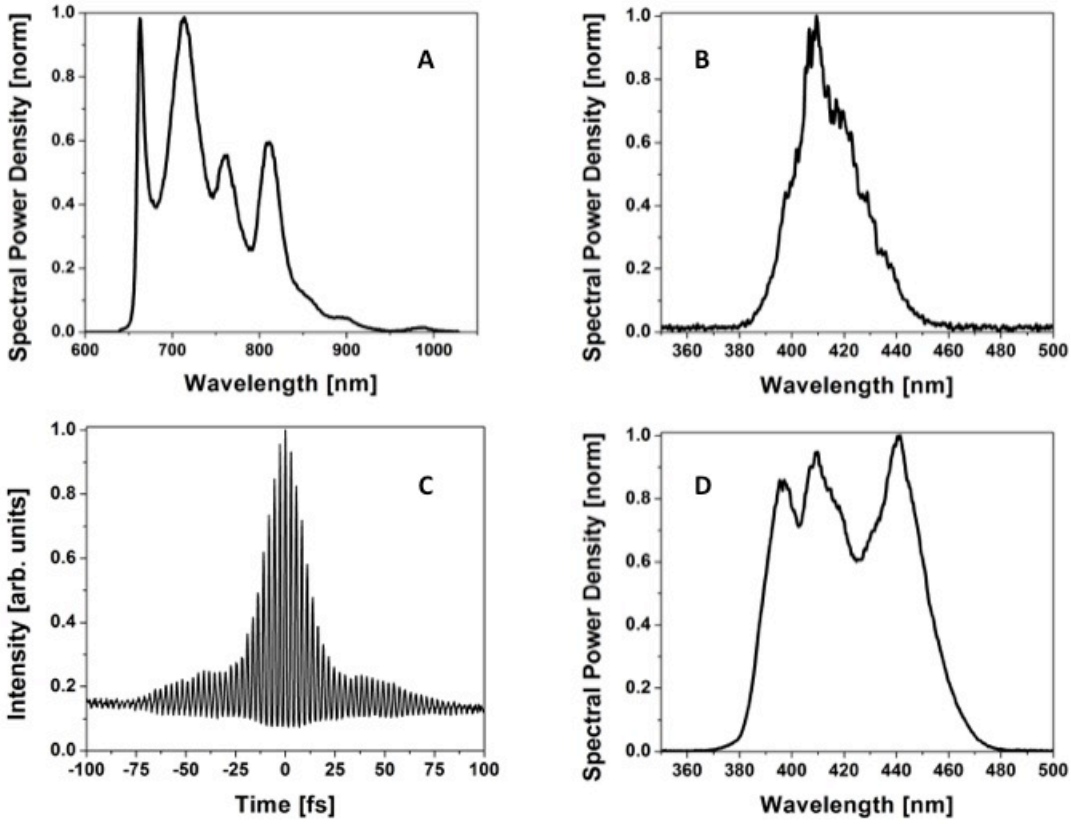

Figure 4.3 Pulse characterization. A. Venteon: Pulse one fundamental spectrum. B. SH bandwidth after microscope objective. C. Pump pulse interferometric autocorrelation. D. Probe pulse spectrum.

An automated delay stage on the pump beam controls the time delay interval between the pump and probe pulses. To ensure the smallest spot size and similar focal lengths, the beams are individually expanded using telescopes to fill the entire back aperture of the objective (Olympus 40X, NA= 0.6) before being combined with a dichroic mirror. The nonlinear interaction of the pump and probe pulses at the focus

results in transfer of pump modulation to the probe. The probe beam is then collimated with a 0.8 NA condenser and the pump light is removed with a dichroic mirror and short-pass filter combination. The modulation on the probe is detected with a balanced amplified photodiode (ThorLabs, PDB420A) and lock-in amplifier (Zurich Instruments, HF2L1). Kinetic lifetimes are obtained by scanning the delay stage. A raster-scanning XYZ piezo stage is used to create three-dimensional images.

4.3 Pulse Shaping

Pulse shaping was previously discussed in chapter 2. In this section, we discuss design elements specific to the blue pulse shaper. Figure 4.4 shows two cartoons and an image of the blue pulse shaper.

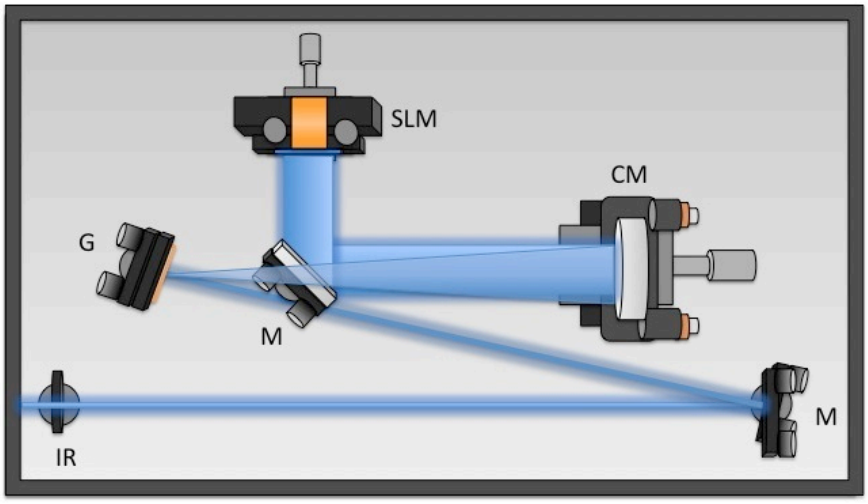

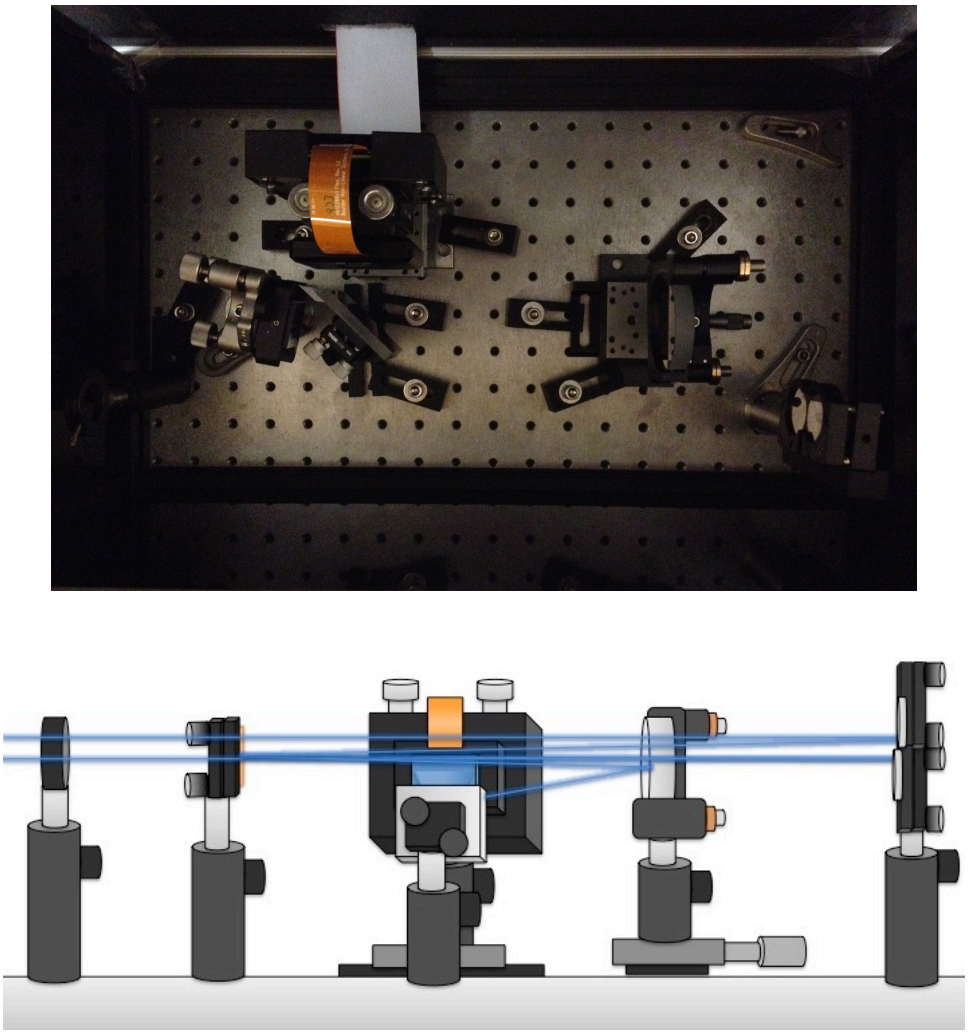

Figure 4.4 Blue pulse shaper geometry. Top: Top-down perspective of blue pulse shaper schematic, illustrating the grating (G), flat mirrors (M), curved mirror (CM), spatial light modulator (SLM), and iris (IR). Middle: Picture of blue pulse shaper from top-down perspective. Bottom: Side view perspective of blue pulse shaper schematic.

In the off Littrow configuration, where the blue beam is incident at $\alpha = 7^{\circ}$, and using a 600 groove/mm $\left(d = 1/60000\right)$ blue blazed grating (Optometrix), with a theoretical wavelength distribution of 350-500 nm we can use the relation

$$m\lambda = d\left(\sin\alpha + \sin\beta\right) \tag{4.1}$$

to find $\beta_{350} = 5.06^{\circ}$ and $\beta_{500} = 10.3^{\circ}$, giving an angular spread of $\Delta\beta \approx 5^{\circ}$. To determine the distance between the grating and collimation required in order to cover the entire 2cm SLM LCD, we use the relation

$$D = \frac{2cm \bullet 180}{\Delta\beta \bullet \pi} \tag{4.2}$$

and find $D \approx 23cm$. The SLM then needs to be properly positioned within the confocal length of the collimating mirror.

There are several other key components to keep in mind when assembling an SLM based pulse shaper. First, the SLM is analogous to an active waveplate with the extraordinary axis voltage dependent. To function properly, the polarization of the incident beam must be parallel with the extraordinary refractive index of the liquid crystals. Taken to the opposite extreme, where the polarization of the beam is perpendicular to that extraordinary refractive index, no retardance will occur. The laser beam should be kept as close to orthogonal to the face of the SLM as possible, while also ensuring the output may be spatially separated from the input. The Nyquist theorem puts an upper limit to the pulse compression capability of an SLM, where the difference in phase applied by two adjacent pixels should be smaller than π.[4] In practice this number may be smaller due to diffraction effects due to the discrete nature of the pixels. For our SLM, the diffraction efficiency (zero-order) is found to be between 80-95% depending on the applied wavelengths. Any optical aberration, wavefront distortion or spatial chirp can also greatly reduce the effectiveness of the SLM.

4.3.1 SLM Characterization

A Boulder Nonlinear Systems, Inc. (BNS) SLM is used in our blue pulse shaper. This phase only SLM is comprised of a 1x12K linear array of liquid crystals capable of modulating light according to the liquid crystal orientation. Vertically polarized light travels through the conductive glass coverslip, the liquid crystals, and is reflected off the electrode pixels. An analog voltage drives each pixel resulting in an electric field across the liquid crystals to the conductive cover glass. The optical properties of the (nematic) liquid crystals can be controlled due to their variable electro-optic response to the electric field. Different voltages at each pixel within the SLM can create an arbitrary phase mask to a high degree of accuracy. No electric field across the liquid crystals results in the liquid crystals perpendicular to the incident beam. As illustrated in figure 4.5, this orientation results in the largest difference between the extraordinary (n_e) and ordinary (n_o) refractive index with respect to the incident light beam. In our configuration, the polarization of the light is parallel with the extraordinary index of refraction of the liquid crystals resulting in the maximum phase delay. At the highest potential, the liquid crystals will orient along the electric field lines resulting in the liquid crystals being parallel with the incident beam. Relative to the incident light beam, the extraordinary index of refraction will approach that of the ordinary index of refraction. This orientation will result in minimal phase delay and as such the SLM acts most like a mirror.

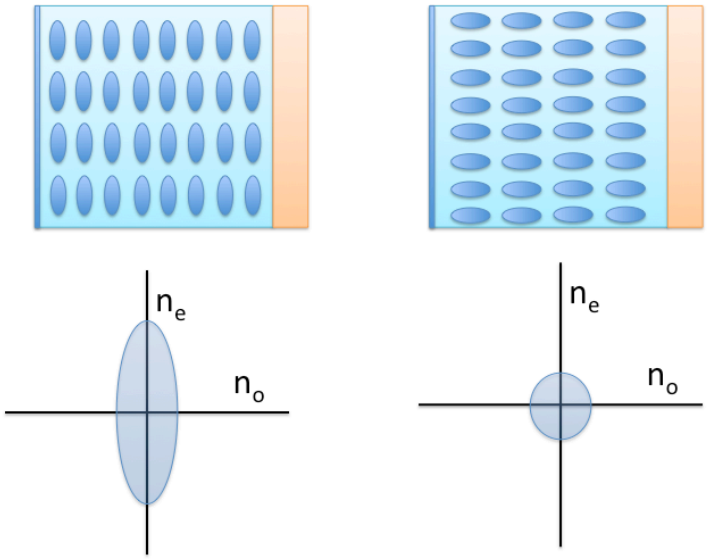

Figure 4.5 SLM liquid crystal cartoon illustrating the change in the extraordinary index of refraction with respect to liquid crystal orientation.

The BNS SLM is a 16-bit device, resulting in each pixel being capable of being independently programmed from 0 to 65535 voltage states (2^{16}). The applied voltage ranges between 0 and 5 V. According to the applied voltage ranging and the nematic liquid crystals can apply a 2π phase shift (1λ) to a beam of light. The 12,288 pixels having ~1.5um width and ~19.66mm high within the 19.66 x 19.66mm array helps mitigate issues due to over sampling (greater than 1π shift between pixels). Unfortunately, adjacent pixels suffer from cross-talk, which is measured to be approximately 8 pixels. For this reason, the SLM is operated with super-pixels (eight pixels acting as a single pixel) resulting in less spectral resolution. During operation, the liquid crystals are toggled between true voltage (+V) and the inverse voltage (-V) to mitigate permanent poling. The optical crystals do not respond differently to polarity, hence 5 V and -5 V result in the same response. When applying a phase mask to the SLM, the SLM will respond with a rise time of approximately 100 ms and a fall time of

2.5 ms. The refresh rate can be controlled with the frame rate (true frames) within a range of 1KHz and 200Hz. The liquid crystal's nonlinear response to the electric field requires full characterization. The nonlinear response is mapped to the applied voltage in a custom look-up-table (LUT file), where a linear output response of 0 to 2π can be obtained. The LUT file is comprised of two columns. The first column contains integers that range from 0-65535 so that every input value may be converted. The second column also ranges from 0-65535, but in a nonlinear fashion, as these values account for the nonlinearity of the liquid crystals. The wavelength incident on each pixel as well as the voltage required to apply a specific phase to each wavelength must be known for proper use.

4.3.2 SLM as a Variable Wave Plate

To understand how the SLM alters the phase of light it is easiest to use the physics of a waveplate as a starting point. A waveplate is made of a birefringent material, where the refractive index is different along the axes of the crystal. Two common types are half-wave plates and quarter waveplates. The half-wave plate shifts the linear polarized light into a different direction. The quarter-wave plate converts linear polarized light into circularly polarized light and back. Mathematically, this can be understood where an electric field E

$$E = E_0 \sin(\omega t - kz)\hat{x} + E_0 \cos(\omega t - kz)\hat{y} \tag{4.3}$$

propagates through a material with different index of refraction. This can be described by substituting $k = \frac{2\pi}{\lambda} nl$ into equation 5.5, resulting in

$$E = E_0 \sin\left(\omega t - \left(\frac{2\pi}{\lambda} n_o L\right) z\right)\hat{x} + E_0 \cos\left(\omega t - \left(\frac{2\pi}{\lambda} n_e L\right) z\right)\hat{y} \tag{4.4}$$

where the refractive index of the material is different for each component of the electric field. This equation is typically rewritten with respect to the ordinary index of refraction, giving

$$E = E_0 \sin\left(\omega t - \left(\frac{2\pi}{\lambda} n_o L\right) z\right)\hat{x} + E_0 \cos\left(\omega t - \left(\frac{2\pi}{\lambda} (n_e - n_o) L\right) z\right)\hat{y} \tag{4.5}$$

A quarter wave plate will have the certain length, L, for a given λ, where the n_e and n_o result in a phase shift of $\pi/2$, resulting in a linearly polarized beam of light converting into a circularly polarized light. For a half wave plate, the resulting phase shift is π, resulting in the polarization flipping.

We can now interpret the SLM as an electronically controlled variable wave plate, where an applied voltage controls the extraordinary index of refraction. The resulting induced phase onto the beam of light from the SLM can be described in complex notation as

$$E_0 e^{\frac{i2\pi}{\lambda} n_{eff}} = E_0 e^{\frac{i2\pi}{\lambda}\left[n_e \sin(\theta) + n_o \cos(\theta)\right]} \tag{4.6}$$

resulting in the effective phase of the beam as

$$\Delta\phi_{\max} = 2\pi\left(n_e - n_o\right)\frac{2d}{\lambda} \tag{4.7}$$

where the 2*d represents the distance propagated through the reflective SLM. The liquid crystals used are proprietary, but have a similar refractive index to liquid crystal MLC-6241-000. The dispersion formula for this liquid crystal is

$$\begin{aligned} n_o &= 1.4601 + 0.0054\lambda^{-2} + 3.15x10^{-17}\lambda^{-4} \\ n_e &= 1.5397 + 0.0075\lambda^{-2} + 1.03x10^{-5}\lambda^{-4} \end{aligned} \tag{4.8}$$

which gives the following figures.

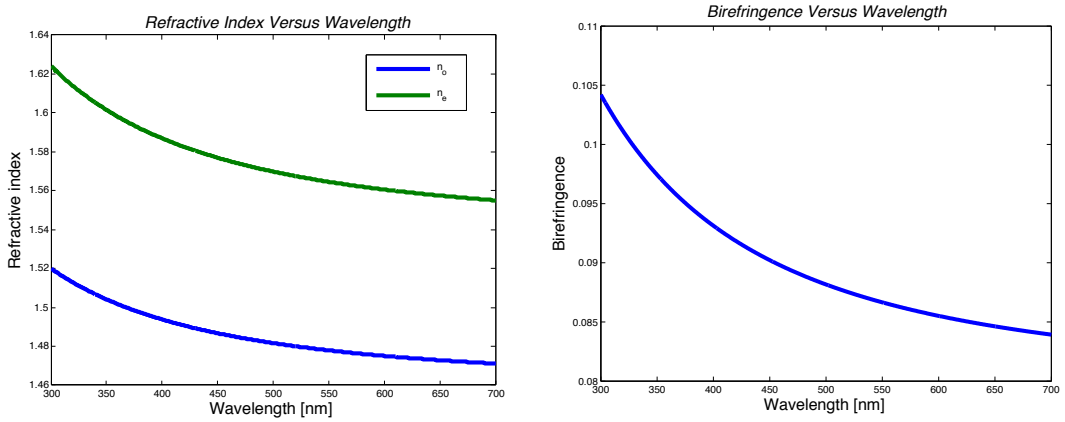

Figure 4.6 Optical properties of the SLM. Left: Refractive index of liquid crystal Right: Birefringence of liquid crystal.

Assuming the liquid crystals have a length of $5\,\mu m$, at 406 nm (n_o=1.4601, n_e=1.5397) we have an effective phase of $\Delta\phi_{\max} \approx 4\pi$.

4.3.3 Pixel-Wavelength Calibration

The first step to SLM calibration is to determine which wavelength is incident on which pixel. To determine this, the blue pulse shaper is put between two cross polarizers (figure 4.7).

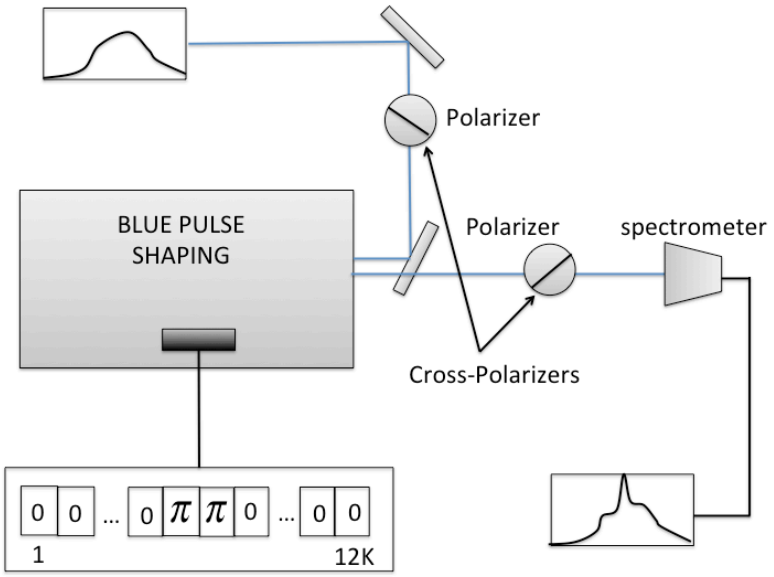

Figure 4.7 SLM geometry for pixel-wavelength calibration.

First, the linear polarized light is converted to 45 degrees at the first polarizer, as the beam propagates into the blue pulse shaping box the polarization can be altered with the SLM, the beam exits the blue pulse shaper and is discriminated with the second polarizer (cross-polarizer). If the SLM has no phase mask, then the polarization of the pulse will be orthogonal to that of the second polarizer, resulting in minimal intensity transition. Applying a phase mask of zeros with a few pixels acting as a super pixel having a π phase, the wavelengths incident on the π phase will alter the polarization of the beam resulting in some intensity after the cross-polarizer. Using a spectrometer, we can then know which wavelength are transmitted through the discriminating polarizer and obtain a wavelength to pixel calibration. The results of this method are presented in figure 4.8. A MATLAB script in conjunction with a spectrometer using LabVIEW was automated to put a π-step phase mask on the SLM and record the corresponding spectra.

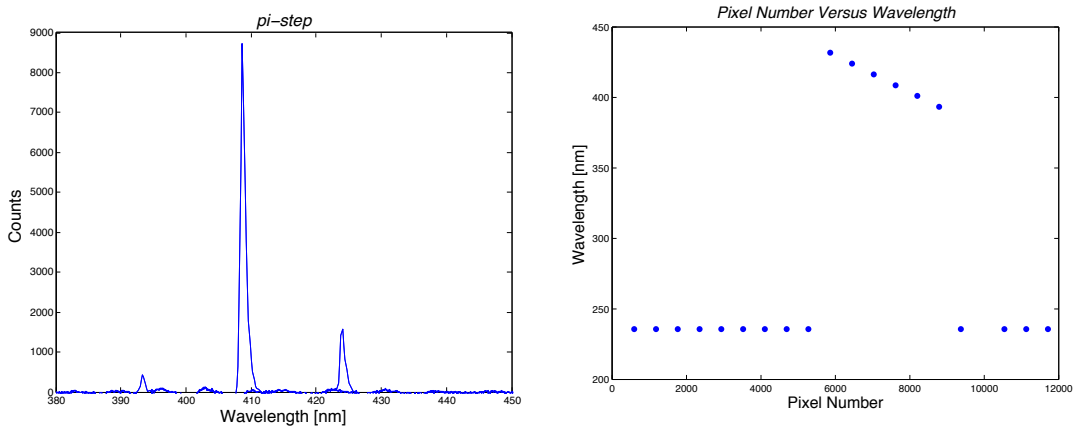

Figure 4.8 SLM pixel-wavelength calibration Left: Selected wavelengths using π-step method. Right: Peak-wavelength associated with center pixel π-step.

The points in figure 4.8 corresponding to the linear spread of wavelength onto the SLM are fit to the equation is $y = -0.0131x = 508.5$, where x is the pixel number and y is wavelength (nm). From this data, we interpolate the position of the SH wavelengths incident on the SLM. In the current configuration, wavelengths are spaced 76 pixels apart.

A second calibration is required for compensating for the birefringence of the liquid crystals at different wavelengths. Previously we simply stated the existence of a maximum and minimum intensity transition through the cross-polarizers. The actual intensity transition follows the relationship

$$I = \sin^2\left(\frac{1}{2}\bullet\left[2\pi\left(n_e - n_o\right)\frac{2d}{\lambda}\right]\right) \tag{4.9}$$

If we plot equation 4.11 versus wavelength we see the dramatic variation in the polarization of the different wavelengths (figure 4.9).

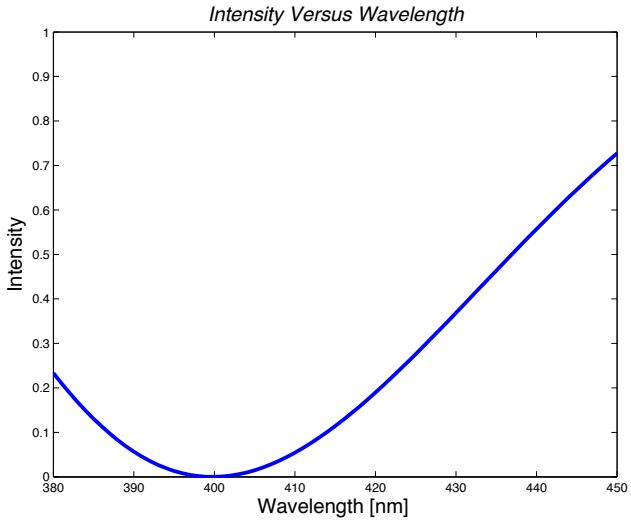

Figure 4.9 Theoretical intensity transmission through cross-polarizers at constant refractive index with respect to wavelength.

Furthermore, if we look at one wavelength (406 nm) and ramp up the voltage, we would see the following intensity profile after the cross-polarizer (figure 4.10).

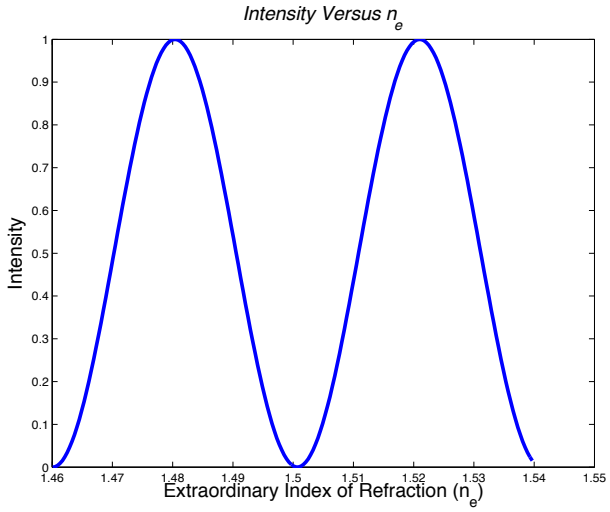

Figure 4.10 Intensity after cross-polarizer of 406 nm light with respect to the extraordinary refractive index.

Figure 4.10 shows the manifestation of the 4π phase on the intensity transmitted through the cross-polarizer. While figure 4.9 gives us an idea of refractive index calibration, we

need to determine this relationship experimentally. The next section discusses the proper procedure for the experimental refractive index calibration.

4.3.4 Refractive Index Calibration

The second calibration technique requires compensation for the index of refraction of the liquid crystals at different wavelengths. Previously, the SLM was calibrated at one wavelength (536 nm). Due to the high variability in the refractive index in the near-UV spectrum, proper calibration across our spectrum is required. The standard calibration technique for refractive index is a Twymann-Green interferometer.[5] Unfortunately, this technique iterates between individual wavelengths, making it time prohibitive.

Our technique uses the SLM in its pulse shaping 4-f geometry between two cross polarizers. A phase mask comprised of the same voltage across all pixels is ramped from 0 to 65535. With the knowledge of which wavelength is at which pixel, we can use the variation in intensity transmission through the discriminating polarizer as a measure of refractive index error. From this data we can generate a LUT file, which properly calibrates the SLM.

The voltage range 0 to 5 volts actually corresponds to 0V to 10V while a constant 5V field is held at the glass plate. Using the corresponding pixel grayscale values of 0-65535 we therefore travel from -5V to +5V. If we increase the voltage while observing one wavelength we obtain the following plot (figure 4.11).

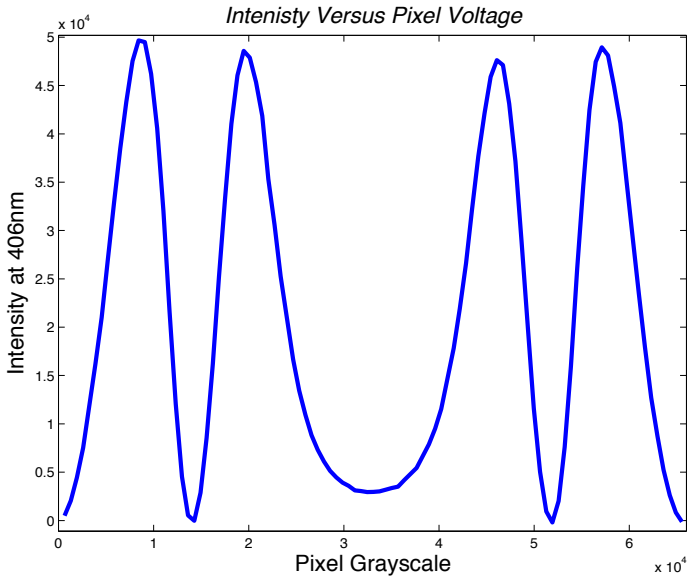

Figure 4.11 Experimental transmission of 406 nm through cross-polarizers with respect to different SLM voltages.

Figure 4.11 is different from figure 4.10 in that it has a mirror image of the 4π phase across the 5V center. At a grayscale value of 32768 (5V) the liquid crystals are in an orientation approaching $n_e = n_o$. The mirror reflection along this point corresponds to the fact that the liquid crystals are not polar and hence have equivalent responses from positive and negative voltages. Looking at grayscale values between 32768-65535 we can see that the SLM can apply an optical phase spanning $\Delta\phi_{\max} \approx 4\pi$, as was theoretically predicted earlier. The 5V potential does not give zero intensity due to the poor optical response of the liquid crystals in the $\pm 1V$ region and for this reason we operate the SLM at the highest voltage range.

Next we compare the theoretical results shown in figure 4.9 to the experimentally measured values. Proper normalization of the experimental data with respect to different intensities at each wavelength gives the transmitted intensity through the cross-polarizer

(green) in figure 4.12. Clearly, the experimental results do not perfectly match with our theoretical predictions. The experimental values are used to calibrate our system as it accounts for imperfections associated with the device.

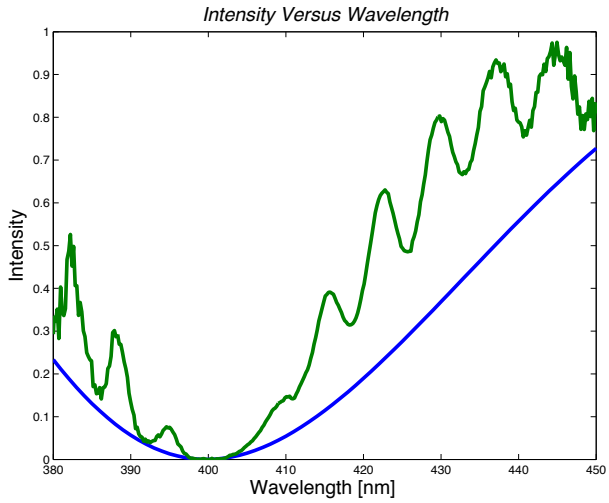

Figure 4.12 Theoretical (blue) and experimental (green) intensity transmission through cross-polarizers at constant refractive index with respect to wavelength.

4.3.5 Pulse Compression

The following describes the process of pulse compression for the SH beam. A cartoon of the sum-frequency alignment is presented in figure 4.13. The pump and probe beams are overlapped and collinear prior to the microscope enclosure. The sum-frequency generated from 800 nm and 400 nm is 266 nm, which will not transmit through our standard condenser. A 0.6 NA parabolic mirror is used in place of the condenser. Proper alignment of the beams will result in continued spatial overlap after sum-frequency, making spatial filtering impossible. A UV-low-pass-filter is used to attenuate the pump and probe beams to ~5% of their original intensity. A fused silica lens focuses the 266nm beam into the spectrometer, which is aligned to filter out the all wavelengths except $\sim 270 \pm 5nm$. We use a PMT (PMT – R1527) to detect the intensity of the sum-

frequency while lock-in detection at 1MHz improved signal to noise. With a maximum anode current of $100\mu A$ and 50Ω termination, we can only obtain a signal of 500 mV.

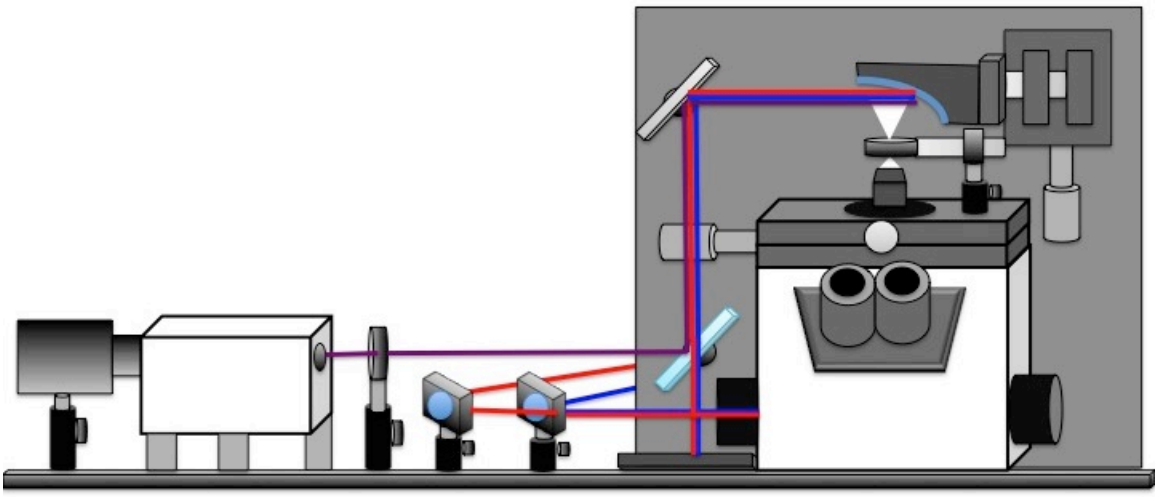

Figure 4.13 Cartoon of experimental sum-frequency setup.

Figure 4.14 illustrates the process used for obtaining a sum-frequency spectrogram. Briefly, a delay stage scans the fundamental beam with respect to the blue pulse. The resulting sum-frequency signal can be used to measure the chirp on the SH beam.

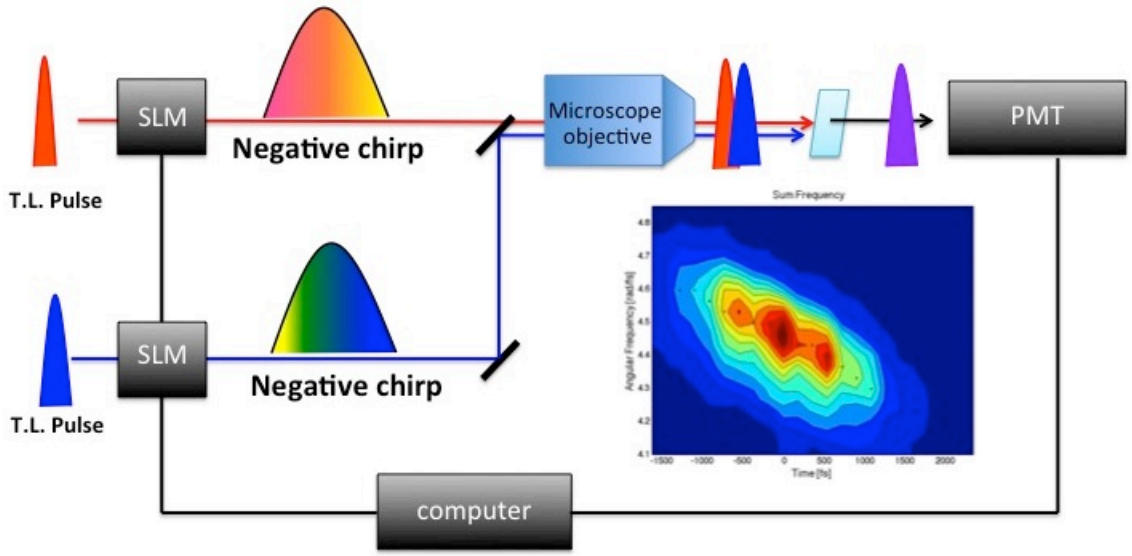

Figure 4.14 Cartoon of sum-frequency generation measurement, by mixing the fundamental beam with the second harmonic beam.

Initial attempt to compress the pulse after the microscope objective were challenging due to the large amount of dispersion. To simplify the problem, the microscope objective was replaced with a 6mm thick fused silica lens. The decrease in dispersive optics and increase in spot size and confocal length greatly simplified the procedure. Using the previously described technique, a spectrograph of the chirp for the fused silica lens can be seen in figure 4.15. Recall, the laser pulse equation in the spectral domain is given as

$$\tilde{E}(\omega) = A(\omega)e^{i\varphi(\omega)} \tag{4.10}$$

where we expanded the spectral phase in a Taylor series to give

$$\varphi(\omega) = \varphi_0^{(0)}(\omega) + \varphi_0^{(1)}(\omega-\omega_0) + \frac{1}{2}\varphi_0^{(2)}(\omega-\omega_0)^2 + \frac{1}{6}\varphi_0^{(3)}(\omega-\omega_0)^3 + \ldots + \frac{1}{n!}\varphi_0^{(n)}(\omega-\omega_0)^n$$

(4.11)

By determining maximum intensities at each time delay, a linear fit of time versus frequency gives an approximate chirp of 1878 fs^2 for the fused silica lens.

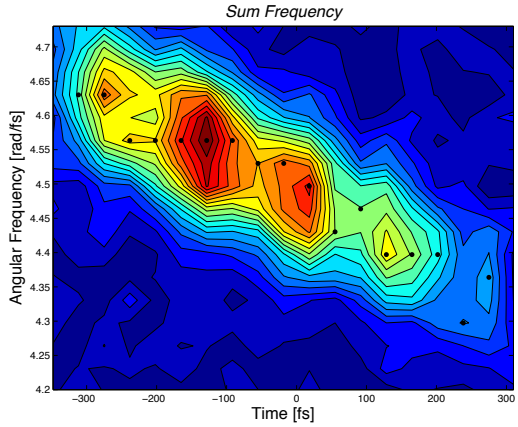

Figure 4.15 Chirp of second harmonic beam without pre-compensation after a fused silica lens. Linear fit of maximum intensities.

With an approximate chirp known, we perform a phase-mask scan across a large alpha domain. The intensity of sum-frequency increases when the pulse compresses. Figure 4.16 shows at $\alpha = -1750\, fs^2$ the greatest intensity from sum-frequency is obtained, signifying second harmonic pulse compression.

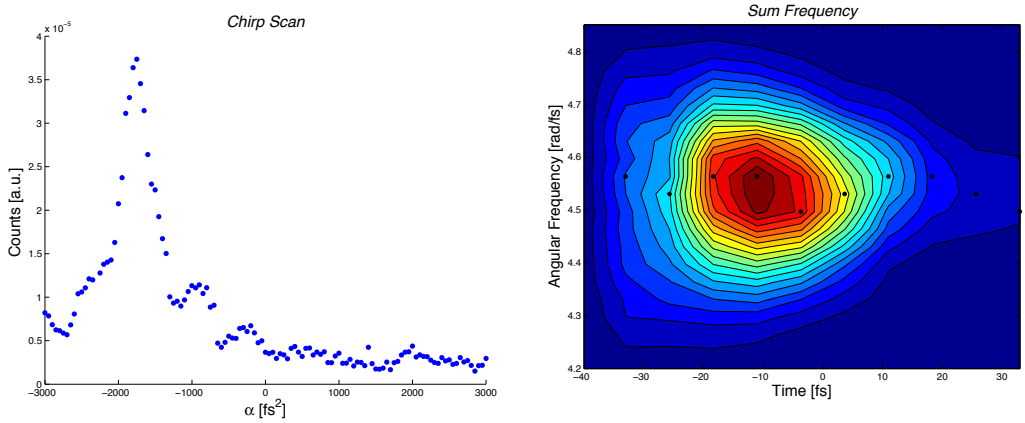

Figure 4.16 Phase mask scan giving higher intensity when the pulse is compressed for a fused silica lens. Spectrogram of pulse compression using $\alpha = -1750\, fs^2$

With pulse compression obtained with a simple fused silica lens, we applied our pulse compression technique to compensating the microscope objective. Figure 4.17 shows the spectrograph of the SH pulse chirp for the microscope objective. The linear fit gives an approximation to the blue chirp of 8200 fs^2.

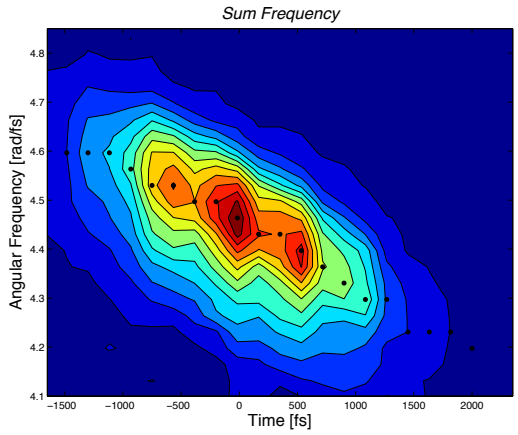

Figure 4.17 Chirp of second harmonic beam without pre-compensation. Linear fit of maximum intensities.

A phase-mask scan across the even larger alpha domain was then performed. An alpha value of approximately -7000 fs^2 was found to obtain the greatest sum-frequency signal (figure 4.18). Using this value for the quadratic phase mask, the SH pulse was compressed to approximately 30 fs (FWHM).

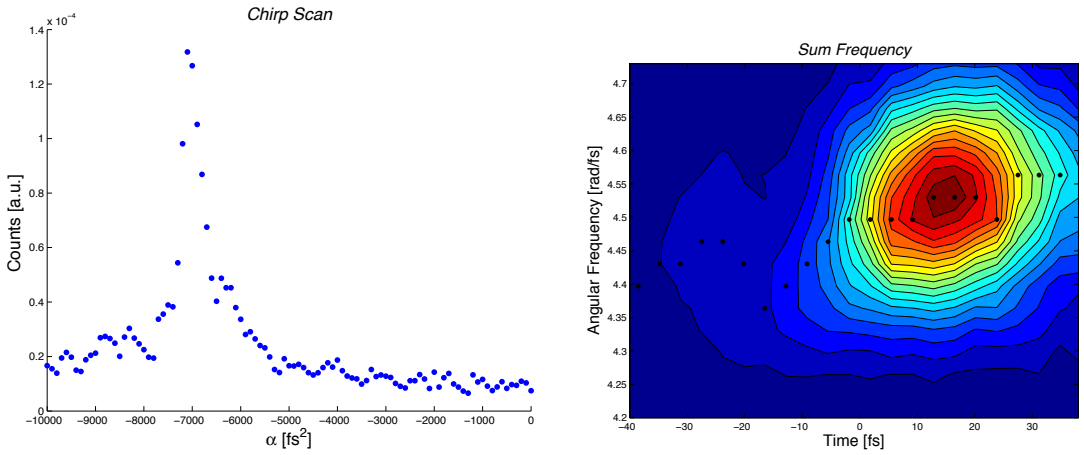

Figure 4.18 Microscope objective SH pulse compensation. Left: Quadratic phase scan. Right: Compressed SH pulse.

4.4 Signal to Noise Optimization

Pump-probe imaging requires sufficient signal to noise ratios to obtain high contrast images. In the collinear geometry, the signal strength can be expressed as:

$$S \propto [c] \cdot \sigma_{molecule} \cdot I_{pump} \cdot I_{probe} \tag{4.12}$$

where S is the signal strength, c is the concentration of the sample, σ is the molecular cross section, and I is the intensity of the pump and probe beam. Unfortunately, material sensitivity and noise intrinsic to the experiment preclude simply increasing the pump-probe intensities. An inherent noise in our system is 1/f noise, which is aptly named as such because the noise decreases with increasing frequency, according to the relation of 1/f (figure 4.19). While the origin of 1/f noise is largely unknown, there are various methods in its attenuation.[6,7]

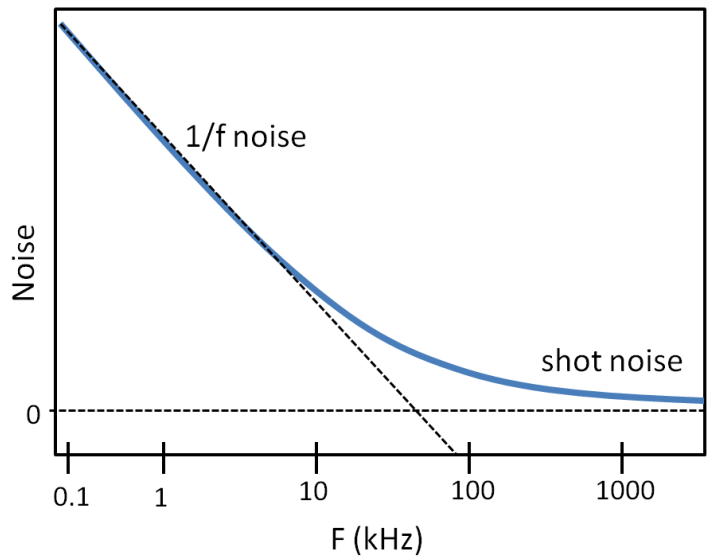

Figure 4.19 Schematic of laser noise as a function of frequency.

To increase signal to noise, we use an electro-optic modulator to modulate our pump beam (figure 4.20). Our experiments require high modulation (1MHz) so we use a Conoptics model 350-160 KD*P series modulator. In essence, an electro-optic modulator is a pockel cell that acts as a linearly dependent voltage-variable waveplate. When unpolarized light transmits through a Pockel cell parallel to the crystal's optical axis, and when no electric field is applied, the light remains unchanged. When an electric field is applied across the crystal, anisotropic changes in the refractive index of the crystal cause birefringence and result in two linearly polarized beams of light (ordinary and extraordinary), which become displaced in space and time. In our case, the beam is initially horizontally polarized propagating orthogonal to the optical axis. When an electric field is applied in this configuration, the resulting ordinary and extraordinary components travel at different speeds but do not split apart. The change in the refractive index causes a phase shift, which allows for conversion between linear, circular, and elliptical polarization. Included within the Conoptics modulator is an output polarizer,

which converts the polarization modulation by the Pockel cell to an amplitude modulation by throwing out the orthogonal polarization. Using a high frequency source, the Conoptic modulator is capable of modulating a signal in the MHz region. This results in our mode locked pulse train being chosen selectively by a square wave modulation.

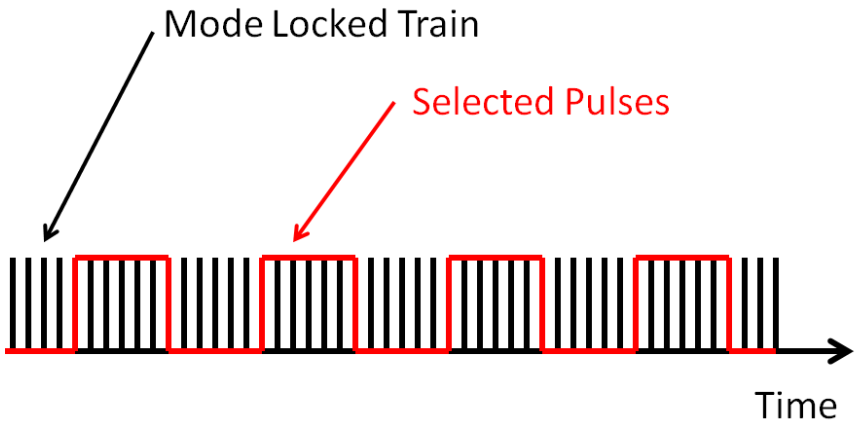

Figure 4.20 Schematic of square wave modulation of mode locked pulse train from Ti:Sapphire laser.

The modulation of our pump is transferred to the probe, which is detected with a detector. The signal from the detector is transmitted to a lock-in amplifier, making the detection scheme phase sensitive. At high modulation frequencies, the technique is capable of extracting weak signals with a known phase from a noisy environment. In our experiments we use a Heliotis HF2 lock-in amplifier, which acts as our frequency source and reference. The lock-in effectively performs a Fourier transform on the signal $f(t)$ by selecting the frequency component (ω_s) of interest from our signal and then averaging over an infinite amount of time.

$$F(\omega_s) = \int_{-\infty}^{\infty} f(t) e^{-i\omega_s t} dt \tag{4.13}$$

More specifically, as in our case, we want to determine the amplitude (A_s) and phase (φ_s) of our input signal so as to distinguish it from the noisy background. Where our signal is defined by

$$V_s = A_s \cos(\omega_s t + \varphi_s) \tag{4.14}$$

The resulting *in-phase* (V_x) and *quadrature* (V_y) outputs are

$$\begin{aligned} V_x &= \left\langle \mathrm{Re}\left\{ V_{signal}(t) 2e^{-i\omega t} \right\} \right\rangle = A_s \cos(\varphi) \\ V_y &= \left\langle \mathrm{Im}\left\{ V_{signal}(t) 2e^{-i\omega t} \right\} \right\rangle = -A_s \sin(\varphi) \end{aligned} \tag{4.15}$$

The signal can be converted to amplitude V_R and phase Φ with the relationship

$$\begin{aligned} V_R &= \left(V_x^2 + V_y^2\right)^{1/2} \\ \Phi &= \tan^{-1}\left(V_x / V_y\right) \end{aligned} \tag{4.16}$$

From this point forward, amplitude refers to V_R and the phase of the signal refers to Φ. The combined measurement of amplitude and phase allows us to distinguish ground state bleach and excited state absorption in our pump-probe experiments.

4.5 Endogenous Subcellular Contrast of Red Blood Cells

RBC function is enabled by its high concentration of hemoglobin. Hemoglobin is composed of four protein subunits, with each protein subunit containing a protoporphyrin IX macrocycle with an iron atom in its center (Figure 4.21).[8] The unique electronic properties of the heme structure enable the binding and transport of oxygen by the hemoglobin in RBCs from the lungs to various parts of the body. With a diameter of approximately $8\mu m$ and thickness of $2.5\mu m$, RBCs are an ideal model system for demonstrating new heme protein imaging techniques. Successful imaging of RBCs using

sub-cellular contrast agents may lead to early diagnostics for angiogenesis or blood related diseases.[9],[10]

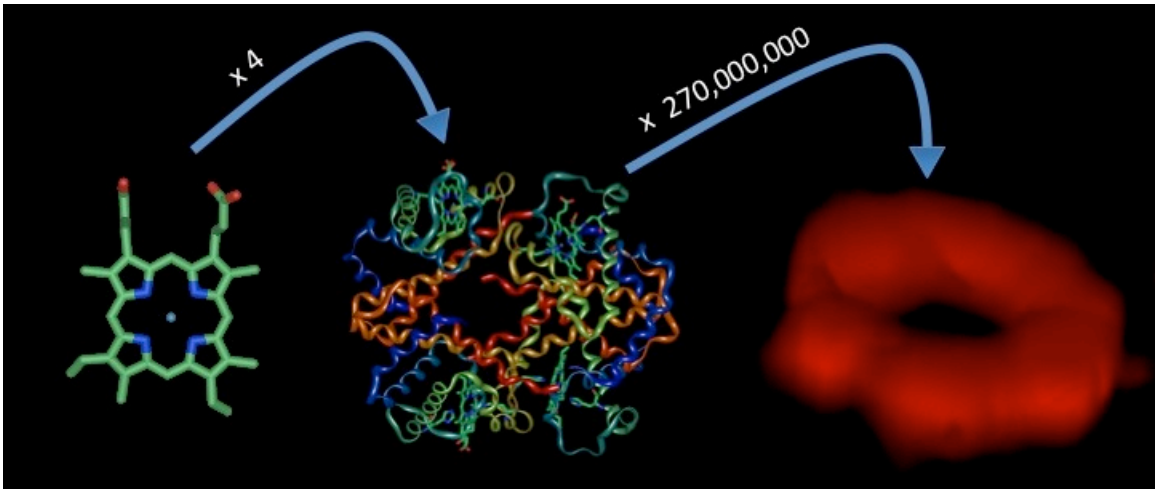

Figure 4.21 Left: Crystal structure of heme (HEM). Middle: Crystal structure of hemoglobin (1A3N), containing four hemes.[11] Right: A red blood cell imaged via our pump-probe microscopy.

The complex electronic structure of hemoglobin gives rise to numerous kinetic pathways for energy redistribution. Hemoglobin has negligible fluorescence, thus restricting studies to non-radiative channels. Absorption spectroscopy[12], transient absorption spectroscopy[13-16], Raman spectroscopy[17,18], and transient grating techniques[19,20], as well as computational studies[21,22], have all contributed to current understanding of the electronic structure and dynamics of heme proteins. The absorption spectrum of hemoglobin is shown in Figure 4.22. The Soret band is the dominant transition (~400 nm), while the Q-band (475 - 650 nm) is comprised of a broad set of transitions with smaller extinction coefficients. Further transitions extend into the near-IR region. The majority of transitions are due to $\pi \rightarrow \pi^*$ transitions of the porphyrin, while the near-IR transitions are due to porphyrin $\leftrightarrow$ iron charge transfer transitions and $d \rightarrow d^*$ transitions from the iron atom.[12-14] Ligand association not only shifts these

spectral bands, but adds and removes electronic transitions throughout the visible and near-IR spectrum.[12] In heme proteins, two-photon transitions can populate the Soret band via virtual intermediate states. The two-photon cross-section in the near-IR has been reported to be up to 150 GM at 825 nm.[23,24]

Nonlinear imaging requires multiphoton interactions mediated by a material's nonlinear susceptibility. With both one and two-photon absorptions in the near-IR, pump-probe microscopy of heme proteins has signal contributions from a number of different mechanisms. The Warren group has performed pump-probe studies employing visible (650 nm) and near-IR wavelengths, leading to endogenous contrast based on sequential two-photon absorption (excited state absorption).[25,26] Imaging of RBCs via two-photon transition to the Soret band and stimulated emission from the Q-band have been reported by the Xie group.[27] Here we perform pump-probe microscopy of heme proteins with broadband near- IR pump excitation followed by probing with higher frequency light resonant with the Soret band.

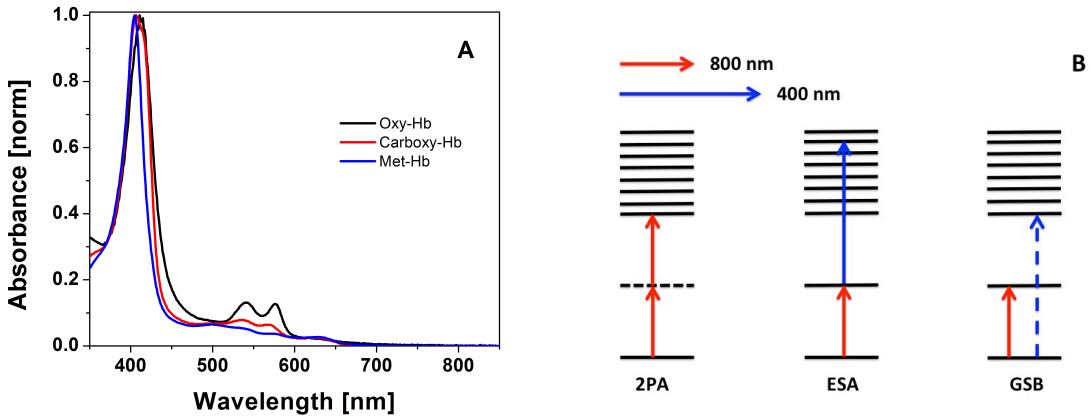

Figure 4.22 A. Steady state absorption spectra of hemoglobin. B: Processes leading to pump-probe microscopy signal in heme proteins: 2PA: two photon absorption,

mediated by virtual intermediate state, ESA: excited-state absorption, GSB: ground-state bleach.

Coumarin1 was used as a standard, as it has a well known two-photon cross-section in the near-IR and no one-photon transition in that region. The standard was excited with the entire fundamental pump bandwidth, modulated at 1 MHz and fluorescence emission was detected with a single channel of a balanced amplified photodiode (PDB440A, Thorlabs). Figure 4.23a shows a clear second order intensity dependence on the pump power, signifying a two-photon transition. As a precursor to studying RBCs, intensity measurements of met-Hb were performed. To detect absorption in met-Hb, intensity measurements require the probe pulse to interact with excited hemoglobin. Excited state absorption (ESA) and ground state bleach (GSB) are detected by 1 MHz modulation transferred to the probe beam. The pump-power dependence shown in Figure 4.23b indicates a dominant one-photon process with saturation appearing at ~20 mW average power. Amplitude shaping to selectively excite the peak 2PA transition exhibited a similar linear dependence (~40 nm bandwidth pump, centered at 825 nm). The results suggest one-photon absorption to band III and IV make up the primary absorption process under our imaging conditions.[12]

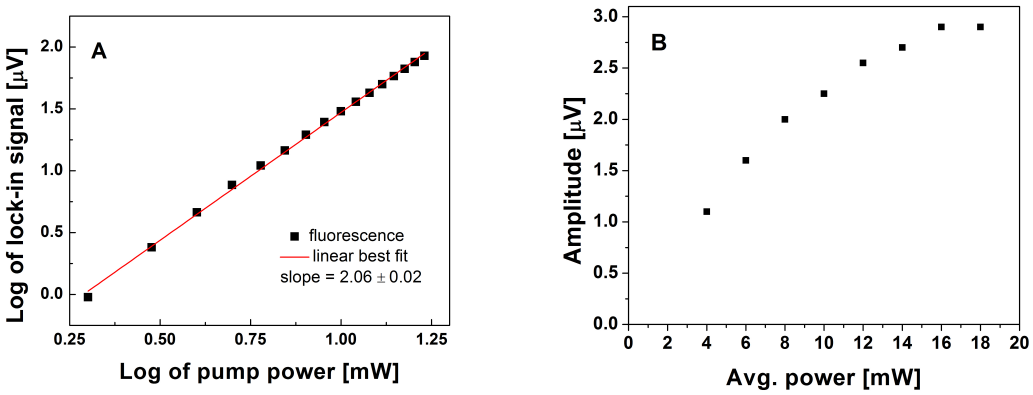

Figure 4.23 A. Two-photon intensity measurement of coumarin 1. B. One-photon intensity measurement of Met-Hemoglobin with 420 – 450 nm probe bandwidth.

Transient absorption measurements were carried out to determine kinetic pathways for both met-hemoglobin and oxy-hemoglobin solutions. Met-hemoglobin was found to have a GSB and an ESA pathway (figure 4.24). The lifetime of these pathways was found to be $539 \pm 25\,fs$ and $4860 \pm 1070\,fs$ respectfully. The interference feature in the ESA pathway is due to an orthogonally polarized portion of the probe. The orthogonal polarization inhibits compression and results in interference at each wavelength of the highly chirped beam (hence the diagonal interference line).

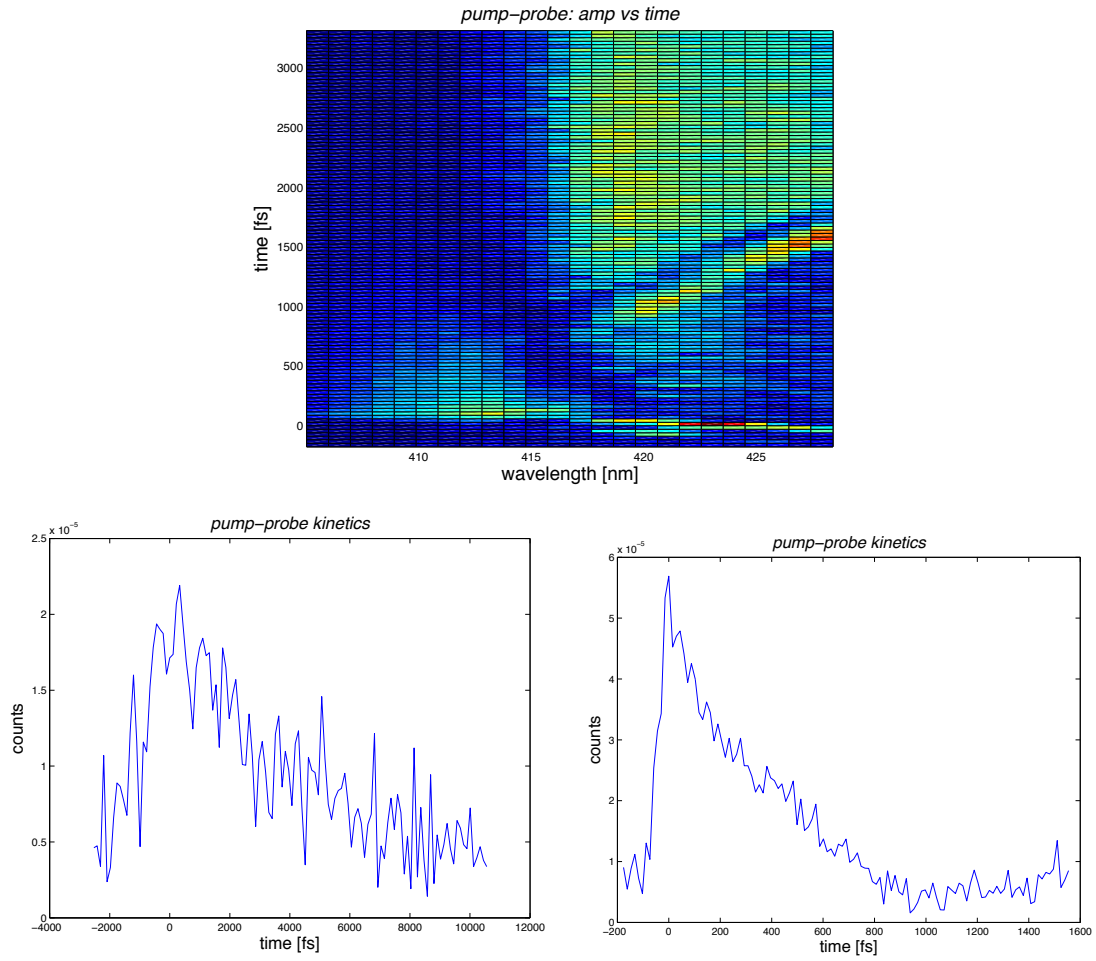

Figure 4.24 Met-Hemoglobin kinetics.

Oxy-hemoglobin was found to have only a GSB feature similar to that of met-hemoglobin (figure 4.25). The lifetime of the GSB was found to be $749 \pm 59\, fs$.

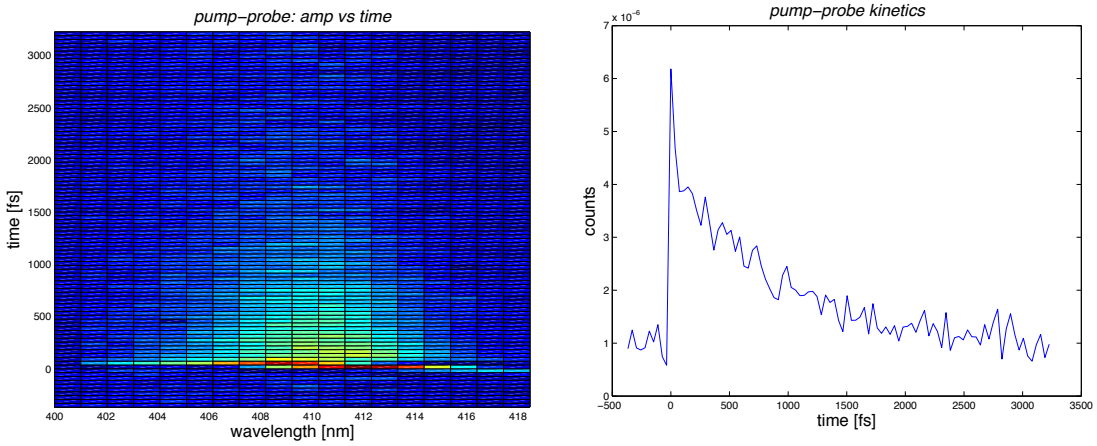

Figure 4.25 Oxy-Hemoglobin kinetics.

In Vitro images of RBCs were taken as a precursor to future in vivo studies. In vivo images of arterioles and venules have previously been distinguished by ESA signals, corresponding to oxy-Hb and deoxy-Hb, by the Warren group.[25,26] Our studies were carried out with blood smears after 24 hours of atmosphere exposure. Pump-probe measurements were then raster scanned with 0.5 μm steps across a 20x20 μm area with probe bandwidth of 380 - 450 nm (figure 4.26).

Lock-in detection identifies an amplitude and phase associated with the signal. Recently phasor analysis has been used to distinguish molecular species in pump-probe imaging.[28] Here we use phase to discriminate increasing and decreasing photon flux, corresponding to GSB and ESA. The phase was calibrated with Coumarin1. Signals from RBCs were found to correspond with previous transient absorption measurements of heme proteins, with GSB in the 380 – 420 nm and ESA in the 420 - 450 nm spectral regions.[13] The amplitude and associated phase of the signal are shown in figure 4.26. The GSB pathway has a positive phase (yellow) and the ESA pathway has a negative phase (red). The pump power was approximately 6 mW and the probe power was 130

μW at the sample. The ESA signal is weaker than the GSB signal in part due to lower power in the probe's 420 - 450 nm spectral region at the time of the study.

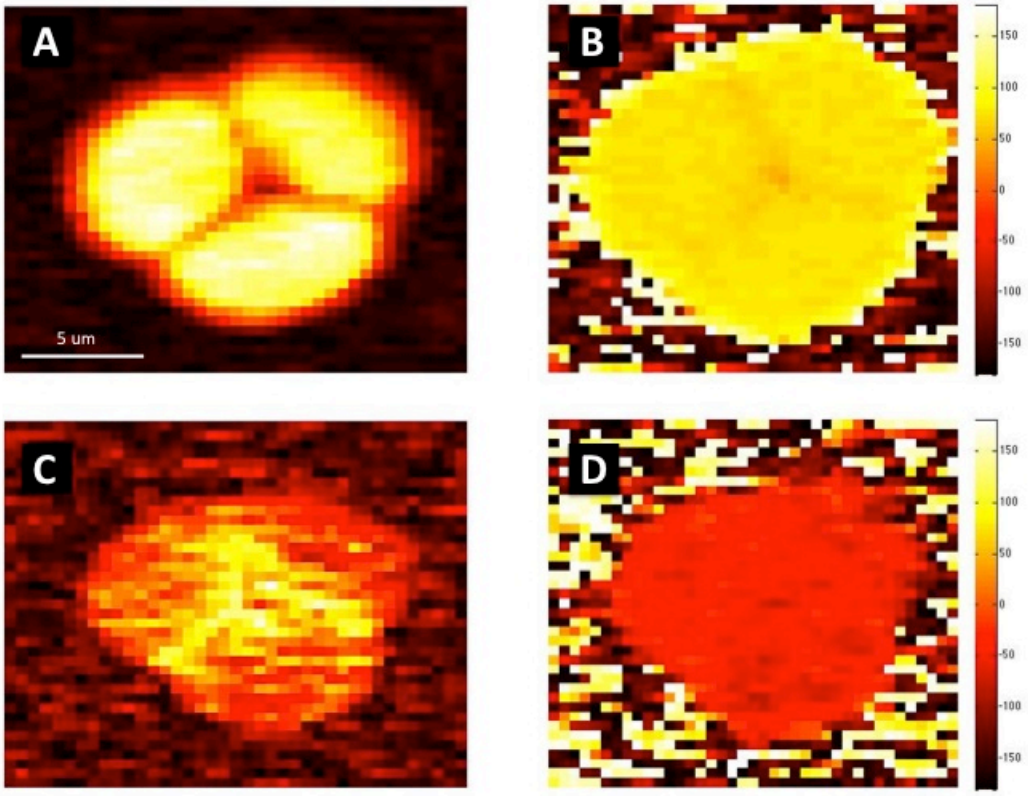

Figure 4.26 Image of three red blood cells. A. Amplitude signal of GSB, recorded with a 380 – 420 nm probe. B. Corresponding phase signal of GSB. C. Amplitude signal of ESA, recorded with a 420 – 450 nm probe. D. Corresponding phase signal of ESA.

Low modulation frequency (≤ 1 MHz) result in lifetime kinetics dominated by a time independent signal (lifetime > 200 ps). Lock-in detection identified only one phase within the full probe bandwidth (380 - 470 nm). The increased kinetic lifetime and single phase suggests a diffusion-based mechanism likely stemming from ligand dissociation/rebinding or thermal lensing. Decreasing modulation further increased the

signal to noise ratio of this signal. Photothermal lens microscopy of RBCs by the Xie group has been previously demonstrated.[29] Their experiment, using 830 nm excitation, accesses a two-photon transition to the Soret band followed by non-radiative relaxation that is detected via a 785 nm continuous wave probe. Figure 7 is an image set obtained by raster scanning a 20x20 μm area with 0.5 μm step size using 380 – 425 nm probe bandwidth at 1 MHz modulation. Determining the mechanism of this signal is an active area of investigation.

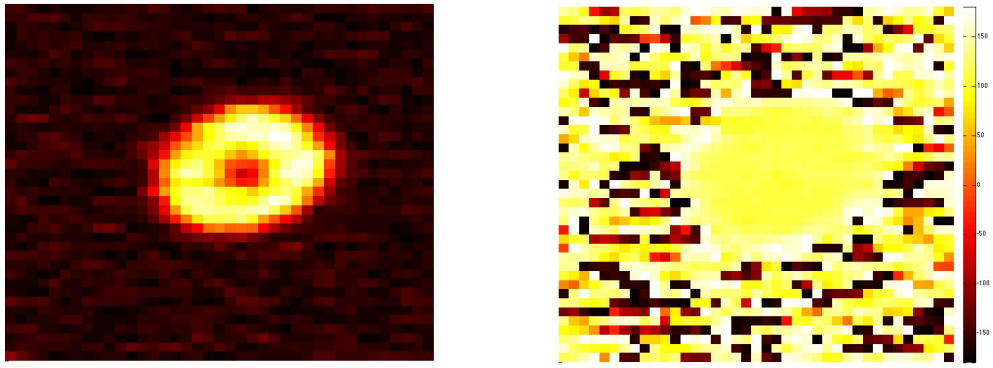

Figure 4.27 Red blood cell image. A. Amplitude of lock-in signal. B. Corresponding phase signal. Similar amplitude and phase images were obtained at different probe wavelengths and delay time intervals, suggesting ligand dissociation/rebinding or thermal lensing as the signal source.

The long-lived signal observed at low modulation frequency is a nonlinear process, depending on both pump and probe pulses. This imaging modality shows promise in obtaining high-resolution three-dimensional images of RBCs. Four pump-probe images were taken consecutively with $0.5\mu m$ steps in the z-axis to demonstrate the axial resolution (Figure 8). ImageJ and Matlab were used to filter noise, remove background and stack images into a 3-dimensional structure.

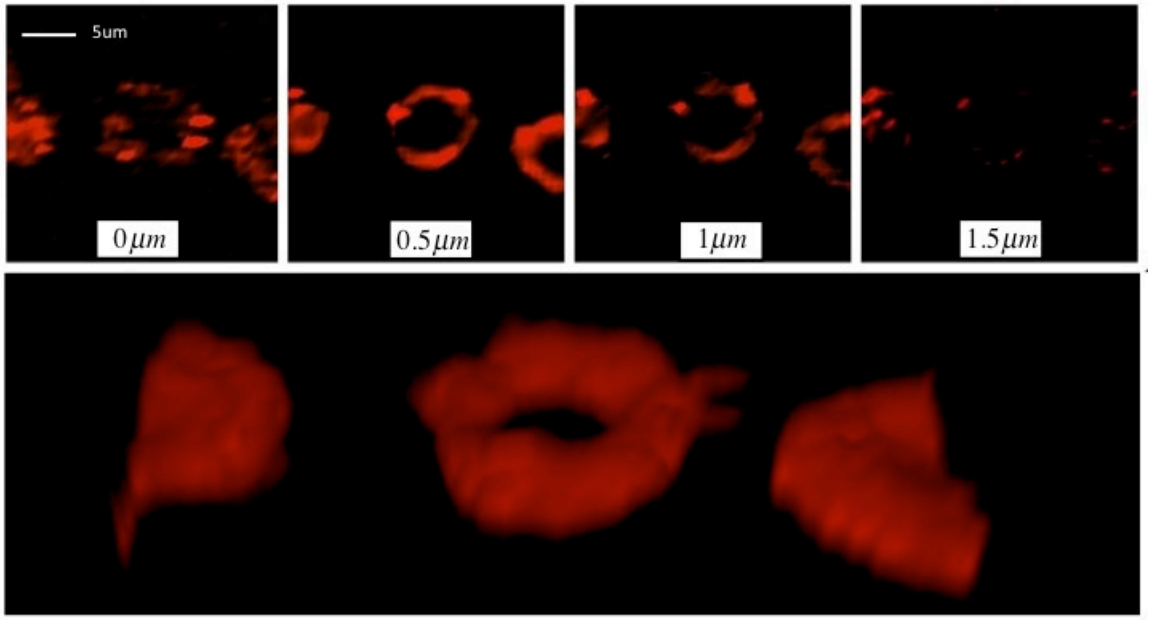

Figure 4.28 Z-stack of RBC pump-probe signal and resulting 3-dimensional image.

4.6 Conclusions

We have demonstrated a multi-color pump-probe imaging technique capable of obtaining high contrast images from the electronic pathways innate to heme proteins. Pulse-shaped broadband excitation provides access to one-photon and two-photon transitions. While short pulse durations give high probability of multiphoton transitions in molecules with large two-photon cross-sections, one-photon transitions into band III and IV appear to dominate the absorption process over the 650 – 1050 nm wavelength range under our imaging conditions. At high modulation frequencies (>1 MHz) we observe both GSB and ESA signals from heme proteins. At lower modulation frequencies (<1 MHz), a long-lived signal overwhelmed the excited state dynamics and is attributed to the ligand dissociation/rebinding or thermal lensing. This signal results in

high signal-to-noise images, giving rise to another endogenous contrast modality. Future studies will focus on pulse-shapes optimized for selected electronic pathways to enhance contrast and chemical selectivity.

References:

[1] Walowicz, K.A., Pastirk, I., Lozovoy, V.V., and Dantus, M., "Multiphoton intrapulse interference. 1. Control of multiphoton processes in condensed phases," Journal of Physical Chemistry A 106(41), 9369–9373 (2002).

[2] Lozovoy, V.V., Pastirk, I., Walowicz, K.A., and Dantus, M., "Multiphoton intrapulse interference. II. Control of two- and three-photon laser induced fluorescence with shaped pulses," Journal of Chemical Physics 118(7), 3187–3196 (2003).

[3] Furbach, A., Le, T., Spielmann, C., and Krausz, F., "Generation of 8-fs pulses at 390 nm," Applied Physics B 70(S1), S37–S40 (2000).

[4] Stobrawa, G., Hacker, M., Feurer, T., Zeidler, D., Motzkus, M., and Reichel, F., "A new high-resolution femtosecond pulse shaper," Applied Physics B 72(5), 627–630 (2001).

[5] Roopashree, M.B., Vyas, A., Banyal, R.K., and Prasad, B.R., "Phase characteristics of reflecting and transmitting type twisted nematic spatial light modulators," in arXiv physics.optics (2009).

[6] Min, W., Freudiger, C.W., Lu, S., and Xie, X.S., "Coherent Nonlinear Optical Imaging: Beyond Fluorescence Microscopy," Annual review of physical chemistry 62(1), 507–530 (2011).

[7] Scott, R.P., Langrock, C., and Kolner, B.H., "High-dynamic-range laser amplitude and phase noise measurement techniques," Ieee Journal of Selected Topics in Quantum Electronics 7(4), 641–655 (2001).

[8] Rappaz, B., Barbul, A., Emery, Y., Korenstein, R., Depeursinge, C., Magistretti, P.J., and Marquet, P., "Comparative study of human erythrocytes by digital holographic microscopy, confocal microscopy, and impedance volume analyzer," Cytometry Part A 73A(10), 895–903 (2008).

[9] McDonald, D.M., and Choyke, P.L., "Imaging of angiogenesis: from microscope to clinic," Nature Medicine 9(6), 713–725 (2003).

[10] Kleinfeld, D., Mitra, P.P., Helmchen, F., and Denk, W., "Fluctuations and stimulus-induced changes in blood flow observed in individual capillaries in layers 2 through 4 of rat neocortex," Proceedings of the National Academy of Sciences 95(26), 15741–15746 (1998).

[11] Tame, J., and Vallone, B., "The structures of deoxy human haemoglobin and the mutant Hb Tyr42His at 120 K," ACTA CRYSTALLOGRAPHICA SECTION D-BIOLOGICAL CRYSTALLOGRAPHY 56, 805–811 (2011).

[12] Eaton, W.A., Hanson, L.K., Stephens, P.J., Sutherland, J.C., and Dunn, J., "Optical spectra of oxy-and deoxyhemoglobin," Journal of the American Chemical Society 100(16), 4991–5003 (1978).

[13] Ye, X., Demidov, A., and Champion, P.M., "Measurements of the Photodissociation Quantum Yields of MbNO and MbO 2and the Vibrational Relaxation of the Six-Coordinate Heme Species," Journal of the American

Chemical Society 124(20), 5914–5924 (2002).
[14] Ishizaka, S., Wada, T., and Kitamura, N., "Femtosecond transient absorption study on relaxation intermediates in oxymyoglobin," Photochemical & Photobiological Sciences 8(4), 562–566 (2009).
[15] Petrich, J.W., Poyart, C., and Martin, J.L., "Photophysics and reactivity of heme proteins: a femtosecond absorption study of hemoglobin, myoglobin, and protoheme," Biochemistry 27(11), 4049–4060 (1988).
[16] Franzen, S., Kiger, L., Poyart, C., and Martin, J.-L., "Heme Photolysis Occurs by Ultrafast Excited State Metal-to-Ring Charge Transfer," Biophysical Journal 80(5), 2372–2385 (2001).
[17] Challa, J.R., Gunaratne, T.C., and Simpson, M.C., "State Preparation and Excited Electronic and Vibrational Behavior in Hemes †," Journal of Physical Chemistry B 110(40), 19956–19965 (2006).
[18] Koyama, M., Neya, S., and Mizutani, Y., "Role of heme propionates of myoglobin in vibrational energy relaxation," Chemical Physics Letters 430(4-6), 404–408 (2006).
[19] Miller, R.J.D., "Vibrational energy relaxation and structural dynamics of heme proteins," Annual review of physical chemistry 42(1), 581–614 (1991).
[20] MIYATA, R., and TERAZIMA, M., "Transient thermal expansion of a protein in solution after photo-excitation of the chromophore: Deoxymyoglobin," Bulletin of the Chemical Society of Japan 76(9), 1707–1712 (2003).
[21] Sagnella, D.E., Straub, J.E., and Thirumalai, D., "Time scales and pathways for kinetic energy relaxation in solvated proteins: Application to carbonmonoxy myoglobin," Journal of Chemical Physics 113(17), 7702–7711 (2000).
[22] Henry, E.R., Eaton, W.A., and Hochstrasser, R.M., "Molecular dynamics simulations of cooling in laser-excited heme proteins," Proceedings of the … (1986).
[23] Clay, G.O., Millard, A.C., Schaffer, C.B., Aus-der-Au, J., Tsai, P.S., Squier, J.A., and Kleinfeld, D., "Spectroscopy of third-harmonic generation: evidence for resonances in model compounds and ligated hemoglobin," JOSA B 23(5), 932–950 (2006).
[24] Clay, G.O., Schaffer, C.B., and Kleinfeld, D., "Large two-photon absorptivity of hemoglobin in the infrared range of 780–880 nm," Journal of Chemical Physics 126(2), 025102–025102–4 (2007).
[25] Fu, D., Ye, T., Matthews, T.E., Yurtsever, G., and Warren, W.S., "Two-color, two-photon, and excited-state absorption microscopy," Journal of Biomedical Optics 12(5), 054004 (2007).
[26] Fu, D., Matthews, T.E., Ye, T., Piletic, I.R., and Warren, W.S., "Label-free in vivo optical imaging of microvasculature and oxygenation level," Journal of Biomedical Optics 13(4), 040503 (2008).
[27] Min, W., Lu, S., Chong, S., Roy, R., Holtom, G.R., and Xie, X.S., "Imaging chromophores with undetectable fluorescence by stimulated emission microscopy," Nature 461(7267), 1105–1109 (2009).
[28] Robles, F.E., Wilson, J.W., Fischer, M.C., and Warren, W.S., "Phasor

analysis for nonlinear pump-probe microscopy," Optics Express 20(15), 17082–17092 (2012).

[29] Lu, S., Min, W., Chong, S., Holtom, G.R., and Xie, X.S., "Label-free imaging of heme proteins with two-photon excited photothermal lens microscopy," Applied Physics Letters 96(11), 113701 (2010).

Chapter 5 Synthesis and Optical Properties of Two-Photon Absorbing GFP-type Probes

5.1 Introduction

Two-photon active green fluorescent protein-type chromophores were successfully synthesized following investigations directed toward a modified version of zFP538 chromophore, a structural analogue to the GFP-chromophore. A generalized approach for the chromophore synthesis via a well-studied cycloaddition reaction combining an iminoglycine methyl ester and a substituted benzaldehyde was developed allowing for flexibility in the incorporation of functional groups such as donor-acceptor substituents and for additional groups to provide extended conjugation. Steady-state spectroscopy, fluorescence quantum yields, and time-resolved fluorescence lifetimes for synthesized chromophores were extensively investigated for the functionalized chromophores. Time-resolved fluorescence lifetimes were found to be biexponential generally with subpicosecond and picosecond components. The individual effects of substitution position of functional groups and relative bulk size were evaluated and found to be rather significant in changing the fluorescence- decay characteristics in the case of positioning, but ambiguous with respect to relative bulk. The GFP-type chromophores were found to possess modest to low two-photon absorption cross sections with the dimethylamino-substituted analogue possessing the largest value at nearly 40

GM. These molecules show promise as biological markers for application in the study of conformation changes and aggregation of amyloid peptides, known to play an important role in many neurodegenerative diseases.

5.2 Background

The green fluorescent protein (GFP)[1-3] is one of the most widely used tools in biomedical studies and has long fascinated researchers with its naturally occurring high fluorescence quantum yield. Because of their unique fluorescence characteristics, GFP and structurally analogous proteins[4] have been utilized in many research applications including protein-dynamics studies, real-time molecular and cellular analysis,[5] and a variety of imaging applications.[5] In the past few decades, the chemical structures of the fluorescently active chromophore of GFP[7,8] as well as several of its homologues[9] have been discovered, and researchers have begun to synthetically model the chromophore outside of the protein environment. Niwa *et al.*[10] were first to synthesize a model compound of the GFP-chromophore in 1996, and computational studies[11] quickly began to examine the photophysical mechanism of the chromophore when it was isolated in solution.

Ultrafast laser spectroscopy has increasingly been used as a tool to develop better theories to describe the fast electronic processes occurring in this system[12] and to understand how the tertiary protein structure contributes to the overall photophysics of GFP. Much of the significant research in this area has been based on the early discovery of a tremendous discrepancy between the fluorescence quantum yield of the chromophore in solution ($\sim 10^{-3}$) and that of the intact GFP (~ 0.8). The reason for such a dramatic

difference has long been thought to be the result of increased bond-rotation effects such as Z-E isomerization of the chromophore in solution as compared to inside the protein cage where such motion may be suppressed.[13] Overcoming this limited fluorescence has led to numerous synthetic attempts through either functional-group modifications or changes in environmental conditions[14] to improve the general characteristics of GFP-type chromophores. Many of these changes have led directly to targeted applications in materials science[15] and biomedical studies.[16]

By eliminating the protein-cage structure, the determination of the photophysical properties (such as the molar extinction coefficients as well as the elucidation of complex dynamics such as fluorescence decay) for these chromophores has been simplified. Consequently, a wide variety of synthetic model systems have now been investigated.[17-19] However, the implementation of these types of chromophores in actual applications has been relatively scarce. One fairly clear area of interest for GFP-type chromophores is to further broaden their use as biological probes by covalently attaching them to macromolecules like DNA and proteins. Their implementation as biological probes for labeling of biomolecules such as DNA or peptides has only seen nascent interest in the literature,[16] but presents many encouraging attributes due to its small size and potential for fluorescence enhancement upon aggregation. A great deal is left to be understood about the complicated process by which amyloid peptides misfold to result in neurotoxic diseases such as Alzheimer's and Parkinson's disease. Fluorescence methods utilizing probes to track changes in particular are promising, but there remains a need for improvements in both fluorescence labels and methodology.[20] To best utilize these properties, a sophisticated technique must be implemented to detect the minute changes

in the chromophore and its environment.

Two-photon excited fluorescence (TPEF) has been shown to be an effective tool to interrogate the fundamentals of the excited state and identify structure-function relationships in organic molecules.[21,22] As a consequence, two-photon excited spectroscopy has been increasingly used as a tool for fluorescence imaging and the monitoring of aggregation[23] and conformational changes[24] in biomolecules to provide additional details inaccessible via linear spectroscopy. In the case of two-photon microscopic imaging, infrared excitations result in more localized, deeper imaging capabilities with reduced likelihood of autofluorescence and photodamage.[25] On the basis of a survey of the literature, there have been no previous studies performed determining the two-photon absorption cross sections or utilizing two-photon excited fluorescence of GFP-type chromophores. Many papers have been published investigating these characteristics for native fluorescent proteins,[25-28] and computational studies have been done on model chromophores, but neither affords a detailed, systematic examination for how substituent groups affect the overall two-photon absorption response, something that is permitted through investigation of the chromophores in solution.

Combining chemical modification and two-photon excited fluorescence as a guide for the design of an ideal chromophore for biological applications, efforts have recently been made in our lab toward the synthesis of two-photon active GFP-type chromophores having strong absorption and fluorescence emission in the visible region that are well suited for direct two-photon excitation using typical Ti:Sapphire lasers. Preliminary synthetic investigations were directed toward a yellow-fluorescent protein chromophore (zFP538)[29] that is structurally similar to that of the intrinsic chromophore found in GFP

but with absorption/ emission maxima at slightly longer wavelengths (376/468 nm) as compared to the more commonly used GFP. This chromophore is predicted to possess among the highest two-photon cross sections of the GFP-type chromophores (1420 GM) due to its strong dipolar[30] character, making it an ideal candidate for future applications as a biological tag[16] in peptide studies.

A diverse library of derivatized structures provides a valuable opportunity to look at a wide range of structural analogues and compare their behavior. The excited-state dynamics of GFP-type chromophores is an important area of study geared toward understanding the photophysical properties of the native chromophore and how such unique fluorescence characteristics are achieved. By synthesizing chromophores outside of the protein, researchers have investigated features isolated to the chromophore allowing for clearer determination of the significance of the protein structure in facilitating fluorescence as well as allowing for the ability to ascertain the role substituent groups play in altering these characteristics. The works of Meech[31-34] and Tolbert[35-37] have looked extensively at the dynamics of synthetic GFP-model systems striving to characterize their excited states. Making slight modifications to the general chromophore structure of GFP allows for probing both the structural and the electronic roles played in the excited state of the protein.

5.3 Experimental Section

All chemicals were used as received from the vendors, without further purification. NMR spectra were obtained on either Varian Inova 400 (399.96 MHz for ^{1}H; 100.57 MHz for ^{13}C) or Varian MR400 spectrometers. ^{1}H and ^{13}C NMR chemical shifts are reported in parts per million (ppm) relative to TMS, with the residual solvent

peak used as an internal reference. Multiplicities are reported as follows: singlet (s), doublet (d), doublet of doublets (dd), triplet (t), quartet (q), and multiplet (m). All NMR spectra were recorded at room temperature.

Unless otherwise specified, absorption and fluorescence emission spectra were recorded on an Agilent (model 8341) spectrophotometer and Fluoromax-2 fluorimeter (ISA instruments, NJ), respectively. Measurements were performed using a standard quartz cell with an optical path of 0.4 cm at room temperature. Fluorescence quantum yields (j) were measured comparing the integrated fluorescence intensity from the samples at low optical densities to that of the standard Coumarin 307 in methanol under the same conditions.

Cross sections were measured using the two-photon excited fluorescence (TPEF) method as described elsewhere.[38] A solution of Coumarin 307 in methanol ($<10^{-4}$ M) was used as the TPA reference across all of the wavelengths studied. Both MaiTai and Kapteyn Murnane Laboratories diode-pumped mode-locked Ti:Sapphire lasers were utilized for sample excitation. The beam was directed onto the sample cell (quartz cuvette, 0.4 cm path length), and the resultant fluorescence was collected perpendicular to the incident beam. A 1-in. focal length plano-convex lens was used to direct the collected fluorescence into a monochromator whose output was coupled to a photomultiplier tube. The photons were converted into counts by a photon-counting unit. A logarithmic plot of collected fluorescence photons versus input intensity was verified to yield a slope of 2, indicating the quadratic power dependence.

The fluorescence upconversion system used for time-resolved measurements of

the chromophores has been described previously.[39,40] In brief, a Tsunami Mode-Locked Ti:Sapphire (Spectra Physics) laser operated 120 fs pulses of 770-840 nm (gate pulse), with a repetition rate of 82 MHz, to generate light of 370-420 nm (excitation) from second harmonic generation in a β-barium borate crystal. Using a FOG-100 system (CDP Inc.), the gate pulse was channeled through a delay line, while the excitation light was up-converted and used to excite the samples. A monochromator detected the second harmonic generation of the gate pulse and emission from the samples and was enhanced by a photomultiplier tube. The samples were prepared in a solution of acetonitrile with an optical density of approximately 1. The measurements of the chromophores were observed using a quartz, rotating cell of 1 mm. The photostability of the chromophores in this study was confirmed by steady-state measurements prior to excitation. The kinetic fitting for the measurements of these chromophores was done after 1 ps of the date to avoid issues with deconvolution with the instrument response function.

5.4 Results and Discussion

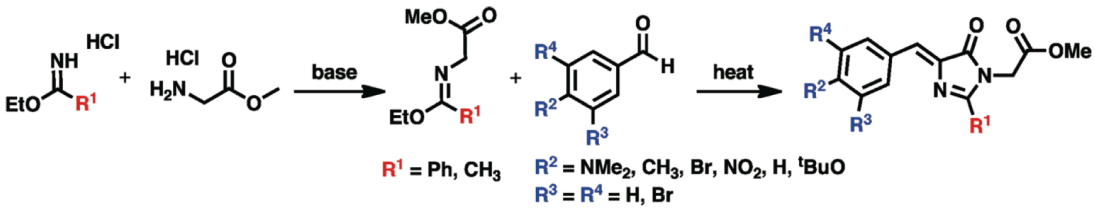

Figure 5.1 General synthesis of GFP-type chromophores.

The core imidazolone moiety of the GFP-type chromophore was synthesized using a well-studied cycloaddition reaction[41-43] combining an iminoglycine methyl ester and a substituted benzaldehyde as depicted in figure 5.1. Each of these precursors was readily obtainable from either commercial sources or a few synthetic steps. Two versions

of iminoglycine methyl esters were used in our experiment with each obtained in a single step from the base-catalyzed condensation reaction of the corresponding ethyl imidate hydrochloride with glycine methyl ester hydrochloride. These products were prone to decomposi- tion upon prolonged exposure to water/air so minimal purification was performed if NMR analysis showed high conversions rates for the crude product. Reactions with benzaldehyde derivatives were performed to great success under moderate heating in toluene overnight. Products were generally collected as oils that often crystallized upon standing for a few hours. A series of nine different GFP-type chromophores were eventually synthesized with a variety of different functional groups designed to examine different substituent effects (Table 5.1).

Table 5.1 Steady-state spectroscopy of GFP-type chromophores in acetonitrile.

abb.	R1	R2	R3	R4	λ_{abs} (nm)	λ_{emis} (nm)	ε (M^{-1} cm^{-1})	Stokes Shift (cm^{-1})	QY
HC	Me	H	H	H	347	417	1.9×10^4	4840	1.3×10^{-4}
MC	Me	Me	H	H	355	419	2.0×10^4	4300	2.2×10^{-4}
BrC	Me	Br	H	H	354	419	2.2×10^4	4380	6.5×10^{-4}
DiBrC	Me	H	Br	Br	355	426	9.2×10^3	4700	1.5×10^{-2}
^{t}BuOC	Me	^{t}BuO	H	H	361	436	2.6×10^4	4770	2.1×10^{-4}
NPC	Ph	NO2	H	H	370	522	2.0×10^4	7070	6.8×10^{-4}
NC	Me	NO2	H	H	376	488	4.1×10^3	6100	7.7×10^{-3}
DMC	Me	NMe2	H	H	422	488	6.8×10^3	3210	3.4×10^{-4}
BC	Ph	NMe2	H	H	453	533	4.0×10^3	3310	1.1×10^{-3}

The effects of conjugation length were primarily examined through the substitution of a phenyl ring at position R^1 for a methyl group with the expectation of red-shifted steady- state spectra and increased TPA cross sections (BC, NPC). At positions R^2-R^4 along the benzylidene moiety, charge-transfer groups were incorporated (NC, DMC) as a means for improving the overall TPA characteristics. Other derivatives with

weaker electronic effects such as MC substituted with a methyl group at R^2 and HC with a hydrogen at the same position served as systems to judge the how significant the hydroxyl group is in defining the photophysical characteristics of the GFP chromophore. Two different chromophores were synthesized with bromine substituent groups, BrC with substitution at the para-position and DiBrC substituted with bromines at both meta positions to interrogate whether the substitution position would substantially change the fluorescence characteristics of the chromophore. Similarly, a derivative (^{t}BuOC) was synthesized to examine the physical size effects of substituent groups as well as to structurally mimic the electronic effects of the hydroxyl group found in the GFP chromophore. With the broad applicability of this synthesis, more diverse functionality could be incorporated into the chromophore by further varying the R-groups with a wider variety of substituents. Our synthetic strategy has also permitted the incorporation of the critical pendant ester into the basic chromophore structure, which may be utilized as a means to attach the molecule to peptide chains or otherwise covalently bond to other molecules of interest.

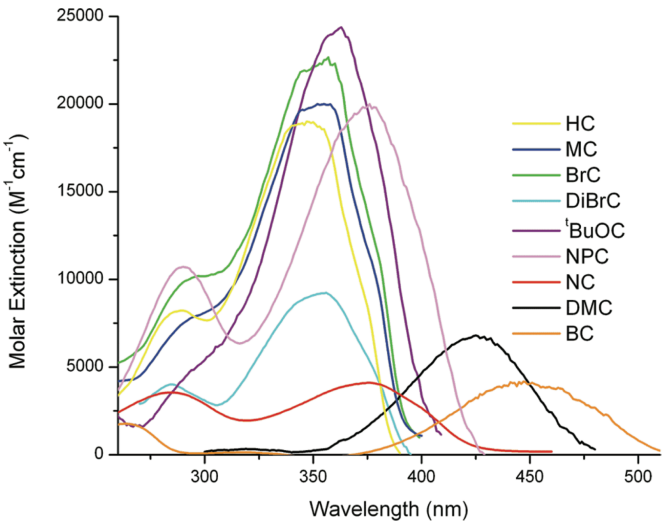

Figure 5.2 Absorption spectra of synthesized chromophores in acetonitrile, scaled to reflect the molar extinction coefficient for each. HC, yellow; MC, blue; BrC, green; DiBrC, cyan; ^{t}BuOC, purple; NPC, magenta; NC, red; DMC, black; BC, orange.

Other typical synthetic strategies have implemented variations of the Erlenmeyer azlactone synthesis[44,45] to incorporate glycine and benzaldehyde to yield upon cyclizing under alkaline conditions in acetic anhydride an azlactone structure.[46] This may be further transformed to the corresponding imidazolinone structure by reacting with an amine (typically methylamine) to give the final model GFP chromophore with a methyl or some other alkyl chain substituted at the amidic nitrogen. Modifications can be made to this synthetic methodology to broaden the resultant chromophore functionality; however, a synthetic strategy such as the one implemented in this study offers substantially more ability for tuning the overall characteristics of the final synthesized chromophore though the incorporation of diverse functionality.

Initial steady-state properties were investigated for the synthesized chromophores. Figure 5.2 shows the steady-state absorption of the chromophores plotted as molar

extinction coefficient versus wavelength. The relative positioning of the absorption bands follows the expected trends pertaining to conjugation effects and charge-transfer groups on photon absorption. The chromophores with the shortest wavelength absorptions are those with shortest conjugation lengths (methyl groups at R^1) and fairly weak electronic groups at R^2 (HC, MC, BrC). Substitution position (DiBrC) and the relative bulk of a group (^{t}BuOC) seem to have no marked influence on the relative shape or position of the band. The absorption of dibromo-substituted DiBrC is indistinguishable from BrC, indicative of a small effect from either meta or para group-substitution on the steady state. The charge-transfer NC chromophore has the broadest absorption centered at 376 nm, but demonstrates a much less pronounced effect from the strongly electron-withdrawing nitro group than that caused by the tertiary amine in DMC whose absorption is red-shifted more than 70 nm as compared to that of HC. Further interrogating the tunability of the absorption of GFP-type chromophores, NPC and BC provide evidence as to the impact of conjugation on the wavelength of absorption. No noteworthy shift in position is found between NC and NPC, while the same comparison of BC with DMC shows a further 30 nm shift results from the additional conjugation.

Bromo (BrC), methyl (MC), and hydrogen (HC) derivatives have absorption profiles very similar to that of the GFP chro- mophore (λ = 376 nm) but have fluorescence emission significantly blue-shifted without the donating character of the hydroxyl group present for GFP chromophore (λ = 490 nm). The emission profiles for HC, MC, BrC, and DiBrC exhibit good mirror image symmetry with respect to their respective absorption curves indicative of very similar transitions occurring in both absorption and emission. ^{t}BuOC has a shifted emission as compared to those four

previously referenced chromophores that is consistent with its red-shifted absorption profile. The Stokes shift for ^{t}BuOC is very similar to those chromophores containing similarly weak electronic functional groups with all having shifts between 4300 and 4900 cm^{-1}. As observed in the absorption studies, with the incorporation of stronger donor (NMe_2) or acceptor (NO_2) substituents into the structure, pronounced red shifts in the emission spectra are induced. The addition of either group onto the core chromophore results in approximately the same fluorescence maximum near 488 nm, but with a large difference in Stokes shift between NC (6100 cm^{-1}) and DMC (3210 cm^{-1}). A significant difference in the emission peak-shape is noted as NC and has a broad fluorescence emission pronounced over a wide range of wavelengths, while DMC has a much narrower peak shape that has a far larger degree of symmetry on both the blue and the red edges. Finally, further increases of the effective conjugation length of the molecule through the inclusion of an additional phenyl substituent (NPC, BC) at R^1 also induce a large shift in the fluorescence emission to near that of the initial zFP538 target chromophore (λ = 538 nm).

Fluorescence quantum yields for the synthesized chromophores have values on the order of 10^{-3}-10^{-4} (Table 5.1) consistent with those previously synthesized.[19] Interestingly, when R^1 is changed to dibromo-functionalized at the meta positions, the quantum yield is increased significantly to 10^2. This indicates that the position of the substitution can have a profound effect on the E-Z isomerization and reduce the radiationless loss of fluorescence intensity. As such, the GFP- type chromophores were synthesized using the procedure de- scribed earlier to incorporate functionality meant to illuminate some of the basic photophysical characteristics as well as the effect of

attaching different groups at positions within the chromophore. The steady-state measurements provide a baseline for the overall photophysical considerations, but more information may be extracted from time-resolved and ultrafast measurements reported in what follows.

The two-photon absorption cross sections of the synthesized chromophores were investigated using excitations around 800 nm. An examination of the TPA characteristics for the synthesized chromophores illuminates the overall significance of different substituent groups on GFP-type chromophores and helps determine which properties make for well-designed two-photon labels for biological studies. For the determination of the best-suited chromophore for application, primary focus was placed on behavior under excitations right around 800 nm as this specifies a material with characteristics most appropriate for direct examination using typical Ti:Sapphire laser sources.

Table 5.2 shows the calculated two-photon cross sections for the GFP-type chromophores at wavelengths near 800 nm. The single member of the series that exhibited comparatively large response in this region was DMC with a cross section near 30 GM at 800 nm. This compares favorably to those cross-section values of 6-14 GM obtained in several experimental studies for wild- type GFP that contains a chromophore structurally similar to DMC.[26,47] Rebane *et. al.*[26-28] have published several reports detailing the basic two-photon absorption characteristics of an assortment of other fluorescent protein analogues to GFP, which make for good comparisons to our synthetically produced molecules. The authors determined absolute cross sections over a broad range of excitation wavelengths (500-1300 nm) finding that values were especially small between 700 and 800 nm for many FPs apart from some red varieties (TagRFP,

mRFP) whose cross sections approach or exceed 100 GM over this range. This would indicate that expanding the extent of conjugation through some means and consequently shifting the absorption to longer wavelengths might have the potential for increased cross sections. Other studies using DFT calculations have also been performed,[48,49] examining the theoretical two-photon absorption bands in a selection of model FP chromophores predicting two-photon absorption maxima to occur in the 500-700 nm excitation regime with maximum values to be ~175 GM near 600 nm and relative minima near 800 nm.

Table 5.2 Two-photon absorption characteristics of two-photon absorption chromophores near 800 nm.

Excitation Wavelength (nm)	Chromophore	QY	δ (GM, 10^{-50} cm^4 s $photon^{-1}$)
780 nm	HC	1.3×10^{-4}	1.69
780 nm	MC	2.2×10^{-4}	0.468
780 nm	BrC	6.5×10^{-4}	0.0525
780 nm	DiBrC	1.5×10^{-2}	0.207
780 nm	tBuOC	2.1×10^{-4}	3.19
780 nm	NC	7.7×10^{-3}	2.37
780 nm	DMC	3.4×10^{-4}	25
780 nm	BC	1.1×10^{-3}	1.32
800 nm	NC	7.7×10^{-3}	1.79
800 nm	DMC	3.4×10^{-4}	29
800 nm	BC	3.4×10^{-4}	17.1
820 nm	NC	7.7×10^{-3}	0.432
820 nm	DMC	3.4×10^{-4}	39.4
820 nm	BC	1.1×10^{-3}	13.4

The effect of conjugation may be evaluated in part with the comparison of BC to DMC. While the additional conjugation produced a red-shifted absorption (Figure 5.1), the overall two- photon absorption response is not as large in magnitude as that found for

DMC. The implication of this points to a smaller transition dipole moment for BC than is found in its structural analogue. Charge-transfer groups were expected to play a critical role in the overall two-photon absorption response of the chromophores as strong donor (NMe_2) and acceptor (NO_2) groups have been shown to significantly affect the two-photon absorption cross sections of branched and extended conjugation systems.[50,51] Examining the cross sections measured for the synthesized chromophores, strong dipole character in DMC and BC results in larger cross sections, but is not reflected in the case of NC. The other synthesized chromophores were excited at wavelengths far from their two-photon absorption maxima, and thus accordingly had smaller cross sections (HC, MC, BrC, etc.), or for those excited near twice the one-photon peak, simply had smaller cross sections at these wavelengths (NC, BC). By shortening the wavelengths of excitations, improved performance was noted for most systems with BrC and ^{t}BuOC approaching 10 GM cross sections at 740 nm. This feature is not entirely unexpected as it has been reported both experimentally[26] and theoretically[49] that there is a resonance enhancement effect of the S_1-S_n transition in the range of 550-750 nm, which results in an additional strong two-photon absorbing band at these shorter wavelengths.

Lifetime measurements like two-photon absorption cross sections are important because they can explain about the environment of the chromophore and are the foundation of FRET-like studies in biological systems. To fundamentally understand the effect that the various substituent groups have in determining the fluorescence lifetime of GFP- type chromophores, a systematic investigation was undertaken to compare fluorescence lifetimes. Table 3 shows the fluorescence lifetimes of the chromophores as observed in acetonitrile. All of the chromophores exhibit a two-component lifetime with

the shortest component primarily being subpicosecond except notably for BC (1.11ps), NC (4.7ps), and DiBrC (4.85ps). There is no clear impact of the substituent group on the duration of this component; however, there is a strong dependence on substitution position of a substituent. These results are consistent with other examinations[36,52] of fluorescence lifetimes with respect to functional group substitution and how it relates to decay behavior. The short components in these chromophores are a result of fast internal conversion, and the long components are from conformational relaxation from isomerization processes.

Table 5.3 Fluorescence lifetimes of GFP-type chromophores.

abb.	τ_1 (ps)	τ_2 (ps)
HC	0.45 ± 0.09	2.20 ± 0.04
MC	0.50 ± 0.02	1.28 ± 0.06
BrC	0.75 ± 0.04	4.31 ± 0.05
DiBrC	4.85 ± 0.05	62.3 ± 0.06
tBuOC	0.38 ± 0.04	0.84 ± 0.04
NPC	0.40 ± 0.05	1.3 ± 0.2
NC	0.47 ± 0.3	53.2 ± 0.6
DMC	0.566 ± 0.001	3.257 ± 0.001
BC	1.11 ± 0.04	9.74 ± 0.03

As a baseline for comparison, an unsubstituted version of the GFP-type chromophore (HC) was synthesized with a hydrogen at R^2. HC shows a fast initial component (0.45 ps) that is among the quickest components for all of the chromophores and a secondary component that lasts 2.2 ps. For comparison, this roughly equates to the observed behavior for the anionic form of the typical GFP model chromophore, 4` -hydroxybenzylidene- 2,3-dimethylimidazolone (HBDI), in acetonitrile whose two-component lifetime was observed[32] to be 0.45 and 1.4 ps. The shortest wavelength

absorbing species nearest to that of unsubstituted HC are the *para*-methyl (MC)- and *para*-bromo (BrC)-substituted versions that both show similar emissive properties as compared to HC in the steady state. As shown in Figures 5.2 and 5.3, these chromophores have nearly identical absorption and emission maxima, so it leads one to expect similar excited-state fluorescence decay profiles. An examination of the fluorescence decays indicates a two-component lifetime with the shortest lasting less than 1 ps.[33] It should be noted that the minor differences in lifetimes may be related to the withdrawing/donating effect of the group substituted at R^2 with the slight donating methyl group causing the shortest lifetime (MC) and the electron- withdrawing bromo group resulting in the longest with the lifetime of BrC nearly 4 times that of HC. It seems that the excited-state lifetime is strongly related to the substitution of the benzylidene ring and that generally the chromophores with electron-donating substituents will have among the shortest lifetimes, often less than that of unsubstituted, while the presence of electron-withdrawing groups will result in prolonged excited-state lifetimes.

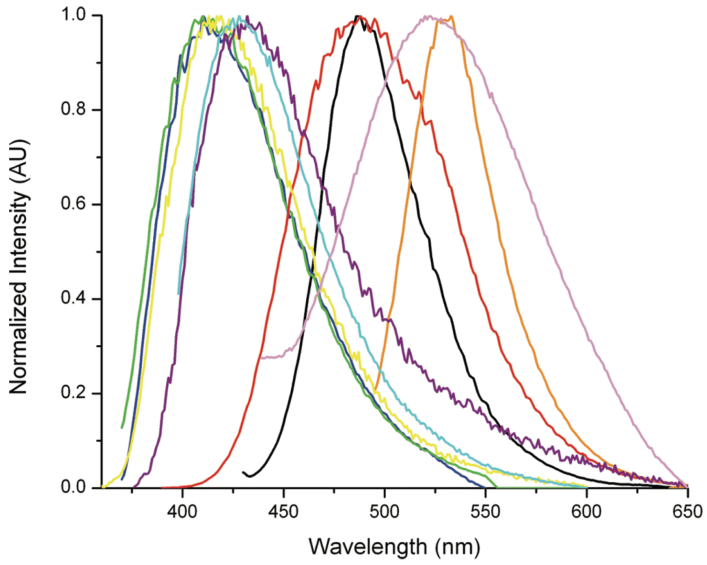

Figure 5.3 Normalized emission spectrum of the synthesized chromo- phores in acetonitrile. HC, yellow; MC, blue; BrC, green; DiBrC, cyan; ^{t}BuOC, purple; NPC, magenta; NC, red; DMC, black; BC, orange.

The next two chromophores (DiBrC, ^{t}BuOC) offer several different functional-group characteristics from our set of derivatives. DiBrC represents the lone example of a meta- and disubstituted chromophore and provides an interesting comparison with BrC as to the extent placement of groups effects fluorescence lifetime. The tert-butoxy-substituted ^{t}BuOC serves as the closest example to replicating the same inductive properties as the hydroxyl group of the most commonly used GFP- model chromophore HBDI, but also represents the largest physical functionalization at R^2, R^3, or R^4. The different fluorescence behavior of these two is among the starker contrasts of the whole series of chromophores. Despite similar steady-state properties, DiBrC has the longest observed fluorescence lifetime with its secondary component lasting 62.8 ps, while ^{t}BuOC has the shortest lifetimes for both components at 0.38 and 0.84 ps. The long lifetimes for DiBrC are directly related to the meta- substitution of the bromo groups that has been shown to

create a potential barrier for isomerization about the exocyclic double bond, resulting in far longer lifetimes and diminished likelihood of internal conversion.[36] The behavior of ^{t}BuOC is more puzzling as any perceived effects of size should have resulted in shorter and not longer fluorescence lifetimes.

The final comparison of chromophores to consider is that of those possessing the strongest electronic groups and should exhibit certain aspects of charge-transfer. The first two (NC, NPC) both contain para-nitro groups, and, as was found in the steady state, NPC has a slightly red-shifted fluorescence maximum. The final two shown in Table 5.2 (DMC, BC) are both para-substituted with dimethylamino groups. Both nitro groups and dimethylamino groups have been shown to be excellent moieties for the synthesis of charge-transfer compounds, but with their incorporation into GFP-type chromophores, defining clear explanations for their very different behavior is quite challenging. NC has a tremendously long two-component life- time that may not be explained under the same considerations as the long lifetime for DiBrC as it cannot be attributed to a substitution effect. However, it would seem as though the strong withdrawing characteristics of the nitro group promote a large difference between ground- and excited-state structures that is exhibited by the large Stokes shift observed from steady-state measurements. This reorganization may result in a complicated (slow) relaxation pathway and a barrier to quick internal con- version. Unfortunately, the structural derivative NPC behaves very differently from its less conjugated analogue. The fluorescence lifetimes for it are closer to ^{t}BuOC in time-scale, which casts doubt about the added effects of replacing the methyl group at R1 with a phenyl group and would seem to be completely at odds with the expected behavior given the results for NC.

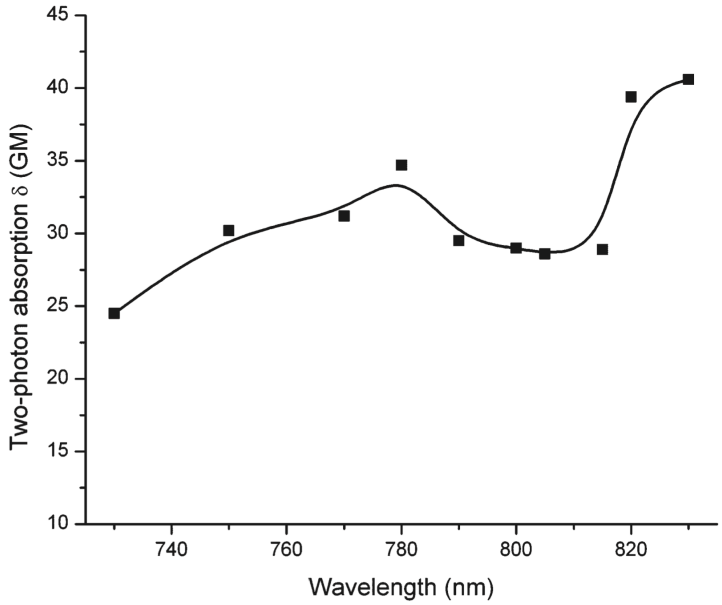

Figure 5.4 Two-photon absorption spectrum of DMC. Fit line provided to guide the eye.

Given the TPA response of DMC (and to some extent BC), the expectation is that there might be longer relative fluorescence lifetimes indicative of the donor-acceptor behavior known to be a general promoter for such characteristics (Figure 5.4). However, the fluorescence lifetimes are both fairly consistent with those found for minor electronic substituents (BrC). There is a prolonged reorganization time that is consistent with a somewhat complicated relaxation pathway, but does not exhibit long charge-transfer type lifetimes. BC has a two-component decay that agrees favorably with similar GFP-type structures adorned with additional phenyl rings.[52] The added component is presumed to be associated with a pronounced increase in the importance of the axis of rotation about the bond connecting R^1. Figure 5.5 shows a representative time-resolved fluorescence lifetime plot of the synthesized chromophores (DMC). To better elucidate the difference in their fluorescence lifetimes, BC and DMC time-resolved fluorescence decays in acetonitrile (0.38 cP) were compared to those obtained from a very viscous ethanol-

amine (19.37 cP) solution. The lifetimes of both were found to be relatively unaffected by the dramatic change in solvent viscosity with BC lifetimes being approximately doubled and DMC slowed by more than 5 times that found in acetonitrile. This result seemingly is the opposite of the expected behavior with the bulkier BC having less of a viscosity-dependent lifetime than the smaller DMC. The effect is likely again a result of a twisting component of the added phenyl substituent.

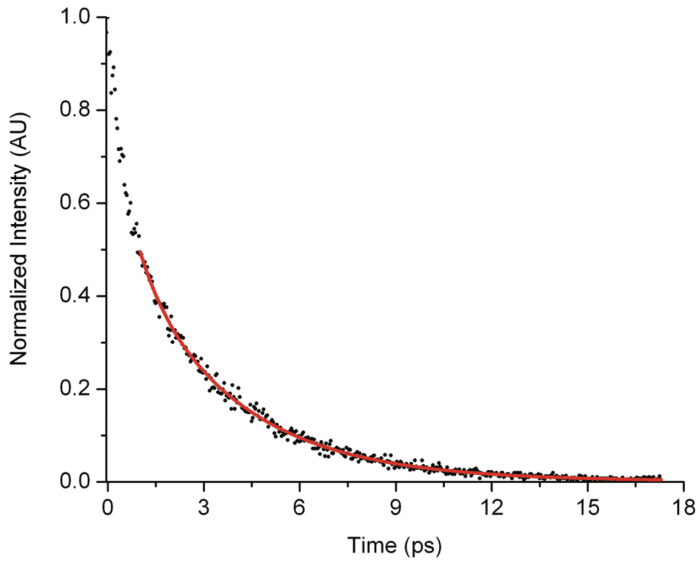

Figure 5.5 Time-resolved fluorescence lifetime decay of DMC in acetonitrile. Best-fit is represented in red.

5.5 Conclusions

Two-photon active green fluorescent protein-type chromophores were synthesized with a diverse set of substituent groups and evaluated for their fundamental steady-state characteristics. A generalized approach for chromophore synthesis was developed, allowing for maximum flexibility for the incorporation of functional groups such as donor-acceptor substituents or additional groups to provide extended conjugation. The GFP-type chromophores were found to possess modest two-photon absorption cross

sections near 800 nm with the dimethylamino- substituted DMC clearly having the largest value at nearly 40 GM. Time-resolved fluorescence lifetimes were determined for the synthesized molecules finding that each decayed in a biexponential fashion with a subpicosecond component and a longer picosecond component. The individual effects of substitution position of functional groups and relative bulk size were evaluated and found to be rather significant in changing the fluorescence-decay characteristics in the case of substitution, but ambiguous with respect to relative group bulk. On the whole, these molecules show promise as biological markers, especially DMC given its two-photon absorption response, for application in the study of conformation changes and aggregation of amyloid peptides, known to play an important role in many neurodegenerative diseases. Investigations are currently in progress using these chromophores as fluorescence dyes in such biological studies of peptides

References:

[1] Megley, C. M.; Dickson, L. A.; Maddalo, S. L.; Chandler, G. J.; Zimmer, M. J. Phys. Chem. B 2009, 113, 302.

[2] Zimmer,M.Chem.Rev.2002,102,759.

[3] Tsien,R.Y.Annu.Rev.Biochem.1998,67,509.

[4] Matz, M.; Fradkov, A.; Labas, Y.; Savitsky, A.; Zaraisky, A.; Markelov,M.;Lukyanov,S.Nat.Biotechnol.1999,17,969.

[5] Taylor, D.; Woo, E.; Giuliano, K. Curr. Opin. Biotechnol. 2001, 12, 75.

[6] Zipfel, W. R.; Williams, R. M.; Webb, W. W. Nat. Biotechnol. 2003, 21, 1369.

[7] Heim,R.;Prasher,D.C.;Tsien, R. Y. Proc. Natl. Acad. Sci. U.S.A. 1994, 91, 12501.

[8] Yang, F.; Moss, L. G.; Phillips, G. N. Nat. Biotechnol. 1996, 14, 1246.

[9] Reid, B. G.; Flynn, G. C. Biochemistry 1997, 36, 6786.

[10] Niwa, H.; Inouye, S.; Hirano, T.; Matsuno, T.; Kojima, S.; Kubota, M.; Ohashi, M.; Tsuji, F. I. Proc. Natl. Acad. Sci. U.S.A. 1996, 93, 13617.

[11] Weber,W.;Helms,V.;McCammon,J.;Langhoff, P. Proc. Natl. Acad. Sci. U.S.A. 1999, 96, 6177.

[12] Chattoraj, M.; King, B. A.; Bublitz, G. U.; Boxer, S. G. Proc. Natl. Acad. Sci. U.S.A. 1996, 93, 8362.

[13] Meech,S.R.Chem.Soc.Rev.2009,38,2922.

[14] Baldridge, A.; Samanta, S.; Jayaraj, N.; Ramamurthy, V.; Tolbert, L. J. Am. Chem. Soc. 2010, 132, 1498.

[15] You, Y.; He, Y.; Borrows, P.; Forrest, S.; Petasis, N. ;Thompson, M. Adv. Mater. 2000, 12, 1678.

[16] Stafforst,T.;Diederichsen,U.Eur.J.Org.Chem.2007,899.

[17] Ivashkin,P.;Yampolsky,I.;Lukyanov, K. Russ. J. Bioorg. Chem. 2009, 35, 652.

[18] Bourotte, M.; Schmitt, M.; Follenius-Wund, A.; Pigault, C.; Haiech, J.;

Bourguignon, J. Tetrahedron Lett. 2004, 45, 6343.

[19] Follenius-Wund,A.;Bourotte,M.;Schmitt,M.;Iyice,F.;Lami, H.; Bourguignon, J.-J.; Haiech, J.; Pigault, C. Biophys. J. 2008, 85, 1839.

[20] Munishkina, L.; Fink, A. Biochim. Biophys. Acta, Biomembr. 2007, 1768, 1862.

[21] Parthasarathy, A.; Ahn, H.-Y.; Belfield, K. D.; Schanze, K. S. ACS Appl. Mater. Interfaces 2010, 2, 2744.

[22] Narayanan,A.;Varnavski,O.P.;Swager,T.M.; Goodson,T. J. Phys. Chem. C 2008, 112, 881.

[23] Wang,Y.;Goodson,T.,III.J.Phys.Chem.B2007,111,327.

[24] Wang, Y.; Clark, T. B.; Goodson, T. J. Phys. Chem. B 2010,114, 7112. (25) Blab, G. A.; Lommerse, P. H. M.; Cognet, L.; Harms, G. S.; Schmidt, T. Chem. Phys. Lett. 2001, 350, 71.

[26] Drobizhev,M.;Makarov,N.S.;Hughes,T.;Rebane, A. J. Phys. Chem. B 2007, 111, 14051.

[27] Drobizhev,M.;Tillo,S.;Makarov,N.S.;Hughes,T.E.;Rebane, A. J. Phys. Chem. B 2009, 113, 855.

[28] Drobizhev,M.;Tillo,S.;Makarov,N.;Hughes,T.;Rebane, A. J. Phys. Chem. B 2009, 113, 12860.

[29] Remington,S.J.;Wachter,R.M.;Yarbrough,D.K.;Branchaud, B.; Anderson, D. C.; Kallio, K.; Lukyanov, K. A. Biochemistry 2005, 44, 202.

[30] Rumi, M.; Ehrlich, J. E.; Heikal, A. A.; Perry, J. W.; Barlow, S.; Hu, Z.; McCord-Maughon, D.; Parker, T. C.; R€ockel, H.; Thayumana- van, S.; Marder, S. R.; Beljonne, D.; Br_edas, J.-L. J. Am. Chem. Soc. 2000, 122, 9500.

[31] Litvinenko, K.; Webber, N.; Meech, S. J. Phys. Chem. A 2003, 107, 2616.

[32] Mandal, D.; Tahara, T.; Meech, S. J. Phys. Chem. B 2004, 108, 1102.

[33] Mandal,D.;Tahara,T.;Webber,N.;Meech, S. Chem. Phys. Lett. 2002, 358, 495.

[34] Webber, N.; Litvinenko, K.; Meech, S. J. Phys. Chem. B 2001, 105, 8036.

[35] Dong, J.; Solntsev, K.; Tolbert, L. J. Am. Chem. Soc. 2006, 128, 12038.

[36] Solntsev,K.M.;Poizat,O.;Dong,J.;Rehault,J.;Lou,Y.;Burda, C.; Tolbert, L. M. J. Phys. Chem. B 2008, 112, 2700.

[37] Usman,A.;Mohammed,O.;Nibbering,E.;Dong,J.;Solntsev, K.; Tolbert, L. J. Am.

Chem. Soc. 2005, 127, 11214.

[38] Xu,C.;Webb,W.J.Opt.Soc.Am.B1996,13,481.

[39] Varnavski,O.;Goodson,T.Chem.Phys.Lett.2000,320,688.

[40] Flynn, D. C.; Ramakrishna, G.; Yang, H.-B.; Northrop, B. H.; Stang, P. J.; Goodson, T. J. Am. Chem. Soc. 2010, 132, 1348.

[41] Lerestif, J.; Bazureau, J.; Hamelin, J. Tetrahedron Lett. 1993, 34, 4639.

[42] Lerestif,J.;Perrocheau,J.;Tonnard,F.;Bazureau,J.;Hamelin,J. Tetrahedron 1995, 51, 6757.

[43] Baldridge, A.; Kowalik, J.; Tolbert, L. M. Synthesis 2010, 2010, 2424.

[44] Jun, E. E. Justus Liebigs, Ann.Chem.1893,275,1.

[45] Conway, P. A.; Devine, K.; Paradisi, F. Tetrahedron 2009, 65, 2935.

[46] He,X.;Bell,A.;Tonge,P.Org.Lett.2002,4,1523.

[47] Xu, C.; Zipfel, W.; Shear, J. B.; Williams, R. M.; Webb, W. W. Proc. Natl. Acad. Sci. U.S.A. 1996, 93, 10763.

[48] Nifosi,R.;Luo,Y.J.Phys.Chem.B2007,111,505.

[49] Nifos,R.;Luo,Y.J.Phys.Chem.B2007,111,14043. (50) Bhaskar, A.; Ramakrishna, G.; Lu, Z.; Twieg, R.; Hales, J.; Hagan, D.; Van Stryland, E.; Goodson, T., III. J. Am. Chem. Soc. 2006, 281, 1653.

[51] Bhaskar, A.; Ramakrishna, G.; Twieg, R.; Goodson, T. J. Phys. Chem. C 2007, 111, 14607.

[52] Petkova, I.; Dobrikov, G.; Banerji, N.; Duvanel, G.; Perez, R.; Dimitrov, V.; Nikolov, P.; Vauthey, E. J. Phys. Chem. A 2010, 114, 10.

[53] Cornforth,J.; Cornforth,R. J.Chem.Soc.1947,96.

Chapter 6 Ultrafast Optical Excitations in Supramolecular Metallacycles with Charge Transfer Properties

6.1 Introduction

New organometallic materials such as two-dimensional metallacycles and three-dimensional metallacages are important for the development of novel optical, electronic, and energy related applications. Here, the ultrafast dynamics of two different platinum containing metallacycles have been investigated by femtosecond fluorescence upconversion and transient absorption. These measurements were carried out in an effort to probe the charge transfer dynamics and the rate of intersystem crossing in metallacycles of different geometries and dimensions. The processes of ultrafast intersystem crossing and charge transfer vary between the two different classes of metallacyclic systems studied. For rectangular anthracene-containing metallacycles the electronic coupling between adjacent ligands was relatively weak while for the triangular phenanthrene-containing structures there was a clear interaction between the conjugated ligand and the metal complex center. The transient lifetimes increased with increasing conjugation in that case. The results show that differences in the dimensionality and structure of metallacycles result in different optical properties, which may be utilized in the design of nonlinear optical materials and potential new, longer lived excited state materials for further electronic applications.

6.2 Background

There is a need for superior organic and inorganic materials for advanced optical applications.[1] Organic chromophores and macromolecules have been investigated for their potential use in optical and electronic applications and great progress has been made in substantially increasing the merit of these useful materials.[2] In addition to the various organic materials that have been probed for their optical effects there has been interest in studying organometallic systems as well.[3-7] Many of these charge transfer materials have shown optical properties that are useful for optical limiting and other nonlinear optical effects.[8-11] The interaction of π structures with d-orbital metal centers has been utilized in electronic interactions that are important for novel applications.[12,13] Both metal to ligand (ML) and ligand to metal (LM) interactions have been exploited for intense absorption properties in the visible and near-IR spectral regions.[3-5]

Platinum-containing organometallic complexes have been extensively investigated for their applications in optical limiting.[14,15] These systems display singlet and triplet excitons in the visible and near-IR regions. In this regard, several platinum acetylene complexes have been synthesized and investigated in the literature to understand their applicability as nonlinear optical materials. They are also good systems for investigating excited state phenomena such as excited state absorption (ESA), intersystem crossing (ISC), triplet state absorption (TTA), two photon absorption[11,16], excimers[5] and phosphorescence[4]. Previous measurements have tailored the conjugated linkages that separate metal centers to promote the degree of π-d interactions, which are important for greater charge correlation throughout the structure. Many of the previous structures studied have been essentially linear with the metal in the center or at either end

of the linkage. Several investigations demonstrated a strong charge correlation within the π-d interaction, which altered (in some cases enhanced) the electronic and nonlinear optical properties of the system. This gave strong justification for the creation of novel materials based on this organometallic motif for the enhancement of electronic interactions for specific optical applications.

While there have been a number of previous investigations that primarily focused on linear structures, the effects of the geometry of the organometallic system have received limited investigation. There is great cause to suggest that structural geometry plays an important role in the electronic transitions of different organometallic systems. Organic macromolecular systems with geometries varying from branched, cyclic, and flat two-dimensional motifs have been investigated by both steady-state and time-resolved measurements.[16-18] It has been found that the symmetry and degree of planarity in these systems is a critical factor in describing their optical excitations. In a similar manner, novel organometallic structures of varying geometry and/or symmetry may show similar correlations between structure and function.[19] Furthermore, only a few organometallic cage structures have had their fluorescent properties studied.[20] Advances in the synthesis of self-assembled Pt-containing metallacyclic and metallacage supramolecules of varying geometry (rectangular and triangular) and dimensionality (2D and 3D) allow for the steady-state and time-resolved properties of such supramolecules to be investigated.[21-27] Femtosecond measurements of fluorescence upconversion and transient absorption spectra have been studied for both the rectangular and triangular Pt-containing organometallic supramolecules in this contribution. The fluorescence lifetimes, as well as the transient absorption lifetimes, of the two architectures are compared. The effect of

the charge transfer character is compared for a series of four different supramolecular rectangles, a series of three different supramolecular triangles, as well as a supramolecular cage structure. A model is proposed that describes the importance of particular excited-state mechanisms, which are dependent upon the macromolecular geometry. These findings suggest that the organometallic structures studied are good candidates for nonlinear optical materials and their optical properties can be tailored based on their geometry.

6.3 Experimental Section

Pt-anthracene acceptor **1**,[24] supramolecular rectangles **2-4**,[24] supramolecular triangles **5-7**,[25] and supramolecular metallacage **8**[26] were synthesized according to literature procedures. Further extentions to the rectangular clip design incorporating ethynyl functionality have recently been developed, although they were not studied in this manuscript.[27] The transient absorption and upconversion measurements were carried out in acetone (Aldrich) unless stated otherwise.

An Agilent UV-VIS absorption spectrometer was used to obtain optical absorption spectra. A Jobin Yvon Spex Fluoromax-2 spectro fluorometer was used to determine the fluorescence spectra.

The two-photon excited fluorescence (TPEF) method involves monitoring the fluorescence intensity as a function of incident intensity. The laser source used in our experiments is either a Ti: Sapphire oscillator (Kapteyn Murnane) that can be tuned from 760nm-830nm or an amplified system (Spectra-Spitfire) with an Optical Parametric Amplifier that can be tuned from 300nm-2μm. The input intensity can be regulated using a neutral density (ND) filter designed for femtosecond pulses. The fluorescence is

measured by a photomultiplier tube (PMT) (R7518P, Hamamatsu). A counting circuit (M8485 counting board, C3866 counting circuit, Hamamatsu) assembly, which is interfaced with a computer, converts the photocurrent from the PMT into an arbitrary number of counts. In this manner, the TPEF intensity can be quantified. A two-photon excited process is ensured when a logarithmic plot of the TPEF intensity versus input intensity is a straight line with a slope of 2.

Femtosecond transient absorption investigations have been carried out using ultrafast pump-probe spectrometer detecting in the visible region. This system contains 1-mJ, 100-fs pulses at 800 nm with a repetition rate of 1 kHz that were obtained from a Nd:YLF(Evolution)-pumped Ti:Sapphire regenerative amplifier (Spectra physics spitfire) with the input from a Millennia-pumped Ti:Sapphire oscillator (Spectra physics, Tsunami). The output of laser beam was split to generate pump and probe beam pulses with a beam splitter (85 and 15%). The pump beam was produced by an optical parametric amplifier (OPA-800). The pump beam used in the present investigation, i.e., 420 nm, was obtained from the fourth harmonic of the idler beam and was focused onto the sample cuvette. The probe beam was delayed with a computer controlled motion controller and then focused into a 2-mm sapphire plate to generate a white light continuum. The white light is then overlapped with the pump beam in a 2-mm quartz cuvette containing the sample, and the change in absorbance for the signal is collected by a charge-coupled device detector (Ocean optics). Data acquisition is controlled by the software from Ultrafast Systems Inc. The typical energy probe beam is <0.1 μJ, while the pump beam is around ~1-2 μJ per pulse. Magic angle polarization has been maintained between the pump and probe using a wave plate. Pulse duration has been

obtained from the nonresonant fitting of the solvent response, which is around 120 fs. The sample is stirred by a rotating magnetic stirrer, and little degradation of the sample was observed during the experiments.

The fluorescence upconversion system used in our time-resolved experiments has been described previously.[29] To excite our samples, a FOG-100 system (CDP) generates second harmonic light (400 nm) from a mode-locked Ti-sapphire laser. Polarization of the excitation beam for anisotropy measurements was controlled with a Berek compensator. All samples were held in a 1 mm thick rotating sample cuvette. Horizontally polarized fluorescence emitted from the sample was up-converted in a nonlinear crystal of b-barium borate using a pump beam at 800 nm, which first passed through a variable delay line. The instrument response function (IRF) was determined from the Raman signal of water. Lifetimes were obtained by convoluting the decay profile with the instrument response function. Spectral resolution was achieved by using a monochromator and photomultiplier tube. Under the experimental conditions, the organometallic complexes investigated were stable and no photo-degradation was observed. To prove that the resulting ultra fast fluorescence is not a solvent artifact, measurements of acetone were carried out.

6.4 Results

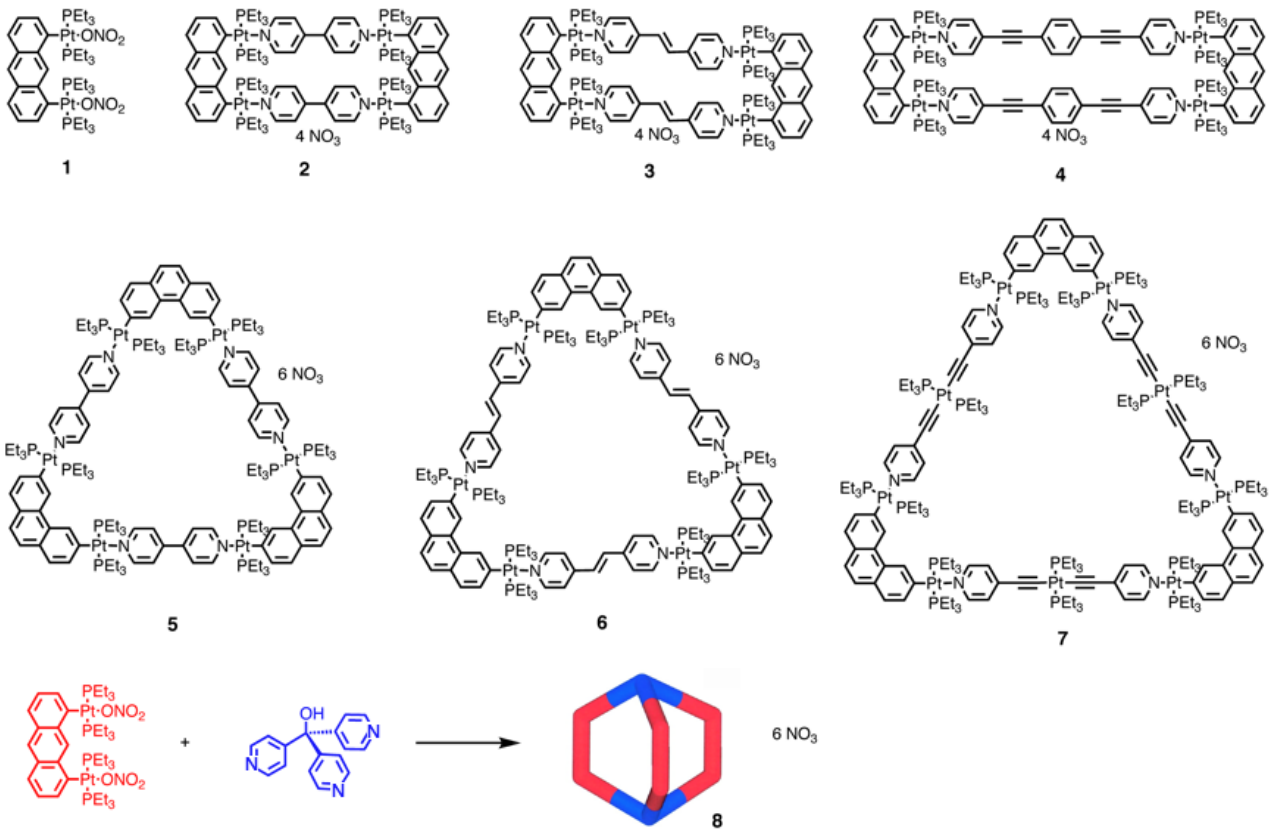

Figure 6.1 Molecular structures of the investigated organometallic monomer "clip" (**1**), metallacycles (**2-7**) and metallocage (**8**).

Figure 6.2 shows the optical absorption data for organometallic compounds **1-4**. All the absorption spectra of these compounds show a vibronic progression that starts at 360 nm with the highest peak in the progression at 389 nm. Indeed, there is a strong similarity in absorption spectra of the first four (**1-4**) organometallic systems. The results suggest that the absorption consists of mainly π-π^* transitions of anthracene whose conjugation might be extended into the Pt-complex. The fact that there is only a small shift in the absorption spectra as the interior conjugation is increased suggests that the main transition is localized on the anthracene-Pt-complex portion of the molecule. As the interior conjugation is increased from compounds **1** to **3** the tail end of the absorbance

spectrum increases. Upon further conjugation (**4**), the tail end of the absorbance spectrum is the same as that of compound (**3**). An increase in the tail end of the absorption, which spans into the visible region until 550 nm, suggests the presence of intramolecular charge transfer effects or a metal-ligand charge transfer transition. It is possible to have the intramolecular charge transfer transitions from the anthracene-Pt complex to various acceptors in the rectangles 4,4'-Bipyridine (**2**), *trans*-1,2-bis(4-pyridyl)ethylene (**3**) and, 4-bis(4'-pyridylethynyl)benzene (**4**). Also shown in Figure 2 are the absorption spectra for the triangular organometallic complexes **5-7**. The presence of the strong vibronic procession that was found in the rectangles is absent for the metallacyclic triangles. This is primarily due to the weaker vibronic progression found in the phenanthrene complex, which is the main chromophore in the triangular organometallic supramolecules.[35] Instead, a long gradual transition is found with a maximum near 345 nm. Triangle **5** has two small noticeable absorption bands at 345nm and 362nm. Triangle **6** has a slightly red-shifted absorption spectrum with a noticeable shoulder at approximately 344nm. Triangle **7** has a broad peak at approximately 343nm and a possible absorption band at 356nm. The absorption in the visible region for these compounds, however, is mainly dominated by the charge transfer transitions arising out of metal-ligand or intramolecular charge transfer in these supramolecular metallacycles. Contrary to that of the supramolecular rectangles, the triangular systems show that the tail end of the absorption spectra amplitude decreases with increasing conjugation. It should be noted that in both series of supramolecular metallacycles, rectangular and triangular, there is very strong absorption deep in the UV. However, our time resolved and nonlinear experiments are more concerned with the metal-ligand interactions found in the

visible portion of the spectrum. Supramolecular metallacage **8** (Figure 6.2) was also studied. The vibronic progression observed in the rectangular series of supramolecules returns with a maximum near that which was found for anthracene-Pt(II) **1**. This observation is similar to previous studies of annulene systems and silsesquioxane.[30] In these systems, the principle $\pi \rightarrow \pi^*$ transition changed dramatically once the triangle or square was closed. The strongly coupled peaks observed in the absorption changed once the macrocycle was broken. It may be that in the present system, the Pt-ligand transfer is so dominant that intramolecular couplings are not strongly affected. In order to probe this process further we carried out time resolved and nonlinear optical experiments.

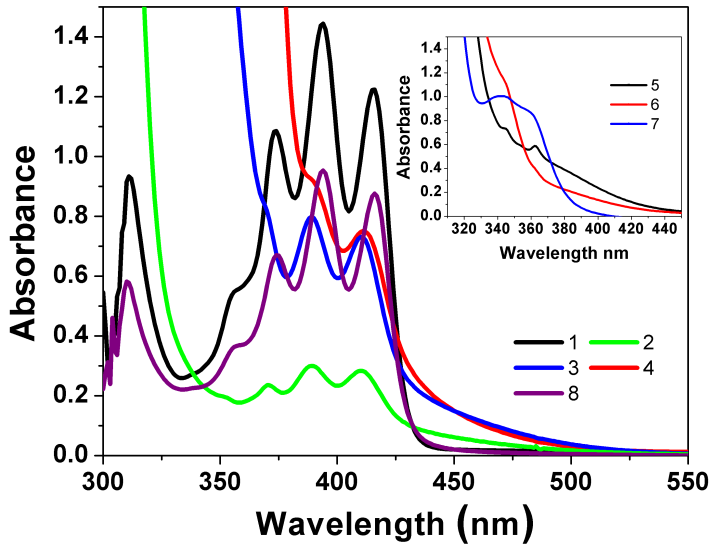

Figure 6.2 Steady state absorbance spectra of compounds **1-4,** and **8**. The insert shows the absorption spectra of compounds **5-7**.

Shown in Figure 6.3 are the optical emission data obtained for compounds **1-4**. For acceptor **1**, after excitation at 356 nm the emission has a strong peak at 472 nm, a smaller peak at 432 nm and a shoulder around 478 nm. For **2**, at 400 nm the emission maximum is shown to be much smaller than the larger peak at 475 nm. Rectangle **3** gives

an emission spectrum peak at 435 nm and a larger peak at 466 nm. On the other hand, **4** has emission spectrum with two equivalent peaks at 458 nm and 485 nm. There is a strong similarity among organometallic systems **1-4**; all emission spectra have a maximum peak at approximately 470 nm. It is clear that by looking at the steady-state emission alone the anthracene-Pt complex appears to be the prevailing emitter. Also shown in Figure 6.3 are the emission spectra for the triangular organometallic complexes (**5-7**) as well as that of the metallacage (**8**). It is clear that increased interior conjugation results in an increasingly strong emission band at approximately 375nm. The results of the emission spectra of triangles show that the emission in smaller triangles (**5-6)** is dominated by the intramolecular charge transfer while that of the largest triangle (**7)** has a measureable contribution from the phenanthrene, which has an emission maximum around 370 nm.

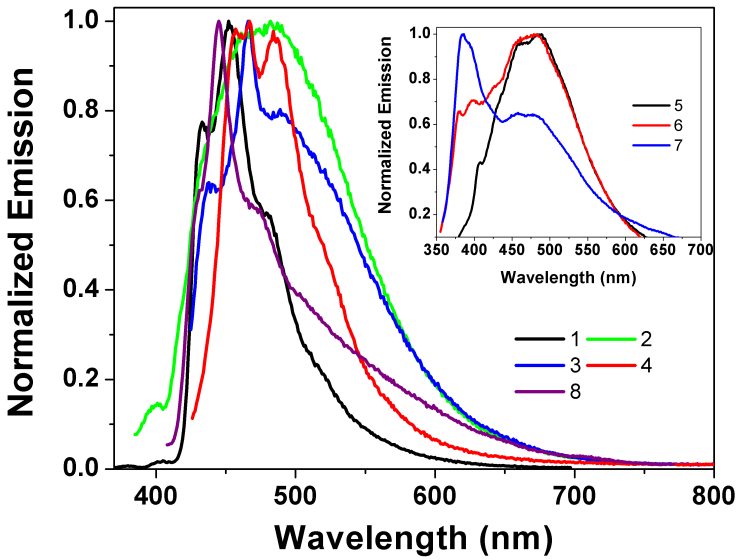

Figure 6.3 Normalized steady state emission spectra profile for compounds **1-4** and **8**. The insert shows the emission spectra of **5-7**.

In general, the steady-state absorption and emission results suggest that the optical excitations consist not only of individual chromophore p-p* transitions in the metallacycle but also of intramolecular or metal-ligand charge transfer transitions. Time-resolved and nonlinear optical property measurements were performed to give a better picture of the transitions and dynamics these systems.

Table 6.1 Steady state absorbance peaks and emission peaks for all compounds.

material	l_{abs}^{max} (nm)	l_{em}^{max} (nm)
1	394	472
2	389	475
3	389	466
4	412	458, 485
5	~400	485
6	~400	474
7	343	382
8	394	446

As stated in the introduction there has been great interest in the use of conjugated organometallic materials as optical limiters and in other nonlinear optical applications. Hence, we are interested in the femtosecond two-photon absorption response in the 700-900nm spectral region. It was found that the length of conjugation in the ligands can have a strong effect on this process. Here, two photon fluorescence measurements were carried out to estimate the nonlinear cross-sections in the Pt-containing organometallic structures.

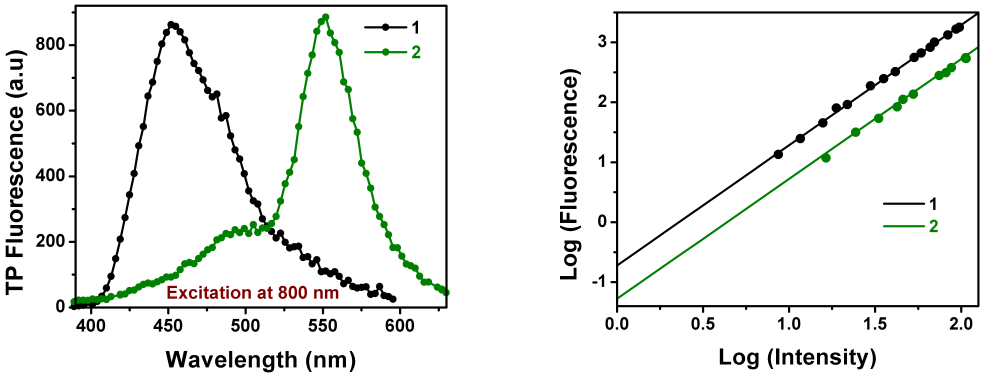

Figure 6.4 Left: The two-photon measurement intensity dependence. Right: The two-photon fluorescence spectrum.

The two-photon fluorescence dependence was carried out using femtosecond (fs) pulses. Figure 4 shows the two-photon fluorescence dependence for compounds **1** and **2**. The appropriate intensity dependence was found for these and other investigated metallacycle systems and a slope of 2, suggesting a two-photon process was observed. With fs pulses one is able to detect and measure the two-photon emission spectra of these and related systems (see figure 6.4). For these macrocycles the spectrum extends over a relatively broad range. These photonic properties could indeed be useful for applications in sensors and optical limiting devices. While the amount of two-photon fluorescence was large, due to the relatively small quantum yield (~10^{-4}) for linear fluorescence in the sample, the calculated two photon cross-section was small (~10 GM). These results suggest that the time-scale of the two-photon measurement may be very fast and the contribution from the triplet state could be small. Previous results with other linear platinum-containing systems showed an increase in the cross-section with increasing delocalization over the ligands.[31] Here, it appears that the two-photon excitation may be localized on each ligand and the main contribution comes from a metal-to-ligand

excitation. This conclusion, however, cannot be concluded from steady-state and two-photon measurements alone.

Time-resolved measurements of the excited state and relaxed states are necessary to more accurately probe the dominate structural/electronic factors in these systems. In the case of relaxed states, fluorescence upconversion experiments were used to probe fluorescence lifetimes over a wide degree of time scales for the purpose of detecting long-range interactions. Here, we are interested in the variation of the fluorescence lifetimes as a function of the chain linkage in the metal centered metallacycles as well as variations due to changes in geometry. Shown in Figure 5 is a representative fluorescence upconversion decay curve for the bis-Pt(II) anthracene **1** at 480 nm. The fluorescence decay profile is best fit by a single exponential given as: $f(x) = Ae^{(-t/\tau)}$. The lifetime for this particular system excited at 400 nm is 8.9 ± 0.2 ps, which can be ascribed to either the intramolecular charge transfer rate or the intersystem crossing to triplet state. This lifetime differs from what has been observed in linear organometallic systems, which in the past have shown fluorescence decay times of 70 ± 40 fs.[31] This discrepancy is due not only to the nonlinear geometry, but also to the metal interaction with the anthracene molecule. The lifetime is shorter than the typical fluorescence lifetime of anthracene (3.9 ns to 6.2 ns).[32] This suggests that the excitation is delocalized up to the metal atom where a fast ISC process dominates its excited state deactivation.

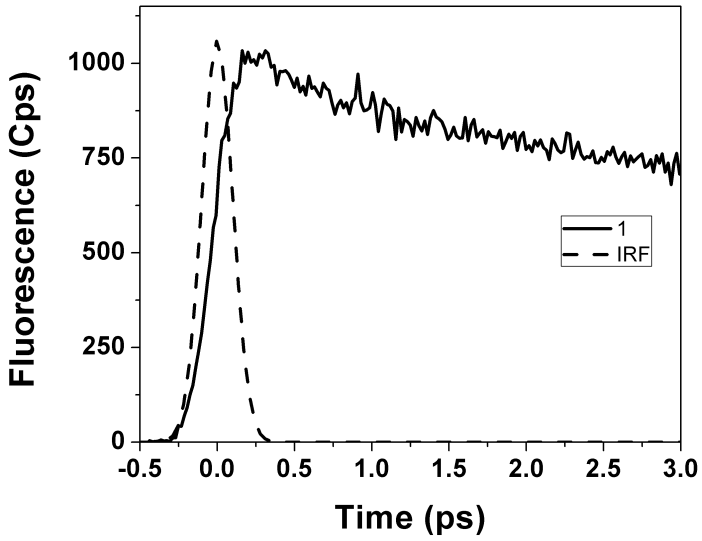

Figure 6.5 Time-resolved fluorescence upconversion of **1** at 480 nm with an excitation at 400 nm. Instrument response function is also shown.

Figure 6.6 shows the time-resolved fluorescence decay at 480 nm for metallacyclic structures **1-4** after excitation at 400 nm. The insert of Figure 6.6 gives the time-resolved fluorescence decay for samples **5-7**. The fluorescence decay of **1** is long lived with respect to the remaining organometallic complexes discussed in this article. The fluorescence decay of complexes **2-4** are extremely fast and therefore close to the instrument response function with a pulse width of 110 fs. The average lifetimes of **2** and **3** at 480nm were found (after deconvolution) to be 110 ± 50 fs and 140 ± 60 fs, respectively. The average lifetime of **4** was found to be 160 ± 60 fs also indicating the presence of a long-lived second component. The fluoresce decay of the triangular samples **5-7** showed similar dynamics with increasing size. Triangle **5** has a lifetime of 130 ± 50 fs, while **6** has a lifetime of 110 ± 40 fs. The fluorescence decay of **7** varried from those of **5** and **6**, having a decay fit with a bi-exponential with a large 190 ± 60 fs component and a small remaining component with a lifetime of 2.4 ± 0.1 ps.

Upconversion fluorescence decay lifetimes are listed in table 6.2.

Table 6.2 The average lifetimes of all upconversion fluorescence sample decays monitored at 480nm.

Material	Average Lifetime
1	8.9 ± 0.2 ps
2	110 ± 50 fs
3	140 ± 60 fs
4	160 ± 60 fs
5	130 ± 50 fs
6	110 ± 40 fs
7	190 ± 60 fs
	2.4 ± 0.1 ps

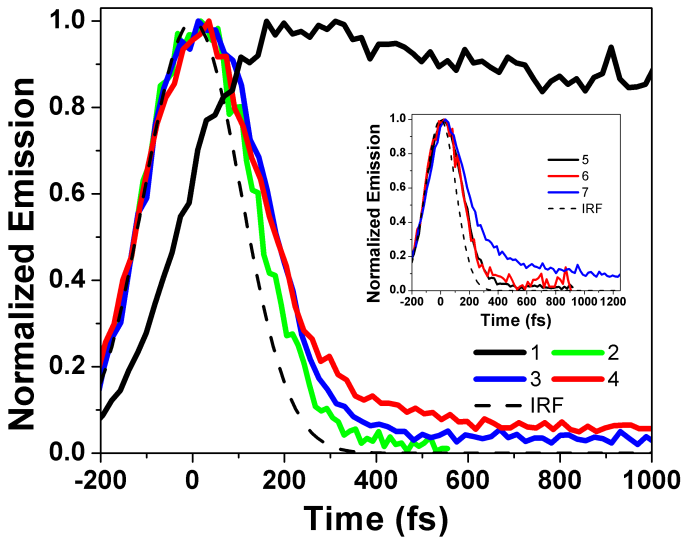

Figure 6.6 Time-resolved fluorescence decay of compounds **1-4** excited at 400 nm. **1** is in black, **2** is in red, **3** is in green, **4** is in blue, and the instrument response function is in the black dashed line. The insert shows the fluorescence decay of compounds **5-7**.

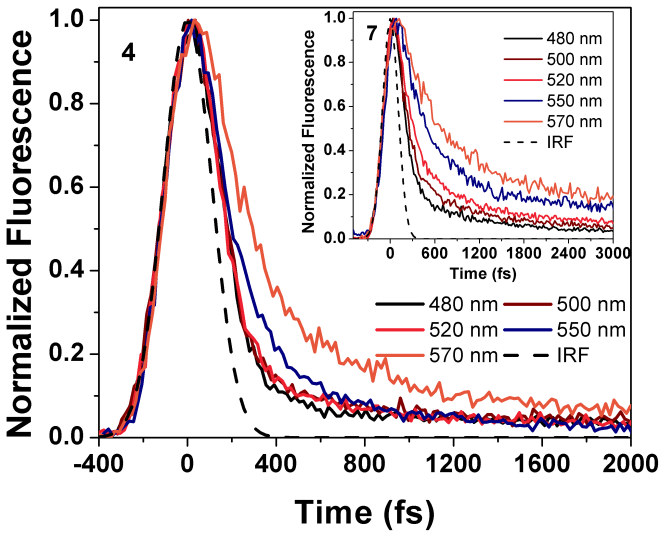

Figure 6.7 Time-resolved fluorescence decay for compound **4** at different wavelengths. Insert: Time-resolved fluorescence decay for triangle **7**.

Upconversion fluorescence decay has also been studied at emission wavelengths of 450 nm, 500 nm, 520 nm, 550 nm and 570 nm resulting in variations in the kinetic time constants. Metallacycles **4** and **7** are representative of the upconversion fluorescence decay lifetimes' emission wavelength dependence and are presented in Figure 6.7 (with sample **7** in the insert). The remaining supramolecular rectangular and triangular fluorescence plots are shown in the supporting information. Femtosecond fluorescence relaxation processes at different emission wavelengths have been investigated previously. For example, in our previous studies we have shown that the fluorescence dynamics of dendrimers at different emission wavelengths can be very important.[33] In this study the bi-exponential lifetime dependence on emission wavelength was in accordance with the formation of two fluorescence states. Such processes are also associated with the formation of aggregates such as excimers or exciplexes. In the discussion of this wavelength dependence on the fluorescence lifetime, an intermediate

trap state best explains the process. Justification for this conclusion comes from the short formation lifetime as compared to the relaxation rates. In the metallacycles studied, it was found that with increasing emission wavelength there was an increase in the average fluorescence lifetime. The lifetimes are described by a bi-exponential decay, with one lifetime being between 100-500 fs and the other lifetime being between 1-6 ps. What is not observed, however, is the long rise time feature found in the dendrimer systems referenced above. This suggests that while there is a strong justification for increased charge-transfer behavior in these systems there may not be a localized intermediate trap state.

The fluorescence upconversion investigations give information about excited state lifetimes as well as the energy migration throughout each system. This can be accomplished through fluorescence anisotropy measurements. The depolarization of the fluorescence as a function of time can be evaluated with very good time resolution by time-resolved fluorescence upconversion. Previous investigations with femtosecond anisotropy measurements have shown the importance of intramolecular interactions to the enhancement of transition moments and nonlinear optical effects.[31] The differences in energy migration and reorientational dynamics in particular systems may point to specific structure-function relationships critical to the design of superior materials. Shown in Figure 8 is a representative fluorescence anisotropy decay result for compounds **1** and **7** out to 3 ps. The noise experienced is due to the weaker signal at long times with the fast anisotropy dynamics essentially completed by this time. The measured initial anisotropy for the case of **1** was near 0.28. Over the 8 ps timescale there was little to no detectable decay of the anisotropy. The remaining rectangular samples had slightly higher

anisotropy values with compound **2** having 0.36, **3** having 0.33 and **4** having 0.3. The triangular metallacycles had anisotropies of 0.37 for **5**, 0.37 for **6** and 0.35 for **7**.

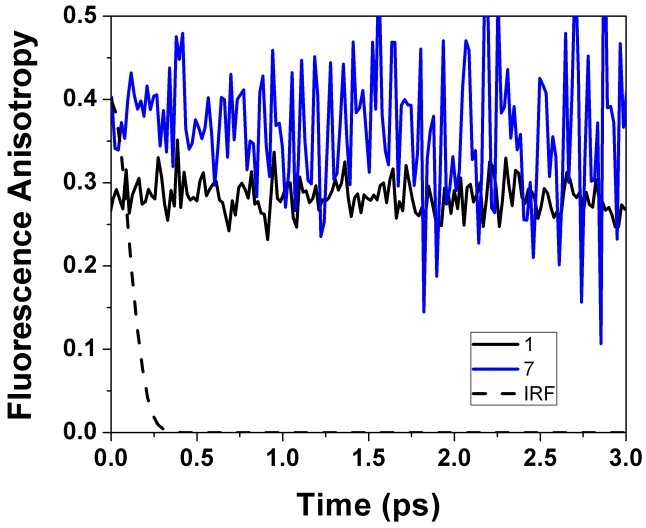

Figure 6.8 Fluorescence anisotropy of **1** and **7** with instrument response function.

For the case of a simple transition moment oscillator system, the initial anisotropy value should be 0.4. The high initial anisotropy (slightly less than 0.4) for all the rectangular and triangular metallocycles confirms that the emission is coming from localized transition dipoles and the emission is not delocalized. The localized excitations are in accordance with the observed intramolecular charge transfer processes in the investigated organometallic systems. The coupling between nearby energy levels accessible to the transition may also give rise to the lower initial anisotropy value. Typically the anisotropy decays from 0.4 to 0. In our systems, there is no discernable anisotropy decay, suggesting that the angle between the emitting and absorbing transition dipoles remains unchanged during intersystem crossing, which is suggestively fast. In our previous measurements we have observed similar effects in square like symmetric

chromophores, cyclic geometry systems, dendrimer systems and linear systems.[16,31,33] These results suggest that the electronic excitation may be localized on one of the chromophores and that the complex excited-state dynamics is entirely directed by intra-chromophore processes.

While time-resolved fluorescence upconversion provides important details about relaxed states in the supramolecular rectangular and triangular systems, ultra-fast transient absorption experiments give important details about the excited state dynamics and amplitudes critical to triplet and singlet lifetimes as well as extent of charge transfer character. Measurements of the excited state lifetimes have been carried out with these systems to probe the changes in charge transfer character with different sized linkers.

Figure 6.9 shows the transient absorption spectrum of compounds **1-4**. Figure 6.10A shows the spectrum of **1**, in which a decay of the excited state absorption (ESA) at a wavelength of 620 nm concomitant growth of ESA at 490 nm is observed. ESA at 490 nm can be ascribed to the triplet-triplet state absorption of anthracene. The lifetime of the ESA is ~20 ps and corresponds with the growth of ESA with a time constant of 22 ± 1.0 ps for the 490nm kinetics. The kinetic analysis of the absorption at 620nm showed a lifetime of 17.1 ± 0.44 ps. The isosbestic point at approximately 545nm is typical of conversion between the triplet and relaxed triplet state. The spectrum of compound **2** (Figure 6.9) shows the decay of the ESA with a maximum around 650 nm from 100 fs to 1 ps, which arises from an intramolecular charge transfer from anthracene to bipyridyl. The fast component observed in the fluorescence matches with the intramolecular electron transfer rate. However, the broad ESA (Figure 6.9.2) decayed very quickly to give rise to absorption around 480 nm, reminiscent of triplet-triplet ESA of the

anthracene-Pt complex. The results show that there is an ultrafast forward electron transfer followed by recombination with time scales of 6.05 ± 0.09 ps for **2**.

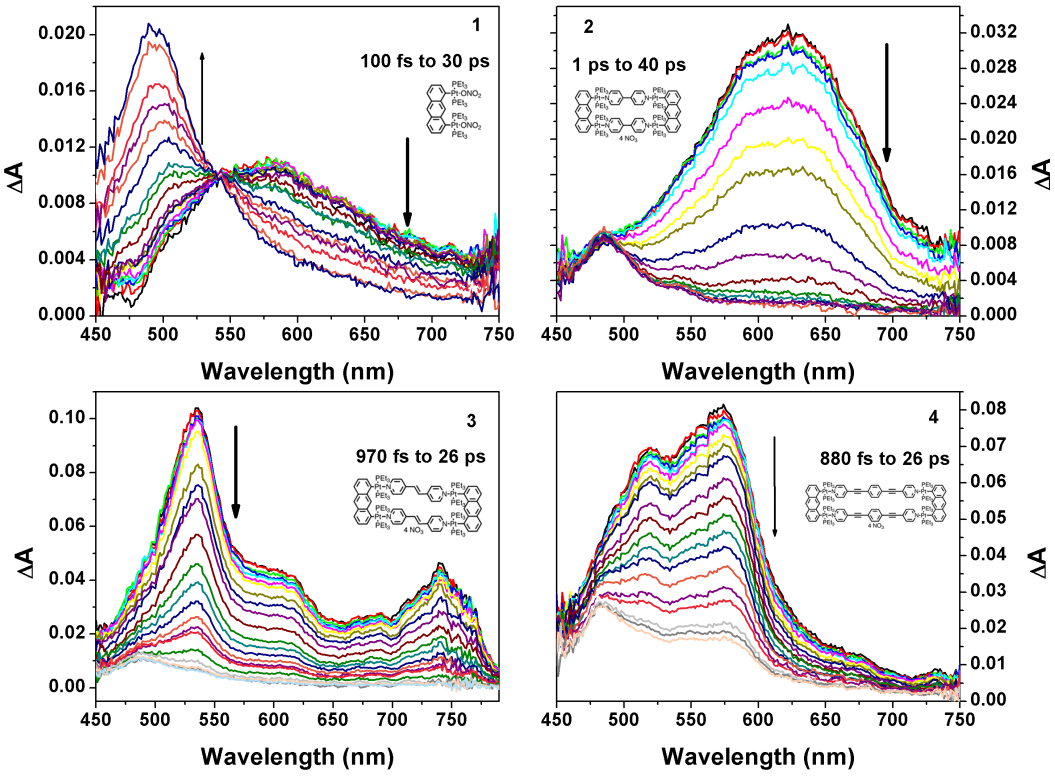

Figure 6.9 Transient absorption spectrum of compounds **1-4** in acetone at various time delays. Top Left: spectra of **1** after excitation at 390 nm 100 fs to 30 ps. Top Right: spectra of **2** after excitation at 390 nm1 ps to 40 ps. Bottom Left: spectra of **3** after excitation at 390 nm 30 ps to 750 ps. Bottom Right: spectra of **4** after excitation at 390 nm 880 fs to 26 ps.

The results indicate that the recombination is producing the triplet state exciton, which is long lived though not as efficient as the anthracene-Pt complex. Interestingly, a completely different transient spectrum is obtained for compounds **3-4**. The ultrafast growth of the intramolecular charge transfer and consequent recombination gives rise to a

triplet state due to the anthracene-pt complex is observed for sample **3**. This is evident from the entirely different transient absorption spectrum for **3**, as it has different transient radical species with the anion located on the bipyridyl stilbene that has a typical ESA spectrum.

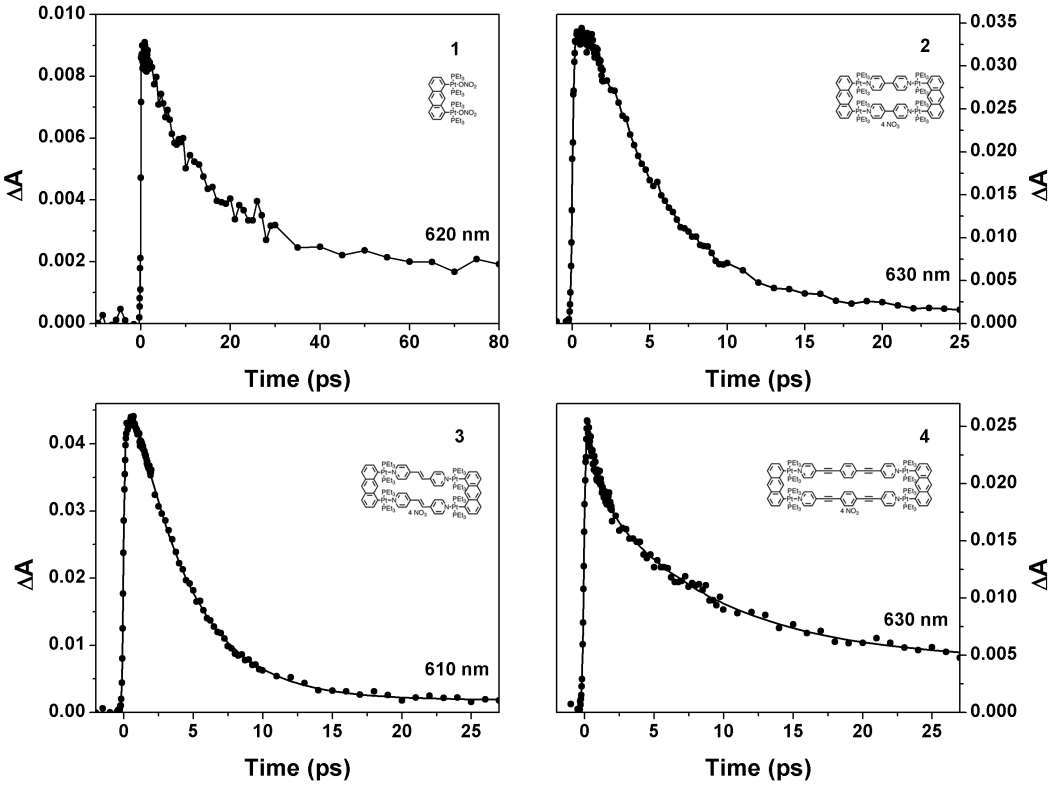

Figure 6.10 Kinetic decays for the transient absorption spectrum of compounds **1-4** in acetone at various time delays. Top Left: kinetics of **1** after excitation at 390 nm. Top Right: kinetics of **2** after excitation at 390nm. Bottom Left: kinetics of **3** after excitation at 390 nm. Bottom Right: kinetics of **4** after excitation at 390 nm.

The transient absorption growth and decay are also observed for organometallic rectangle **4**, with different transient spectra arising out of the ICT from anthracene-Pt complex to the anion radical present in the metallacycle **4**. The lifetimes of the charge

separation and recombination are obtained from the global fit analysis of the kinetic decay trace (Figure 6.10). Also, the kinetic decay traces at two different wavelengths, representing the ESA of the ICT state and the triplet-triplet absorption are seen in Figure 10. The decay lifetime was 22.0 ± 1.0 ps for compound **1**. The substantial difference between bis-Pt(II) anthracenyl acceptor **1** and rectangular supramolecules **2-4** suggests stronger intramolecular interactions leading to different charge transfer character and lifetimes. Table 6.3 outlines the various transient absorption kinetics and the charge separation and recombination lifetimes.

Table 6.3 Transient absorption average lifetimes for samples **1-4**.

Transient Absorption Kinetics		
Material	Wavelength (nm)	Time (ps)
1	620	17.1 ± 0.44
2	630	6.05 ± 0.09
3	610	4.49 ± 0.07
4	630	6.47 ± 0.24

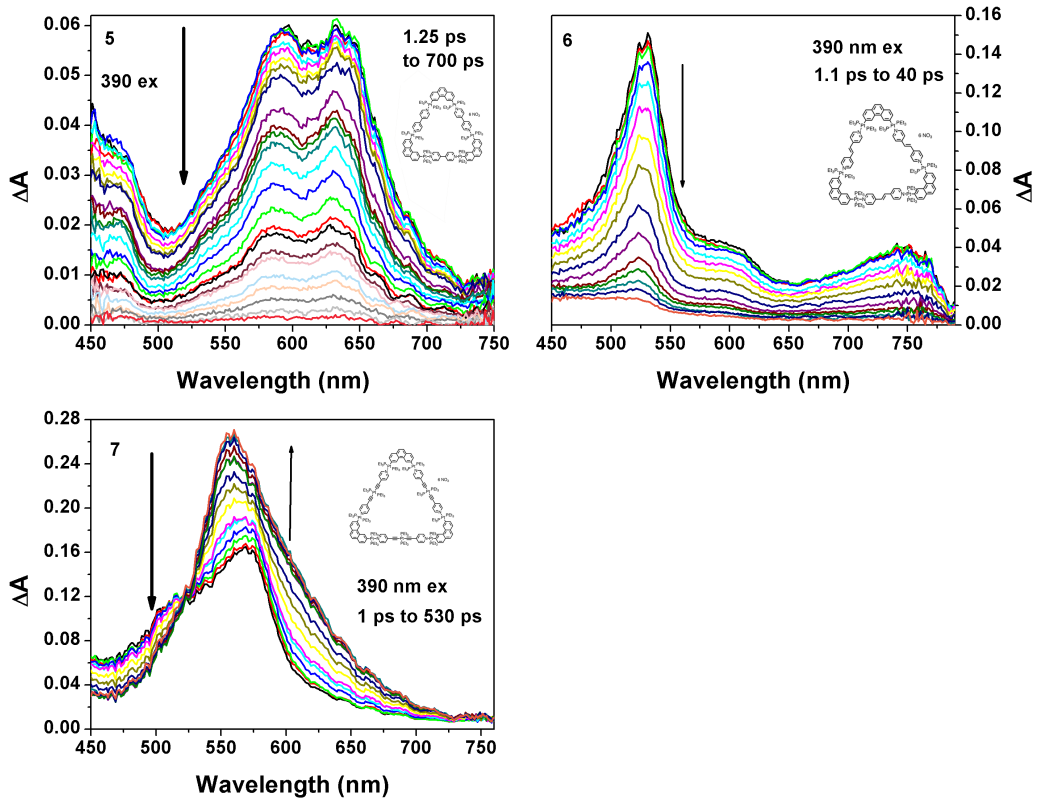

Figure 6.11 Transient absorption spectra of triangles **5-7** in acetone at various time delays. Top Left: spectra of **5** after excitation at 390 nm 1.25 ps to 700 ps. Top Right: spectra of **6** after excitation at 390 nm 1.1 ps to 40 ps. Bottom Left: spectra of **7** after excitation at 390 nm 1 ps to 530 ps.

Figure 6.11 shows the transient absorption spectrum of triangular metallacycles **5-7**. For **5**, it can be observed that there is a growth of the excited state absorption with a maximum near 600 nm and a growth at 450 nm. At 490 nm, the kinetic decay for compound **5** is described by a bi-exponential decay with lifetimes of 5.7 ± 0.4 fs and 114.8 ± 8.9 fs. At 640 nm, the kinetic decay gives the bi-exponential decay lifetimes of 10.5 ± 0.7 fs and 150 ± 5.4 fs. The extremely fast lifetime decay for compound **5** is drastically different from that of the other systems studied. This suggests extremely fast ICT. Compound **6** displays a similar transient absorption profile with a maximum near

525 nm. At 525 nm a single exponential lifetime decay of 8.1 ± 0.2 ps is observed, while at 565 nm an exponential lifetime decay of 6.7 ± 0.2 ps is found. These two lifetimes are evident of triplet state relaxation. Interestingly a completely different transient spectrum is obtained for metallacycle **7**. A maximum excited state absorption was found at 555 nm with an isosbestic point at 525 nm. Again, the isosbestic point suggests conversion between the triplet and relaxed triplet state. The lifetimes of the charge separation and recombination for the triangular supramolecules are obtained from the global fit analysis of the kinetic decay trace (Figure 6.12). The kinetic decay traces at two different wavelengths representing the ESA of ICT state and the triplet-triplet absorption are seen in Figure 6.12. The average exponential lifetime of **7** is 21.5 ± 0.7 ps at 460nm. As observed for compounds **2-4**, the substantial difference for triangle **7** from the other supramolecular triangles may be attributed to stronger intramolecular interactions leading to different charge transfer characters and lifetimes. Table 6.4 gives their transient absorption kinetic lifetimes.

Table 6.4 Transient absorption average lifetimes for samples **5-7**.

Transient Absorption Kinetics		
Material	Wavelength (nm)	Time (ps)
5	640	0.184 ± 0.006
6	525	8.1 ± 0.2
7	460	21.9 ± 0.9

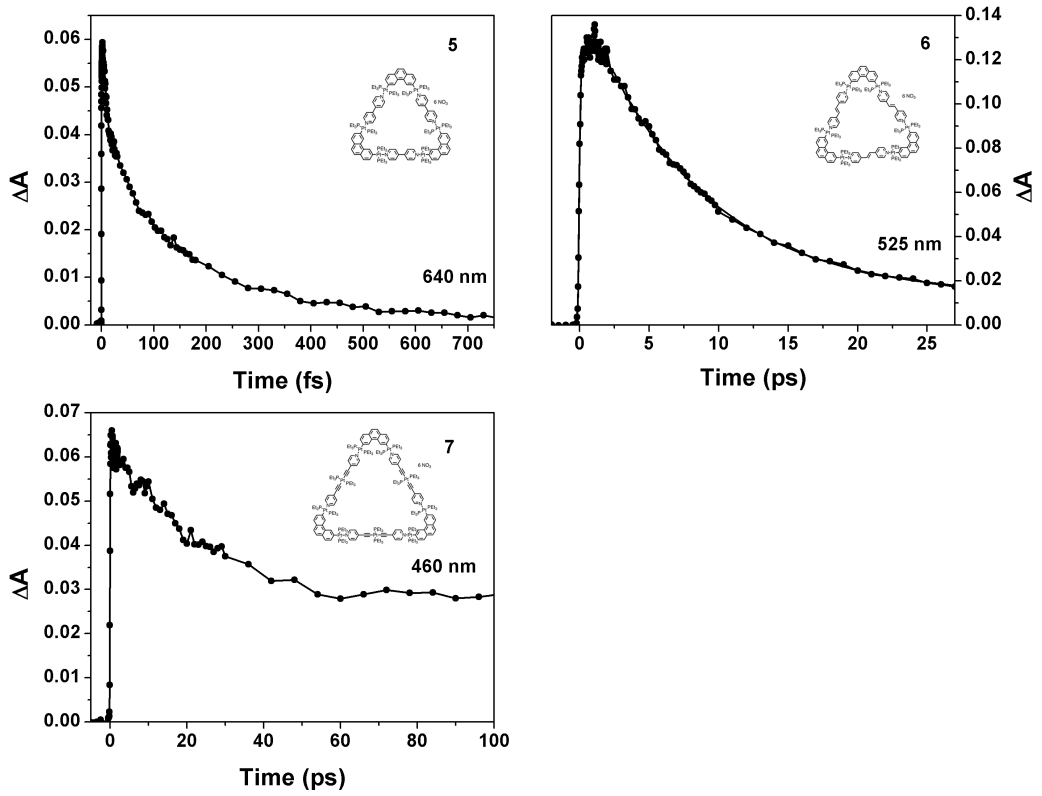

Figure 6.12 Transient absorption kinetics for supramolecular triangles **5-7**.

A three dimensional metallacage (**8**) was studied to investigate the role that dimensionality plays in charge transfer dynamics. Toward this aim, steady state measurements, fluorescent upconversion and transient absorption measurements were carried out. Figure 6.13 displays the upconversion lifetimes, transient absorption, transient kinetics and anisotropy measurements of metallacage (**8**). Compound **8** displays similar absorbance spectra to that of compound **1** with a high peak at 446 nm and a vibronic progression of 423 nm, 472 nm, and 500 nm as the main chromophore is similar to that of compound **1**. The shoulder at 423 nm is similar to that of the lower peak for compound **1**, while the shoulder at 472 nm of the metallacage lines up with the highest

peak of **1**. The metallacage emission spectrum differs from compound **1** in that it has a much stronger tail into the red. This again accounts for the larger cage structure of compound **8**, which contains three bis-Pt(II) anthracenyl moieties (**1**). The fluorescence upconversion decay lifetimes are described by a bi-exponential decay for 450 nm, 480 nm, and 500 nm, and 520 nm. With increasing emission wavelength, increasing fluorescence lifetimes are found for both the short and long decay processes, indicating the presence of intramolecular charge transfer interactions. At 480 nm a short lifetime of 420 fs and a long lifetime of 2.4 ps were observed. At 520 nm, a short lifetime of 760 fs and a long lifetime of 4.3 ps were found.

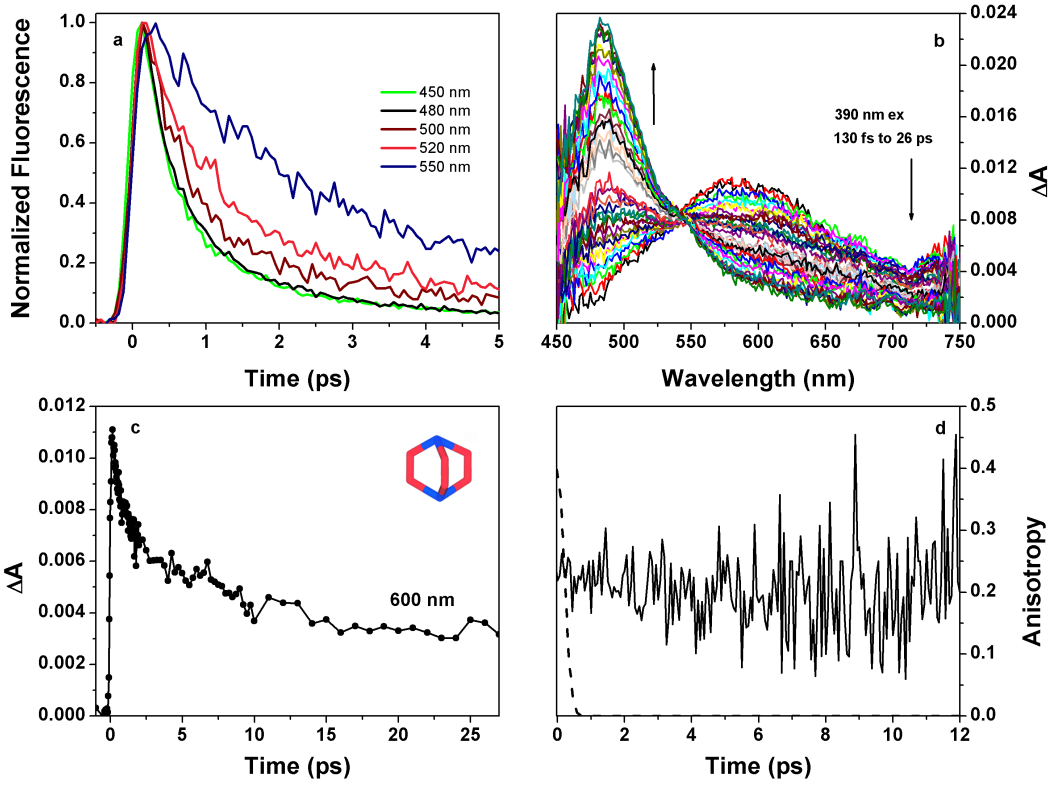

Figure 6.13 Metallacage (a) Fluorescence upconversion lifetimes (b) Transient absorption spectrum (c) Transient absorption kinetics (d) Anisotropy.

Transient absorption experiments were carried out giving a maximum excited state absorption at approximately 482 nm with an inflection point at 542 nm and two smaller absorption peaks at 590nm and 745nm. The lifetimes of the charge separation and recombination for the metallacage were described by a bi-exponential decay with a lifetime of 1.1 ps and 32.2 ps at 600 nm. In general while the cage compound shows a higher degree of complexity in structure, the dynamics appeared to be very similar to what was found with the metallacycles investigated.

6.5 Discussion

The goal of this investigation was to probe the differences in charge transfer character, triplet state relaxation, excited fluorescence dynamics and potential nonlinear optical and electronic applications. The observed results suggest that these metallacycles vary in their triplet state relaxation when the square like geometry is changed to the triangular system. The kinetic schemes for excitations in similar organometallic complexes have been illustrated in previous reports.[31] For informative reasons a variation of this diagram is reproduced in Figure 6.14. As seen in the diagram, a chromophore is excited from the ground state S_0 to the S_1 state. ISC allows for the S_1 state to transition to the T_1 state, which then decays to the ground state. Femtosecond fluorescence upconversion is used to determine the extent of ISC and singlet decay while transient absorption is determines the TTA and ESA. In our previous study regarding the platinum acetylene complexes, ISC time increased with ligand length.[31] It is understood that the increased π^* character as well as the decreased heavy atom effect were the factors for the increased ISC lifetime. In the current study, increasing ligand length was accomplished by substitution of the different ligands 4,4'-Bipyridine (**2,5**), *trans*-1,2-bis(4-

pyridyl)ethylene (**3,6**) and 1,4-bis(4'-pyridylethynyl)benzene (**4**) and *trans*-[bis(4-pyridylethynyl)bis(triethylphosphine)]platinum(II) (**7**). The compound with the longest fluorescence lifetime was the bis-Pt(II) anrthracenyl acceptor (**1**). Upon conjugation, the ISC time dramatically decreased. The dramatic decrease in ISC lifetime (in the 100fs range) typically suggests very strong spin-orbit coupling due to the presence of the Pt metal. Since this was not the case for compound **1**, it is believed that conjugation was the determining factor for the ultrafast fluorescence (ISC) results. However, as shown earlier, the charge transfer contribution to the observed dynamics depends on the nature of the bridging ligand and its energetics rather than the conjugation length. For the rectangular organometallic structures, further conjugation showed evidence of slightly increasing ISC times although all lifetimes were within the experimental error. For the triangular organometallic compounds, organometallic triangle **6** displayed a slightly decreased lifetime with respect to triangle **5**, although again this was also within the error. Interestingly, compound **7** showed a dramatic increase in the lifetime from that of **5** and **6**. This result is unexpected given that the ligand contains more platinum atoms, which should result in a shorter ISC lifetime. A possible reason for this can be because of the presence of weaker charge transfer interactions, which increases the fluorescence lifetime. It can be observed from the absorption measurements that the charge transfer absorption for **7** is significantly lower than **5** and **6**. A comparison of the rectangular and triangular organometallic structures shows considerable similarities. Both systems have ultrafast ISC, an increase in ISC with increasing conjugation, and emission wavelength dependence. However, the large ISC lifetime variation between compounds **4** and **7** was

not expected. This can possibly be attributed to the anthacene moiety as well as to different ligands.

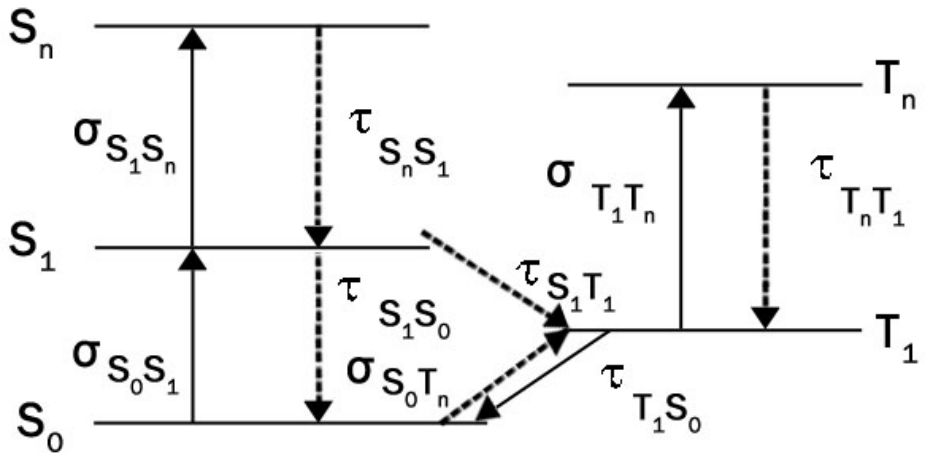

Figure 6.14 Kinetic scheme for the organometallic complexes.

Metal-to-ligand charge transfer processes with varying degrees of conjugation in the ligands has been investigated in the past. For example, Ren, et.al investigated such charge transfer processes in oligoynes.[34] It was found that for the case of linear absorption, the low energy metal-to-ligand charge transfer band has a significant shift to lower energy as the ligand-conjugation is increased. It was also found that as the π character is increased in the ligand the charge transfer character also changed for the complex, which follows from basic electron transfer molecular processes. The drastic difference in lifetimes for the triangular organometallic cages **5-7** gives evidence for the charge transfer character dependence on increased conjugation. Such variations in lifetimes with similar steady state absorption profiles demonstrates that the steady state profiles alone are not capable of describing the complexities of the charge transfer within organometallic systems.

6.6 Conclusions

Using femtosecond upconversion and transient absorption, we have measured and characterized the ultra-fast excited state relaxation dynamics of platinum containing organometallic metallacycles. Typically a bi-exponential decay was capable of describing the two fluorescence species. We found intramolecular charge transfer processes giving rise to charge-separated species followed by charge recombination to give rise to the triplet exciton. One species is the decay of immediate ESA ascribed to singlet state. The other observed species is a long lived excited state, which is ascribed to triplet-triplet absorption of anthracene and phenanthrene. It was determined that the presence of platinum influences the spin-orbit coupling and increases the rate of ISC while decreasing the lifetime of the singlet state. The rectangular structures show similar transient lifetimes within the series studied. However, the triangular systems showed a strong and definite effect on the ligand conjugation. A consistent increase in the lifetime was observed as the conjugation of the ligand unit next to the metal center was increased. The triangular unit, for this reason, is a great candidate for nonlinear optical and optical limiting effects.

References:

[1] (a) Patil, A. O.; Heeger, J.; Wudl, F. *Chem. Rev.* **1988**, *88*, 183. *(b) Tour, J. M. Acc. Chem. Res.,* **2000**, *33*, 791. (c) *Zang, L.; Che, Y.; Moore, J. S. Acc. Chem. Res.*, **2008**, *41*, 1596. (d) *Bredas, J. L.; Norton, J. E.; Cornil, J.; Coropceanu, V. Acc. Chem. Res.*, **2009**, *42*, 1699.

[2] Kohler, A.; Wilson, J. S. *Org. Elect.* **2003,** *4*, 179.

[3] Rogers, J. E.; Hall, B. C.; Hufnagle, D. C.; Slagle, J. E.; Ault, A. P.; McLean, D. G.; Fleitz, P. A.; Cooper, T. M. *J. Chem. Phys.* **2005,** *122*, 214708.

[4] Cooper, T. M.; Krein, D. M.; Burke, A. R.; McLean, D. G.; Rogers, J. E.; Slagle, J. E.; Fleitz, P. A. *J. Phys. Chem. A.* **2006,** *110*, 4369.

[5] Cooper, T. M.; Krein, D. M.; Burke, A. R.; McLean, D. G.; Rogers, J. E.; Slagle, J. E. *J. Phys. Chem. A.* **2006,** *110*, 13370.

[6] Silverman, E. E.; Cardolaccia, T.; Zhao, X.; Kim, K.-Y.; Haskins-Glusac, K.; Schanze, K. S. *Coord. Chem. Rev.* **2005,** *249*, 1491.

[7] Wong, W.-Y.; Ho, C.-L. *Coord. Chem. Rev.* **2006,** *250*, 2627.

[8] Tessler, N.; Denton, G. J.; Friend, R. H. Nature **1996**, 382, 695.

[9] Rogers, J. E.; Slagle, J. E.; Krein, D. M.; Burke, A. R.; Hall, B. C.; Fratini, A.; McLean, D. G.; Fleitz, P. A.; Cooper, T. M.; Drobizhev, M.; Makarov, N. S.; Rebane, A.; Kim, K.-Y.; Farley, R.; Schanze, K. S. *Inorg. Chem,* **2007,** *46*, 6483.

[10] Slagle, J. E.; Cooper, T. M.; Krein, D. M.; Rogers, J. E.; McLean, D. G.; Urbas, A. M. *Chem. Phys. Lett.* **2007,** 447, 65.

[11] Bhaskar, A.; Guda, R.; Haley, M.; Goodson, T. I. *J. Am. Chem. Soc.* **2006,** *128*, 13972.

[12] Varnavski, O. P.; Ranasinghe, M.; Yan, X.; Bauer, C. A.; Chung, S.-J.; Perry, J. W.; Marder, S. R.; Goodson, T. III. *J. Am. Chem. Soc.* **2006,** *128*, 10988.

[13] Liu, Y.; Jiang, S.; Glusac, K. D.; Powell, D. H.; Anderson, D. F.; Schanze, K. S. *J. Am. Chem. Soc*. **2002**, *124*, 12412.

[14] Vestberg, R.; Westlund, R.; Eriksson, A.; Lopes, C.; Carlsson, M.; Eliasson, B.; Glimsdal, E.; Lindgren, M.; Malmström, E. *Macromolecules*, **2006**, *39*, 2238.

[15] *Guo, F.; Sun, W.; Liu, Y.; Schanze, K.; Inorg. Chem.*, **2005**, *44*, 4055.

[16] Bhaskar, A.; Ramakrishna, G.; Hagedorn, K.; Varnavski, O. P.; Mena-Osteritz, E.; Bäuerle, P.; Goodson, T. III. *J. Phys. Chem. B.* **2007,** *111*, 946.

[17] Goodson, T. III. *Acc. Chem. Res.* **2005,** *38*, 99-107.

[18] Ramakrishna, G.; Bhaskar, A.; Goodson, T. III. *J. Phys. Chem. B* **2006,** *110*, 20872.

[19] Yam, V. W. W. *Acc. Chem Res*. **2002**, *35*, 555.

[20] Ghosh, S.; Mukherjee, P. S.; *Organometallics* **2008**, *27*, 316.

[21] Stang, P. J.; Olenyuk, B. *Acc. Chem. Res.* **1997**, *30*, 502.

[22] Leininger, S.; Olenyuk, B.; Stang, P. J. *Chem. Rev.* **2000**, *100*, 853.

[23] Seidel, S. R.; Stang, P. J. *Acc. Chem. Res.* **2002**, *35*, 972.

[24] Kuehl, C. J.; Huang, S. D.; Stang, P. J. *J. Am. Chem. Soc.* **2001**, *123*, 9634.

[25] Kryschenko, Y. K.; Seidel, S. R.; Arif, A. M.; Stang, P. J. *J. Am. Chem. Soc.* **2003**, *125*, 5193.

[26] Kuehl, C. J.; Kryschenko, Y. K.; Radhakrishnan, U.; Seidel, S. R.; Huang, S. D.; Stang, P. J. *Proc. Natl. Acad. Sci. U.S.A.* **2002**, *99*, 4932.

[27] Ghosh, S.; Chakrabarty, R.; Mukherjee, P. S. *Inorg. Chem.* **2009**, *48*, 549.

[28] Bhaskar, A.; Ramakrishna, G.; Lu, Z.; Twieg, R.; Hales, J. M.; Haga, D. J.; Van Stryland, E.; Goodson, T., III. *J. Am. Chem. Soc.* **2006**, *128*, 11840.

[29] Varnavski, O.; Goodson, T. *Chem. Phys. Lett*. **2000**, *320*, 688.

[30] Sulaiman, S.; Bhaskar, A.; Zhang, J.; Guda, R.; Goodson, T. III; Laine, R. M. *Chem. of Mat.* **2008**, *20*, 5563.

[31] Ramakrishna, G.; Goodson, T. III; Rogers-Haley, J. E.; Cooper, T. M.; McLean, D. M.; Urbas, A. J. *Phys. Chem. C* **2009**, *113*, 1060.

[32] Birks, J.B. *Photophysics of Aromatic Molecules,* Wiley: London, 1970.

[33] Varnavski, O.; Leanov, A.; Liu, L.; Takacs, J.; Goodson, T. III. *Physical Review B.* **2000**, *61*, 12732.

[34] Xu, G. L.; Wang, C. Y.; Ni, Y. H.; Goodson, T. III; Ren, T. *Organometallics*, **2005**, *24*, 3247.

[35] Murov, S. L.; Carmichael, I.; Gordon, L. H. *Handbook of Photochemistry*, Marcel Dekker Inc: New York. 1973.

Chapter 7 Conclusions

7.1 Summary

In this dissertation, we discussed the theory, implementation, and application of pulse shaping to fluorescence microscopy and pump-probe microscopy. In the second chapter, phase shaping was used to compensate for dispersion from microscope optics resulting in compressed pulses at the sample. The resulting high peak intensities were used to drive nonlinear transitions at low average power. Techniques for the selective excitation of two-photon absorbing fluorophores were discussed where a binary genetic algorithm was found to quickly converge to the optimal phase mask for selective excitation.

In the third chapter, one-photon FRET stoichiometry theory was generalized to account for two-photon excitation. A library of computational methods implemented this theory enabling the analysis of large volumes of data in minutes. Two-photon FRET stoichiometry was demonstrated with live COS-7 cells transfected with mAmetrine, tdTomato, and mAmetrine-tdTomato constructs. The resulting images containing 167 cells were analyzed in approximately 10 minutes. The two-photon FRET stoichiometry made the accurate measurement of donor and acceptor in construct as well as the ratio of total acceptor to donor possible. The fast selective excitation switching (~30ms) enabled

by the pulse-shaping approach will allow the application of quantitative multiphoton FRET to dynamic systems.

In the fourth chapter, a pulse shaping based pump-probe microscope was built, where broadband 800nm pulses acted as the pump source and 400nm pulses acted as the probe. The two-color pump-probe design enables characterization of two-photon excited transient states. To measure transient states on the femtosecond time scale an additional pulse shaper was built to compress the SH probe after the microscope objective. Met-hemoglobin solution had both ESA and GSB lifetimes whereas oxy-hemoglobin only had a GSB pathway. The ESA and GSB pathways were used to image red blood cells by selecting the appropriate temporal delay and frequency domain. An additional imaging modality in red blood cells was found at low modulation frequency, possibly due to thermal lensing.

In chapter five, two-photon active fluorescent protein-type chromophores were synthesized with a diverse set of substituent groups. The GFP-type chromophores were found to have modest two-photon cross-sections reaching up to 40 GM at 800 nm for the dimethylamino-substituted system. Time-resolved fluorescence upconversion was used to measure bi-exponential lifetimes on the femtosecond and picosecond time scale. The individual effects of the substitution position of functional groups as well as their relative bulk size were found to play a significant role in the fluorescence decay characteristics. These molecules show promise as biological markers for applications in measuring conformation changes and aggregation of amyloid peptides known to contribute to many neurodegenerative diseases.

In chapter six, ultrafast excited state dynamics of platinum containing organometallic metallacycles were characterized using femtosecond fluorescence upconversion and transient absorption. On average, a bi-exponential decay was capable of describing the two fluorescent species. Intramolecular charge transfer processes gave rise to charge-separated species and recombination resulting in a triplet exciton. One fluorescent decay was associated with the decay of the singlet ESA. The other species is associated with triplet-triplet absorption of anthracene and phenanthrene. The presence of platinum influences spin-orbit coupling and increases the rate of ISC while decreasing the lifetime of the singlet state. While the rectangular structures showed similar transient lifetimes, the triangular systems were highly dependent on ligand conjugation. Increasing ligand conjugation resulted in increasing lifetimes. The triangular unit, for this reason, is a great candidate of nonlinear optical and optical limiting applications.

7.2 Future Direction

When the laser was first developed it was described as a hammer looking for a nail. One of the first intended applications was to break specific bonds in a form of coherent control. Today, lasers play an increasing role in material characterization and synthesis. In this dissertation, ultrafast spectroscopy was used to characterize materials with optical responses on the femtosecond time scale. The combination of these techniques with optical microscopy has enabled the visualization of materials through the unique quantum pathways associated with their components. The integration of multiple nonlinear imaging modalities such as SHG, THG, and TPEF could be integrated into our system offering more modes of contrast. In the far future, extending the frequency range

of table top coherent light sources to encompass not just visible wavelengths, but x-ray, terahertz, infrared and beyond offers new and excited possibilities.

Pulse-shaping-based two-photon FRET stoichiometry was demonstrated in live COS-7 cells *in vitro*. The increased depth penetration using two-photon excitation enables future *in vivo* studies. One exciting application would be using the FRET pair aptamer-thrombin for the *in vivo* analysis of tumor growth, metastasis, and angiogenesis. Applying stoichiometric techniques to such a system would give cancer researchers quantitative metrics for drug cancer interactions. Another exciting route is in extending FRET stoichiometry to more than just one donor and acceptor molecule. Human cells contain thousands of molecules that interact in a highly complex and orchestrated manner. Quantifying the interaction of such complicated dynamics at the millisecond time scale would enable medical personnel to diagnose both the cellular components and mechanisms used by pathogens and diseases in a time frame necessary for possible treatment. Unfortunately, extending FRET stoichiometry to systems with many identifiers, such as N-way FRET, would result in increasingly complex parametric functions. Advances in machine learning and nonlinear algorithms offer routes towards such complicated stoichiometric analysis and are an exciting possibility.

While chemical contrast imaging with pulse-shaping-based pump-probe microscopy has been successfully applied to imaging red blood cells, many other interesting systems could be studied with this technique. Pathogens and diseases such as malaria and sepsis introduce and alter chemical structures in healthy cells. Label free detection using pump-probe microscopy offer opportunities toward *in vivo* identification. Another system of interest is thiophene-fullerene blends (P3HT:PCBM). This polymer

blend material has shown great promise in electro-optic devices. Unfortunately, in the solid state (thin film), molecular aggregation, complex topology, and non-uniform homogeneity drastically influence kinetics. The effect of which is low carrier mobility and short-lived exciton lifetimes resulting in low exciton diffusion lengths, limiting their efficiency and device applicability. Pulse-shaping-based pump-probe microscopy offers routes towards imaging these exciton dynamics on the femtosecond time scale giving insight into structure-function relationships.

In this dissertation, we also discussed the molecular design of materials with specific nonlinear optical responses. GFP-variants were designed to have large two-photon cross-sections for fluorescence imaging. New molecular probes may be designed not just for imaging, but for optogenetics and other optical control techniques for driving specific cellular functions. In the case of optical limiters, where nonlinear optical responses are used as low-pass filters to protect against high power lasers, pulse shaping techniques offer routes to bypass such defenses. The nature of light-matter interactions and the steady increase in technology to control such dynamics leaves countless opportunities for the future.